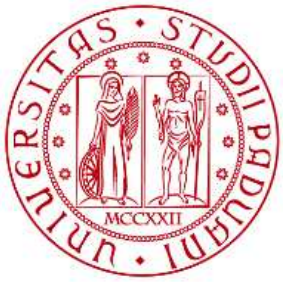

UNIVERSITÀ
DEGLI STUDI
DI PADOVA

DIPARTIMENTO DI INGEGNERIA INDUSTRIALE

CORSO DI LAUREA MAGISTRALE IN INGEGNERIA AEROSPAZIALE

EFFETTO DELL'ALTA TEMPERATURA SULLE PROPRIETÁ DELLO STRATO DI OSSIDO NELLE LEGHE A BASE DI Ni-Cr 625 PRODOTTE PER MANIFATTURA ADDITIVA

EFFECT OF HIGH TEMPERATURE ON OXIDE LAYER PERFORMANCE OF ADDITIVELY MANUFACTURED Ni-Cr-Based Alloys 625

Relatore: **Prof. Manuele Dabalà**

Correlatore: **Arshad Yazdanpanah**

Laureanda: **Lisa Zotta**

ANNO ACCADEMICO 2023-2024

Abstract (EN)

This study investigates nickel-chromium (Ni-Cr) based alloys, which are high-performance materials renowned for their exceptional resistance to both high temperatures and corrosion. These alloys are critical in the aerospace industry, particularly for engine components and exhaust systems. The material under examination was fabricated using Laser Powder Bed Fusion (LPBF), an advanced 3D printing technique that employs a laser to selectively melt and solidify metal powder layers in intricate deposition patterns. Aircraft engines, especially turbines, operate under extreme conditions of high temperatures and humidity at sea level, which can accelerate corrosive degradation.

The primary goal of this study is to understand how heat treatments influence the microstructure of Ni-Cr alloys and, consequently, their native oxide layer performance. Specifically, we focus on the passivation of the oxide layer that forms on the alloy's surface, which serves as an indirect measure of corrosion resistance. The study aims to determine the optimal temperature for reducing residual stresses in the material, and how this reduction is affected by the deposition pattern used during the LPBF process.

In the initial phase, the samples underwent heat treatment at varying temperatures to alleviate residual stresses. The passive layer formed on these samples was then analyzed, simulating the conditions typically encountered in aircraft engines. In the second phase, the samples were polished to further investigate the impact of temperature on the microstructure.

The study highlights that alloys containing chromium form a protective passive layer that acts as a barrier, preventing the diffusion of other alloying elements. When this layer is compromised, for instance, by high temperatures, nickel can penetrate and diffuse through the barrier, leading to the formation of nickel oxides on the surface.

The findings indicate that the temperature required for optimal performance of the native oxide layer varies with the deposition pattern of the samples. Additionally, the study observes that as the temperature increases, the grain size of all the samples grows, and the hardness of the samples inversely correlates with temperature

Contents

1. Introduction

1.1 Superalloys

Superalloys, also known as high-performance alloys, are materials engineered to withstand extreme conditions, such as high temperatures, high pressures, and corrosive environments. These advanced alloys typically consist of nickel, cobalt, or iron as their base elements, and are enhanced with various other metals to improve their properties. Due to their exceptional mechanical strength, resistance to thermal creep deformation, and excellent surface stability, superalloys are crucial in demanding applications, particularly in the aerospace, power generation, and chemical processing industries. Their ability to maintain structural integrity under stress and at elevated temperatures makes them indispensable for the performance and longevity of critical components such as jet engines, gas turbines, and nuclear reactors. [1]

Reaching optimal properties simultaneously in any material is rarely feasible. As a result, superalloy compositions are often adjusted to emphasize specific mechanical properties, potentially at the expense of oxidation/corrosion resistance. Alternatively, the properties may represent a compromise, considering manufacturability factors such as castability, forgeability, weldability, and cost. Superalloys are classified based on the primary alloying elements within their composition, with nickel, cobalt, and iron being the three fundamental metals. The entire superalloy family shares a common foundational microstructure, characterized by a face-centered cubic (FCC) matrix, with various dispersed secondary strengthening phases. Nickel, in its elemental state, is the only superalloy base metal that has an FCC structure at room temperature. The FCC structure is one of the most common types of crystal structures found in metals. In an FCC lattice, the atoms are arranged in such a way that there is one atom at each of the eight corners of the cube, as well as one atom at the center of each face of the cube. This arrangement gives the structure a high degree of symmetry and packing density. Cobalt has a hexagonally close-packed (HCP) structure at room temperature but transitions to FCC at 417 °C. Iron has a body-centered cubic (BCC) structure at room temperature but transforms into FCC austenite at 912 °C.

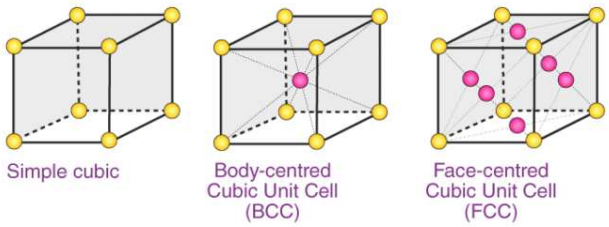

Figure 1: Examples of unit primitive cubic, body-centred cubic (BCC) or face-centred cubic (FCC). [3]

In superalloys, both iron and cobalt are stabilized by adding nickel to maintain an FCC crystal structure across the entire temperature range applicable to gas turbine engines. Superalloy is an alloy based on group VIII elements (nickel, cobalt or iron with a high percentage of nickel added) to which a multiplicity of alloying elements are added. This gives at this metal high mechanical strength and surface stability at high temperature. Superalloys are unsurpassed in terms of combination of high temperature mechanical properties and environmental resistance as shown in Figure 2.

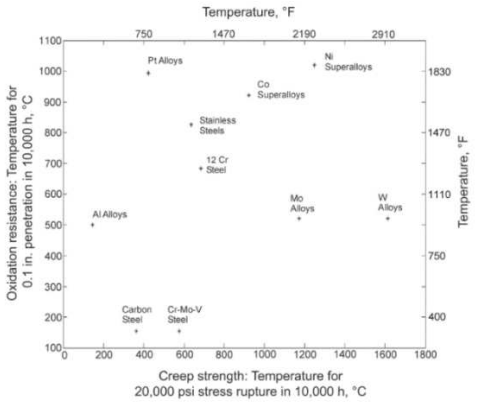

Figure 2: Environmental resistance and strength for various metallic families. [2]

1.2 Historical Development

The evolution of superalloys has been primarily driven by the need for materials that can withstand the escalating temperatures and stresses in gas turbine engines.

The first self-sustaining gas turbine engine, unveiled in Paris in 1903, included a reciprocating three-cylinder compressor and an impulse turbine. Norwegian engineer Aegidus Elling later created a gas turbine engine using a centrifugal compressor and radial turbine, generating 11 hp with a turbine inlet temperature of approximately 400 °C. This relatively low temperature allowed the use of austenitic stainless steels as structural materials. Significant advancements in gas turbine engine technology began with a collaboration between General Electric and the U.S. Army.

Around 1918, British patents were granted for Nichrome, a Ni-20Cr alloy, forming the basis for future superalloy innovations. In 1929, Bedford, Pilling, and Merica patented the addition of small amounts of titanium and aluminium to Nichrome (Nimonic 80) to enhance its strength. In 1935, Elling improved his gas turbine engine design to achieve 75 horsepower while maintaining a turbine inlet temperature of 550 °C, still within the capabilities of austenitic stainless steels.

The aircraft gas turbine engine was independently developed by Hans von Ohain and Max Hahn at the German engineering firm Ernst Heinkel. The Heinkel engine He-178, patented in 1935, became the first gas turbine engine to successfully power an aircraft by 1939, marking a significant milestone in superalloy development as turbine inlet temperatures reached 780 °C, rendering austenitic stainless steels inadequate. [1]

By the time the United States developed its first aircraft gas turbine engine in 1943, cobalt-based superalloys had already been introduced. The initial turbine blade material used was Haynes Stellite 21, initially designed as a cast alloy for dental implants.

A major advancement in superalloy development occurred in the 1950s with Eiselstein's introduction of alloy 718, a superalloy reinforced by the γ''-Ni_3Nb precipitate. From the 1930s to the 1950s, superalloy development focused on microstructure refinement. The next phase emphasized process improvements. In 1952, Falih N. Darmara pioneered commercial vacuum melting technology, leading to vacuum-melted alloys around 1955. Vacuum induction melting (VIM) facilitated the efficient incorporation of trace elements like boron, manganese, and

silicon, improving high-temperature properties, particularly ductility. Vacuum casting improved alloy performance through refined compositional control, and VIM allowed for higher levels of aluminium and titanium in the alloy, crucial for developing γ′ precipitation-hardened nickel-base superalloys.

Alternative superalloys, such as oxide-dispersion-strengthened (ODS) alloys by Dupont in 1965 and mechanically alloyed alloys by INCO in 1966, were developed. Starting in 1969, Pratt and Whitney Aircraft introduced directionally solidified alloys for airfoils. Despite the advantages of increased alloying from vacuum casting, the precipitation of detrimental phases during service highlighted the need for compositional limits based on phase stability. Elevated chromium levels were linked to the emergence of detrimental phases, prompting a reduction from around 20 to 10 weight percent in superalloy compositions, making the alloys susceptible to hot corrosion. Coatings were introduced to enhance environmental resistance, with diffusion coatings, primarily aluminium, applied to the surface of superalloy substrates. These coatings were successful, allowing turbine inlet temperatures up to 1200 °C. The first commercial use emerged in the late 1950s on cobalt-base first-stage turbine vanes, extending to nickel-base superalloy turbine blades in the 1960s. [1]

By the 1970s, superalloys with protective coatings demonstrated adequate strength, creep resistance, and environmental durability. However, the main failure mode had shifted to thermomechanical fatigue (TMF). This led to the development of a new generation of alloys designed to improve TMF resistance, optimized through advanced processing techniques like directional solidification and powder metallurgy. A significant milestone occurred in 1979 with the introduction of PWA-1480, the first commercial single-crystal (SX) superalloy, offering greater creep life and temperature capability.

Single-crystal superalloys are nearing their temperature limits at 1200 °C, with incipient melting around 1300 °C. ODS superalloys also reach their maximum useful temperatures at 1200 °C. As turbine inlet temperatures continue to rise, researchers are exploring the next generation of materials, complemented by thermal barrier coatings, to operate at even higher temperatures. [1]

1.3 Applications of Superalloys in the GTE

We can divide the applications of superalloys in the Gas Turbine Engine (GTE) in two groups:

- Stationary parts: includes combustor cans, nozzles, guide vanes, seals, and casings.
- Rotating parts: includes discs, shafts, blades, and spacers.

The combustor endures the highest temperatures within the engine while bearing limited structural loads. Superalloys such as Nimonic 75, Hastelloy X, Inconel 600, and Haynes 188 are commonly selected for this role due to their exceptional formability and weldability.

Following the combustor, the turbine vanes are the next critical components, subjected to slightly lower temperatures. However, oxidation resistance remains a significant concern. Variations in airfoil surface pressure generate stresses that necessitate careful consideration of creep resistance in material selection. A common issue is the "bowing" of the airfoil due to

creep deformation. Frequently used alloys for vane assembly include Waspaloy, X-40, alloy 713, MAR-M 302, B-1900, and columnar-grained MAR-M 200.

Turbine blades are exposed to the hot gas stream and must withstand hot corrosion and oxidation, similar to the combustor and vane surfaces. These blades also endure substantial structural loads from centrifugal and thermal stresses. Additionally, the rotating blade tips must maintain precise clearances with stationary components to enhance engine efficiency, necessitating highly creep-resistant alloys. Hot corrosion due to salt deposits is another critical issue, particularly in marine atmospheres where sulfur from fuel impurities reacts with airborne sea salts to form sodium sulfate.

Turbine disks are designed for high static strength, fatigue resistance, and toughness. Although they do not experience temperatures as high as turbine blades, they still require robust materials. Alloys commonly used for turbine disks include Incoloy 901, Waspaloy, Astroloy, A-286, and Inconel 100. Superalloys are classified according to main alloying elements in the composition, with three base metals being nickel, cobalt, and iron. The entire superalloy family shares a common microstructure that is a face-centerer cubic FCC matrix. In elemental form, nickel is the only superalloy base metal with an FCC structure at room temperature. Cobalt is hexagonally close-packed (hcp) at room temperature but undergoes a transformation to FCC at 417 °C. In superalloys, both iron and cobalt are stabilized by the addition of nickel. [1]

Inconel 625 nowadays is widely used in various critical aerospace components due to its excellent heat, corrosion, and oxidation resistance. Here are some specific examples of aircraft and applications where this alloy is used:

1. **Jet engine exhaust systems**: Components like exhaust ducts and jet nozzles, which are exposed to extreme temperatures, are often made from Inconel 625. For instance, this alloy is used in military aircraft like the Northrop Grumman EA-6B Prowler of the U.S. Navy. [41]
2. **Turbine and engine components**: it is utilized in turbines to withstand high temperatures and mechanical stress. It is found in thrust-reverser systems and turbine shroud rings of jet engines. [42] [43]
3. **Aircraft ducting systems**: Modern aircraft use Inconel 625 in air ducting systems, including applications such as anti-icing systems and heat management in engines. [43]

1.4 Nickel-Base Superalloys

Nickel-based superalloys, emphasizing their optimal combination of temperature resistance and strength, making them well-suited for high-temperature applications such as turbine blades. The superior temperature capability of these alloys is attributed to the precipitation of the γ'-Ni_3 (Al, Ti) phase. Nickel-based superalloys exhibit a unique combination of high temperature and strength properties, enabling their use in components that must endure extreme conditions over extended periods.

Wrought nickel-based superalloys are frequently employed in applications where high toughness is essential, such as turbine discs and forged blades, where the material's resistance to mechanical failure is critical.

On the other hand, cast nickel-based superalloys are preferred for their high strength and superior creep resistance, making them ideal for components that must retain their shape and integrity under prolonged exposure to high temperatures and mechanical loads.

1.4.1 Strengthening Mechanisms

Superalloys are strengthened through these principal mechanisms:

- Solid-solution hardening (SSH)
- Precipitation hardening (PH)
- Dispersion strengthening

The grain size refinement could be another strengthening mechanism but is rarely used due to the high temperature environment. There is usually one dominate mechanism, between SHH, PH, Oxide and carbide dispersion strengthening, in the same alloy. Further improvement of mechanical properties is enabled by the control of the grain structure.

Solid-Solution Hardening (SSH)

Solid-solution hardening is the attainment of an increase in matrix strength by the addition of a different soluble element. The distortion of the atomic lattice, that increases with different size, caused by the misfit of atomic radius inhibits dislocation movement.

To limit the diffusion and provides a stronger lattice cohesion, it's possible use high-melting-point elements. Another effect of decreasing the stacking fault energy in the crystal lattice which is the main deformation mode in imperfect crystals at elevated temperatures.

A lower Stacking Fault Energy (SFE) makes it more difficult for dislocation to change directions, when a dislocation encounters a barrier, it's more difficult for the dislocation to be able to bypass that barrier by moving onto a new slip plane. Another mechanism that contributes to strength is called atomic clustering or short-range. Its effect is related to the electronic orbitals and is observed more strongly for certain elements, including molybdenum, tungsten, chromium, alumina, and rhenium that produce an enhanced hardening effect in a nickel matrix compared with iron, titanium, cobalt, or vanadium.

Precipitation Hardening (PH)

The PH is used to avoid the risk of alloy to creep during the application on high temperature. For example, in the case of nickel-base alloys, this can be achieved using elemental additions such as titanium, aluminium, and niobium. The heat treatment can generate finely distributed precipitates in the matrix from a supersaturated solid solution. The precipitates, which are generally coherent intermetallic compounds such as γ'-$Ni_3(Ti,Al)$ or γ''-Ni_3Nb phase, can inhibit the movement of dislocations.

The four main factors controlling the effectiveness of PH are:

- Coherency strains between the matrix (γ) and the precipitate (γ', γ'') due to the difference in their lattice parameters
- Antiphase-boundary (APB) energy in the presence of an ordered precipitate (γ', γ''). The APB represents the energy needed for the dislocation to cut through the ordered

precipitate, because cutting could result in disordering between the matrix and precipitate.
- Volume fraction of the precipitate (γ', γ'')
- Particle size

Oxide Dispersion Strengthening (ODS)

Oxide dispersion strengthening is a mechanism like PH, except that the strengthening agent is added to the alloy and not precipitated from the matrix. The production of ODS alloys is complicated by the fact that the density of ceramics is lower than the metal matrix. The ceramic particles tend to float to the surface of the molten metal during casting, thus diminishing the strengthening effect.

For this reason, ODS alloys are product by combination of mechanical alloying, powder metallurgy and subsequent thermomechanical processing. Oxides are always incoherent respect the matrix, so oxide additions cause strengthening through the Orowan bypassing mechanism. Grain-boundary strengtheners as well as SSH are also usually incorporated in mechanically alloyed alloys, for example, Inconel MA760 and Inconel MA-6000.

Carbide Hardening

In alloy systems in which SSH elements such as molybdenum and tungsten have limited solubility, carbides are often used to provide high temperature strengthening.

Carefully designed carbide hardening can be particularly useful for increasing creep strength, because under service loads, the high-temperature creep processes mainly take place at the grain boundaries. Carbides, precipitated preferentially at the grain boundaries, inhibit grain-boundary slip, transferring creep processes from the grain boundary to the interior of the grain, where diffusion is slower.

The primary carbides assume the formula of MC and M_6C, with “M” representing molybdenum, tungsten, titanium and niobium that they become $M_{23}C_6$ with prolonged exposure to high temperatures. This type of carbides ($M_{23}C_6$) is often cohesive and form along grain boundaries.

1.5 Phases, microstructure and Compositional Effects

The gamma matrix phase, with its face-centered cubic (FCC) structure, forms the backbone of the alloy. Within this matrix, precipitates are embedded to enhance the mechanical properties. This FCC structure is highly advantageous for high-temperature applications due to its superior mechanical characteristics, such as tensile strength, rupture resistance, creep resistance, and thermomechanical fatigue resistance. These benefits stem from the presence of numerous slip systems in the FCC lattice.

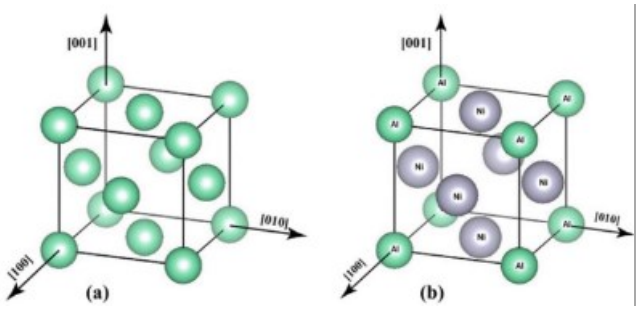

Figure 3: Unit cell of (a) FCC crystal and (b) ɤ' phase. [5]

The densely packed FCC matrix is particularly suited for high-temperature operations (relative to the material's melting point, $\frac{T}{T_M}$) because of the low diffusivity of alloying elements within the structure. Additionally, the FCC matrix has a high solubility for secondary elements, which aids in the precipitation of strengthening intermetallic compounds like γ′ and γ″ and allows for the dissolution of high-melting-point refractory elements.

In the FCC lattice, atoms are located at each of the corners and the centers of all the faces of the cube. This creates a cubic unit cell where:

- Corners: Atoms at each of the eight corners of the cube.
- Faces: Atoms at the center of each of the six faces of the cube.

The FCC structure has a high packing efficiency. The Atomic Packing Factor (APF) is about 0.74, meaning that 74% of the volume is occupied by atoms, and the rest is void space. This is one of the highest packing factors among crystal structures. In FCC, each atom has a coordination number of 12, meaning it is in contact with 12 neighbouring atoms. [9]

The matrix phase primarily consists of the base metal of the superalloy, such as nickel, along with a significant concentration of solid-solution-strengthening elements like cobalt, chromium, molybdenum, tungsten, tantalum, and rhenium. These elements play a crucial role in enhancing the matrix's overall strength through solid-solution hardening. The predominant component in the composition of the matrix phase is the base metal of the superalloy, complemented by a significant proportion of solid-solution elements like cobalt (or nickel in cobalt-based superalloys), chromium, molybdenum, tungsten, tantalum and rhenium. These elements contribute to solid-solution hardening within the matrix. [5]

Crystal Structure of phases in Alloy 625

Alloy 625 compromises a nickel-base solid solution as a matrix phase that may contain a variety of intermetallic and carbide phases. The Table below lists crystallographic features of various phases that usually form in Alloy 625.

Phase	Common structure type[a]	Pearson's symbol	Space group	Prototype	Formula	Crystal structure	Atoms per unit cell	Lattice parameters[b] (nm)			Angle (°)
								a	*b*	*c*	
Gamma (γ)	A1	cF4	Fm-3 m	Cu	Ni	Face-centered cubic	4	0.3609	0.3609	0.3609	90°
Gamma double prime (γ'')	$D0_{22}$	tI8	I4/mmm	Al_3Ti	$Ni_3(Nb,Ti,Al)$	Ordered body-centered tetragonal	8	0.362	0.362	0.741	90°
$Ni_2(Cr, Mo)$	D_{2h}^{25}	oP6	Pmmm	Pt_2Mo	$Ni_2(Cr,Mo)$	Ordered body-centered orthorhombic	6	0.2513	0.7553	0.3580	90°
Delta (δ)	$D0_a$	oP8	Pmmn	β-Cu_3Ti	Ni_3Nb	Ordered body-centered orthorhombic	8	0.5116	0.426	0.4565	90°
$M_{23}C_6$ Carbide	$D8_4$	cF116	Fm-3 m	$Cr_{23}C_6$	$Cr_{23}C_6$	Complex cubic	116	1.050–1.070	1.050–1.070	1.050–1.070	90°
M_6C Carbide	$E9_3$	cF112	Fd-3 m	Fe_3W_3C	$(Cr,Mo,Ni)_6C$	Complex cubic	112	1.091–1.13	1.091–1.13	1.091–1.13	90°
MC Carbide	B1	cF8	Fm-3 m	NaCl	(Nb,Ti)C	Cubic	8	0.430–0.444	0.430–0.444	0.430–0.444	90°
Mu (μ) Phase	$D8_5$	hR13	R-3 m	W_6Fe_7	Mo_6Ni_7	Hexagonal	39	0.48	0.48	2.56	γ = 120°
Laves Phase	C14	hP12	$P6_3/mmc$	Zn_2Mg	$(Cr,Ni)_2(Si,Nb,Mo)$ Ni_3Mo_2Si	Hexagonal	12	0.47–0.48	0.47–0.48	0.77–0.78	γ = 120°

[a]The "common structure type" is based on the Strukturbericht designation commonly used to describe frequently encountered similar types of crystal structures
[b]The range signifies that the lattice parameter values vary with composition
[c]The reported lattice parameter of the $Ni_2(Cr, Mo)$ phase in a model Ni–Cr–Mo alloy containing Cr and Mo solutes equivalent to the amount present in Alloy 625

Table 1: Crystallographic details of various phases that may form in Alloy 625 [5]

Phase ɤ

The gamma phase (γ) in Ni-Cr based alloys is the primary matrix phase, it serves as the backbone of the alloy, providing excellent mechanical properties such as high strength, ductility, and thermal stability. The gamma phase is capable of dissolving significant amounts of alloying elements, including chromium, molybdenum, and cobalt, which further enhance its mechanical properties. Within this matrix, secondary phases like γ′ (Ni_3Al) and γ″ (Ni_3Nb) precipitate, strengthening the alloy and improving its resistance to high-temperature deformation, creep, and fatigue. The gamma phase plays a crucial role in maintaining the alloy's structural integrity under extreme operating conditions. [8]

Phase ɤ'

The gamma prime phase (γ') is a coherent, ordered precipitate that forms within the matrix of the gamma phase (γ). γ' phase typically has a face-centered cubic (FCC) structure, but with a different atomic arrangement compared to the γ phase. This is often composed of nickel and a precipitating element such as aluminium (Al), titanium (Ti), or both. For example, in Ni-based superalloys, it is commonly represented by the formula $Ni_3(Al, Ti)$, indicating a composition of nickel and aluminium or titanium in a 3:1 ratio. [1]

The γ' phase significantly enhances the mechanical properties of the alloy and contributes to the thermal stability of the alloy. It impedes dislocation movement, thereby increasing the alloy's high-temperature strength and creep resistance. The γ' phase forms during the heat treatment process of the alloy. It typically precipitates out of the γ phase during aging at elevated temperatures. The size, distribution, and volume fraction of γ' precipitates can be controlled through heat treatment processes to optimize the mechanical properties of the alloy. [10] [11]

Phase ɤ"

The γ" phase typically has a body-centered tetragonal (BCT) structure. In nickel-based superalloys, the γ" phase is often represented by Ni_3Nb (nickel-niobium) or similar

composition usually contains nickel and elements such as niobium (Nb), titanium (Ti), or aluminium (Al). [1]

The γ'' phase contributes to strengthening the alloy by impeding dislocation motion, enhancing the material's high-temperature strength and creep resistance. It also improves the thermal stability of the alloy, which is crucial for high-temperature applications.

γ'' phase forms during heat treatment processes, typically at lower temperatures compared to the γ' phase. It precipitates within the γ matrix, and its formation can be influenced by the alloy's composition and heat treatment conditions. It precipitates as fine, rod-like or needle-like particles, which are different in morphology from the γ' phase. [12]

Phase δ

The delta phase has an orthorhombic crystal structure and is commonly based on Ni_3Nb, a combination of nickel and niobium, although chromium can influence its formation in Ni-Cr alloys. The delta phase is closely related to the gamma-prime (γ') phase, another common phase in nickel-based superalloys, although it has different structure and properties. The delta phase tends to form during prolonged heat treatments or exposure to intermediate temperatures (around 700-900 °C) in Ni-Cr superalloys that contain strengthening elements like niobium or titanium. Its formation is favoured in alloys where alloying additions lead to oversaturation and the decomposition of the stable γ (gamma) phase. The delta phase can be used to control grain size in alloys during hot-working processes. It can act as a barrier to grain boundary movement, improving high-temperature stability.

Although the delta phase does not directly contribute to the mechanical strength of the alloy like the γ' phase, its presence in certain amounts can influence the ductility and deformation resistance of the alloy, limiting grain growth and improving long-term properties.

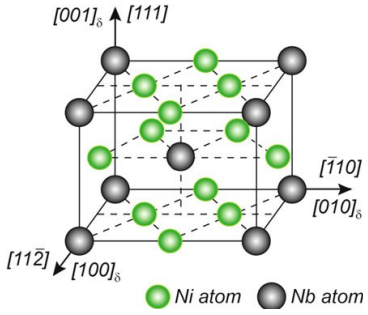

Figure 4: The unit cell of the D0a structure of the δ phase. [5]

Carbides

There are different types of carbides like:

- MC Carbides: These are typically simple carbides where M is a metal such as chromium (Cr) or titanium (Ti). Examples include Cr_3C_2 and TiC. MC carbides are usually found in the as-cast state of the alloy and are relatively coarse.
- M_6C Carbides: These are complex carbides where M is typically chromium (Cr), and the formula is M_6C. They form during heat treatment and are generally finer than MC carbides.

– $M_{23}C_6$ Carbides: These are a type of complex carbide where M is usually chromium (Cr) and the formula is $M_{23}C_6$. These carbides often form during aging and are responsible for additional hardening of the alloy.

Carbides form during the solidification and heat treatment of Ni-Cr-based alloys. The specific types of carbides and their distribution depend on the alloy composition and heat treatment conditions. They can be distributed throughout the matrix or at grain boundaries. The size, shape, and distribution of carbides influence the mechanical properties of the alloy. Carbides significantly enhance the hardness and wear resistance of Ni-Cr-based alloys. They act as a reinforcement phase within the matrix, they also contribute to the stability of the alloy at high temperatures by inhibiting grain growth and maintaining structural integrity. [13]

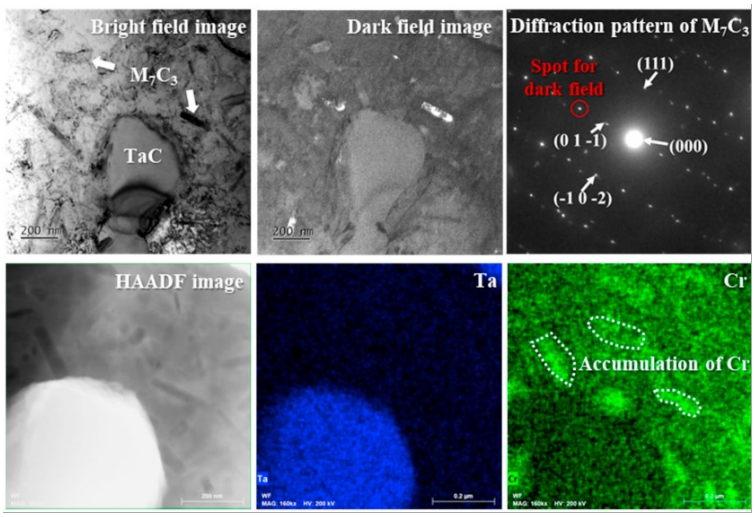

Figure 5: TEM morphology and element distribution of carbide in NiCrTa alloy [14]

Topologically Close-Packed Phases

In the context of nickel-chromium (Ni-Cr) based superalloys, significant efforts are made to avoid composition ranges that could lead to the formation of topologically close-packed (TCP) phases during heat treatment or operational use. TCP phases are generally undesirable because they can adversely affect the alloy's performance.

TCP phases are characterized by densely packed atomic layers, with these layers interspersed by other layers containing relatively larger atoms. This packing arrangement often results in platelike or needle-like microstructures. The most common TCP phases observed in Ni-Cr based superalloys include:

- σ (Sigma) Phase (AxBy): Where "A" could be elements such as nickel (Ni), chromium (Cr), or iron (Fe), and "B" could be elements like molybdenum (Mo), tantalum (Ta), or niobium (Nb). The σ phase is known for its detrimental effect on mechanical properties, including rupture strength and ductility.
- μ (Mu) Phase (Ax′By′): This phase also features a complex structure, where "A" and "B" elements are like those in the σ phase but in different proportions. The μ phase can contribute to reduced high-temperature stability and mechanical performance.

- Laves Phase (A_2B): Characterized by a body-centered cubic structure, where "A" elements are typically nickel (Ni), cobalt (Co), or iron (Fe), and "B" elements are chromium (Cr), molybdenum (Mo), or tantalum (Ta). The Laves phase can cause embrittlement and a decrease in the alloy's overall toughness.

The presence of these TCP phases in Ni-Cr based superalloys can lead to a reduction in the material's rupture strength and ductility, thereby compromising its performance in high-temperature and high-stress applications. As such, controlling the alloy composition and heat treatment processes is crucial to minimizing the formation of these undesirable phases. [1]

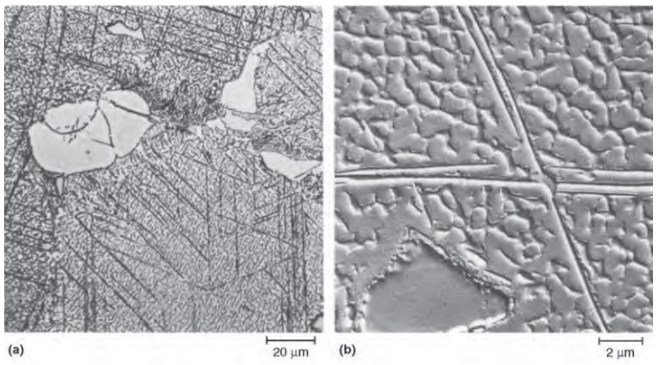

Figure 6: IN-100 nickel-base alloy casting, held at 815°C for 5000h. (a) Structure consists of massive MC particles, platelets of σ phase, and primary and precipitated γ ' in the γ matrix. (b) Replica-electron micrograph shows a massive particle of MC, Widmanstätten platelets of σ phase, and γ ' in the γ matrix.[1]

Protective Oxide

In nickel-chromium (Ni-Cr) based alloys, protective oxides play a crucial role in enhancing the alloy's resistance to oxidation and corrosion, especially at high temperatures. These oxides form a thin, stable layer on the surface of the alloy, which acts as a barrier against further oxidation and deterioration. When Ni-Cr based alloys are exposed to high temperatures, they react with oxygen to form a protective oxide layer. The primary oxides in these alloys are typically chromium oxides (Cr_2O_3) and nickel oxides (NiO).

- Chromium Oxide (Cr_2O_3): Chromium is the main element responsible for the formation of a stable and protective oxide layer. Cr_2O_3 forms a dense, adherent layer on the alloy surface, which prevents further oxidation of the underlying metal. The chromium oxide layer is highly effective in blocking the diffusion of oxygen into the alloy, thus preventing further oxidation of the metal.
- Nickel Oxide (NiO): Nickel oxide also forms but is generally less protective than chromium oxide. It may contribute to the overall oxidation resistance but is not as critical as Cr_2O_3.

This oxide layer is typically stable at high temperatures and helps to maintain the mechanical properties of the alloy, such as strength and ductility. Over time, the protective oxide layer can become compromised due to factors such as high temperature, high pressure, or exposure to aggressive environments.

1.5.1 Alloy 625

Alloy 625, also known as Inconel 625, is a nickel-based superalloy distinguished by its exceptional combination of high strength, superior corrosion resistance, and high-temperature stability. This alloy primarily consists of nickel, with a minimum of 58%, chromium ranging from 20 to 23%, molybdenum between 8 and 10%, and niobium from 3.15 to 4.15%. The specific composition of Alloy 625 contributes to its unique properties, including outstanding resistance to a wide variety of corrosive environments, such as acidic and alkaline conditions, and resistance to pitting and crevice corrosion. This precipitation process significantly complicates the microstructure of the alloy and alters its properties. However, the presence of elements like chromium, molybdenum, and niobium leads to the precipitation of multiple phases during various stages such as solidification, processing, and thermal exposure.

The transformation from cubic to non-cubic phases during precipitation affects the distribution and morphology of particles within the matrix. These transformations result in several crystallographic orientations of the precipitating phases, referred to as "variants," with their number determined by the reduction in lattice symmetry due to the transformation. [7]

Alloy 625 is particularly noted for its ability to maintain mechanical strength at elevated temperatures, up to approximately 982°C. Unlike some superalloys, it does not undergo phase transitions at high temperatures, which ensures its structural integrity and performance under thermal stress. Additionally, the alloy exhibits excellent weldability, eliminating the need for post-weld heat treatment, which simplifies its fabrication and repair processes. This property is advantageous in applications requiring complex welding. Furthermore, Alloy 625 is renowned for its high resistance to fatigue and creep deformation, even under conditions of extreme thermal cycling. This makes it suitable for demanding applications in aerospace and industrial sectors where long-term reliability is essential. [5]

Below a summary of the effects of various alloying elements on Alloy 625:

- **Nickel** (Ni): Nickel is the primary element, providing phase stability and allowing Alloy 625 to accommodate other alloying elements without phase instability. It also improves high-temperature properties and stress-rupture strength.
- **Chromium** (Cr): Chromium contributes to corrosion resistance by forming a protective chromium oxide (Cr_2O_3) layer. It also enhances strength and prevents undesirable phase formation up to certain concentrations.
- **Molybdenum** (Mo): Molybdenum strengthens the matrix through solid-solution hardening and increases resistance to localized corrosion. It also improves creep resistance.
- **Iron** (Fe): Iron is not particularly beneficial in Alloy 625 and is generally minimized to avoid promoting the formation of deleterious phases.
- **Carbon** (C): Carbon plays a role in carbide formation (MC, $M_{23}C_6$) during solidification and heat treatment. Keeping carbon levels low (below 0.1%) is important to prevent detrimental carbide formations.
- **Manganese** (Mn): Small amounts of manganese help mitigate the effects of sulfur by forming sulfides, which reduce the embrittlement.
- **Silicon** (Si): Silicon promotes the formation of carbides and can influence the microstructure, especially in promoting the formation of the Laves phase. Its levels must be kept low to avoid excess carbide formation.

- **Niobium** and **Tantalum** (Nb + Ta): Niobium improves the strength of the alloy, especially at elevated temperatures, by promoting the formation of the γ″ phase (Ni_3Nb). It also enhances creep resistance.
- **Titanium** (Ti) and **Aluminium** (Al): These elements are used in small amounts to avoid excessive hardening but contribute to solid-solution strengthening and improve creep properties.
- **Phosphorus** (P) and **Sulfur** (S): Both elements are detrimental in high concentrations. Sulfur reduces workability and forms low-melting eutectics, while phosphorus can enhance creep resistance in small quantities but should be minimized.

1.6 Additive Manufacturing

In the context of additive manufacturing (AM) for a Ni-Cr-based alloy, such as nickel-based superalloys, AM refers to a layer-by-layer process that allows the creation of complex parts. One of the most widely used AM techniques for these materials is Powder Bed Fusion (PBF), which uses either laser (L-PBF) or electron beams (E-PBF) to melt and fuse metal powder into the desired shape. AM for Ni-Cr alloys offer several advantages like the fact it allows for intricate part designs that are difficult or impossible to achieve with traditional methods, reduced Material Waste and we have shorter production time.

Nickel-based superalloys, such as Inconel 625, are commonly processed using AM because they provide excellent mechanical properties, corrosion resistance, and high-temperature strength. However, producing these alloys via AM requires careful control of process parameters to manage microstructural features, such as grain structure and the formation of strengthening phases like γ' and γ. [16]

1.6.1 Laser Powder Bed Fusion L-PBF

L-PBF (Laser Powder Bed Fusion) is an additive manufacturing (AM) process that uses a high-powered laser to selectively melt and fuse metal powder layer by layer. In L-PBF, a thin layer of metal powder is spread over a build platform, and the laser traces a predefined pattern based on the part's design, melting the powder to form a solid structure. This process is repeated, layer by layer, until the entire part is built.

Figure 7 illustrates the process, a form of additive manufacturing used to build metal parts layer by layer. In this process, a thin layer of metal powder (such as Inconel 625) is spread across a build platform. A high-energy laser then selectively melts specific areas of the powder based on the part’s design, as dictated by a CAD model. As the laser moves, it melts the powder, forming a small molten pool that solidifies into a solid layer as it cools. Once one layer is complete, the build platform lowers slightly, and a new layer of powder is spread on top. The laser again melts the powder, fusing the new layer to the previous one. This process continues, with the part being constructed layer by layer. The LPBF method allows for the creation of highly complex geometries, including intricate internal features, which would be difficult to achieve with traditional manufacturing techniques. Once the part is fully formed, excess powder is removed, and the part may undergo further post-processing to improve its properties and ensure its quality. [44]

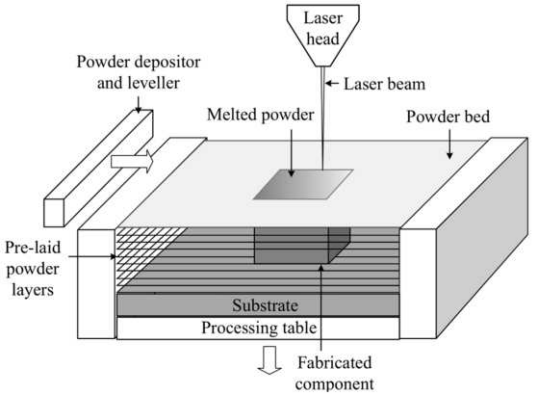

Figure 7: Schematic diagram of laser powder bed fusion (LPBF) technology.[44]

There are numerous parameters that must be taken into consideration including:

- **Laser Power**: This is a critical parameter that controls the energy transfer from the L-PBF system to the powder bed, ensuring consistent and controlled melting of the material. By increasing laser power, the energy input becomes more efficient, which typically enhances the melting of the powder, leading to better densification of the final part. Higher laser power results in more robust fusion between powder particles, producing denser, higher-quality components. However, the challenge lies in balancing this with cost-efficiency. Excessive laser power can drive up production costs due to increased energy consumption and potential overheating, which may lead to defects such as excessive melt pool size or spatter formation. Therefore, optimizing laser power is essential to achieve high part quality while minimizing costs. [16]
- **Scan Path**: The path followed by the laser, such as linear, serpentine, or more complex patterns like chessboard or stripes, impacts how heat is spread across the layers. More complex patterns, like a chessboard or island strategy, can help distribute heat more evenly, reducing thermal stresses and improving mechanical properties. However, these strategies can also increase build time. [17]
- **Scan Rotation**: Rotating the scan direction between layers (e.g., by 90 or 67 degrees) can help reduce anisotropy in the mechanical properties by promoting more isotropic grain growth and reducing the alignment of defects like cracks or pores in a single direction. [17]
- **Scan Speed**: This refers to the rate at which the laser moves across the powder bed. It plays a significant role in both build speed and the quality of the component. A slower scan speed allows the laser to dwell longer on each point of the powder bed, delivering more energy and promoting deeper melting, which can lead to better layer bonding. However, excessively slow speeds may cause over-melting, leading to defects such as warping or porosity. On the other hand, very high scan speeds can reduce energy input, resulting in incomplete melting and poor layer adhesion. Thus, finding the right balance between scan speed and laser power is crucial for ensuring uniform melting and optimal mechanical properties in the finished part.
- **Hatch Distance**: This is the distance between adjacent laser tracks as the beam passes over the powder bed. Hatch distance controls how uniformly the powder bed is heated, influencing the thermal profile across the build. If the hatch distance is too wide, regions of the powder may not receive enough energy, leading to incomplete melting and voids between layers. Conversely, a hatch distance that is too narrow can cause excessive heat concentration, potentially resulting in thermal stresses and warping. Optimizing the hatch

spacing is essential to ensure even energy distribution, proper melting, and a smooth surface finish, which in turn improves part quality and mechanical performance.

- **Layer Thickness**: The thickness of each deposited powder layer directly influences build time and the overall mechanical properties of the component. Thicker layers can speed up the construction process but may reduce the precision and quality of the part. The reduced precision arises from less accurate energy distribution across thicker layers, leading to uneven melting and poor inter-layer bonding. Moreover, mechanical properties like impact toughness and elasticity also degrade as the layer thickness increases, due to incomplete fusion and higher residual stresses. Therefore, controlling layer thickness is vital for maintaining the desired balance between build speed and the mechanical integrity of the part. [16]

1.6.2 Sample types

In my study we focused on Ni-Cr alloy produced with additive manufacturing (L-PBF), produced with various laser scanning strategies used during the fabrication process. The differences between these scanning strategies can significantly influence the microstructure, residual stresses, porosity, and overall mechanical properties of the alloy. Below is a list of the samples and their main properties of the study:

1. **Conventional**: refers to a standard or default scanning strategy, such as a simple linear or serpentine path where the laser moves back and forth across the powder bed layer. This strategy might result in predictable but potentially anisotropic mechanical properties, with some risk of thermal stress buildup in specific directions.
2. **Nopat40**: indicate no pattern or no repetitive pattern, combined with a rotational element. The numbers 40 refer to the degree of rotation between layers. For example, in nopat40, the laser path might rotate 40 degrees between layers. Rotating the scan pattern helps reduce anisotropy and distribute thermal stresses more evenly, leading to more uniform microstructures.
3. **Nopat180**: indicate no pattern or no repetitive pattern, combined with a rotational element. The numbers 180 refer to the degree of rotation between layers. For example, in nopat 180 degrees essentially it is reversing the scan direction. Rotating the scan pattern helps reduce anisotropy and distribute thermal stresses more evenly, leading to more uniform microstructures.
4. **Stripes**: refers to a scanning strategy where the laser moves in distinct parallel bands or stripes across the build area. The stripes strategy can concentrate heat in specific regions, which may help with localized bonding but can also introduce thermal gradients, affecting grain growth and potentially leading to anisotropy or internal stresses.
5. **Chess**: The chessboard strategy involves dividing the powder bed into square or rectangular segments, where the laser scans each segment in an alternating pattern. This strategy is effective in distributing heat more evenly across the part, minimizing thermal stress accumulation and reducing the risk of warping or cracking. It can also promote more isotropic mechanical properties due to the uniform distribution of heat across different areas. [18]

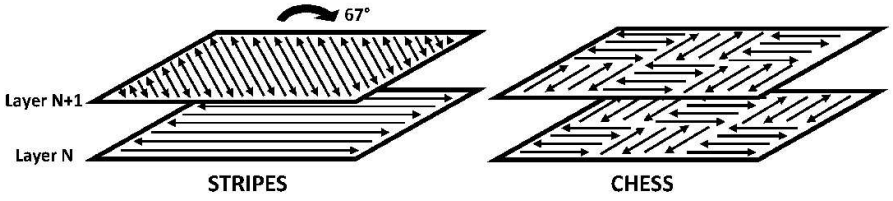

Figure 8: Stripes and Chess laser strategies used for producing the samples.[19]

1.7 Heat Treatments

Mechanical and physical properties of metals and alloys are significantly influenced by heat treatment processes. These processes involve subjecting the materials to precise temperature cycles, followed by carefully controlled cooling rates, with the goal of refining their internal structure and improving properties such as hardness, strength, ductility, fatigue life, and resistance to corrosion.

A typical heat treatment procedure is composed of three key phases: heating, holding at a target temperature (also referred to as soaking), and cooling. Depending on the alloy and the specific performance requirements, both the temperature and the duration of each phase can vary considerably. Advanced heat treatment techniques are rooted in principles of thermodynamics, reaction kinetics, and crystallography, enabling engineers to adjust the microstructure at the atomic and grain level. These modifications allow for tailoring material properties to meet the demanding requirements of various industrial applications, from aerospace components to cutting tools. Additionally, modern innovations in heat treatment, such as cryogenic treatment or induction hardening, further expand the range of achievable material characteristics.

1.7.1 Annealing Treatment

Annealing is a heat treatment process used to soften work-hardened alloys by heating them to a specific temperature and then cooling them at a controlled rate. This process increases the alloy's ductility for easier forming and machining, relieves internal stresses, and can produce other desirable changes in material properties.

For Alloy 625, annealing is typically performed at around 980 °C, though this can vary depending on factors like the extent of cold work and the duration of heating. During annealing, recrystallization occurs, which softens the alloy but also reduces its mechanical strength. If the alloy is heated above 1000 °C, significant grain growth can occur, as carbides dissolve and the grains enlarge, which is less desirable for applications requiring good fatigue strength. To counteract grain coarsening, the alloy may need to be reworked and annealed again to achieve a fine-grained structure. [5]

For annealing Alloy 625, a dry, protective atmosphere is essential to prevent oxidation and maintain a bright surface. A 100% hydrogen environment is ideal, with a dew point of −50 °C or lower, to reduce chromium oxide and protect the alloy from oxidation. Residual hydrocarbons in hydrogen should be minimized to avoid carburizing. Alternative gases like nitrogen or dissociated ammonia are less effective and may cause nitride formation. During

annealing, the hydrogen atmosphere must be at positive pressure to prevent dangerous reactions with air. Proper purging of the chamber with inert gas before heating is also crucial to avoid fires or explosions. [5]

1.7.2 Homogenization Treatment

In Ni-Cr based alloys, homogenization treatment is used to reduce or eliminate chemical segregation by allowing diffusion to occur when the alloy is heated above the solution annealing temperature. However, the homogenization temperature must be kept below the alloy's incipient melting point. This temperature is influenced by both equilibrium and non-equilibrium phases formed by segregating elements during solidification.

For Alloy 625, the incipient melting temperature is approximately 1288 °C, and homogenization is typically recommended at temperatures between 1200 and 1250 °C. The duration of the homogenization process depends on the level of inhomogeneity present. However, homogenization becomes increasingly less cost-effective when temperatures exceed 1200 °C. This process is particularly important for cast structures where thermo-mechanical processing cannot be applied.

1.7.3 Precipitation Treatment

Precipitation treatments are designed to induce the formation of strengthening phases from a supersaturated matrix and to control carbide phases in alloys. For Ni-Cr based alloys, such as Alloy 625, the choice of precipitation temperature and duration can vary greatly, as it depends on factors such as the size, distribution, volume fraction, and density of the precipitating particles. When multiple phases precipitate from the matrix, careful selection of the aging temperature becomes crucial.

Alloy 625 is primarily a solid solution strengthened alloy, but it also undergoes precipitation of various hardening phases at intermediate temperatures. These phases precipitate homogeneously as sub-microscopic particles throughout the grains, leading to a significant increase in hardness and strength. The precipitation reactions and their temperature ranges for forming different phases in Alloy 625 are summarized in Table 2. Unlike some γ′-strengthened alloys, such as Alloy 693, where hardening phase precipitation occurs more readily, Alloy 625 experiences delayed precipitation due to longer incubation periods. However, these incubation times and precipitation temperatures can be reduced by subjecting the alloy to deformation prior to precipitation.

Temperature range	Precipitation reaction	Aging duration
$T \leq 600$ °C	$\gamma_s \rightarrow \gamma + Ni_2(Cr, Mo)$	Prolonged aging
600 °C < T ≤ 650 °C	$\gamma_s \rightarrow \gamma + Ni_2(Cr, Mo) + \gamma''$	Prolonged aging
650 °C < T < 750 °C	$\gamma_s \rightarrow \gamma + \gamma''$	Short aging
650 °C < T < 750 °C	$\gamma_s \rightarrow \gamma + \gamma'' + \delta$	Prolonged aging
750 °C < T < 800 °C	$\gamma_s \rightarrow \gamma + \gamma'' + \delta$	Short aging
750 °C < T < 800 °C	$\gamma_s \rightarrow \gamma + \delta$	Prolonged aging
T > 800 °C	$\gamma_s \rightarrow \gamma + \delta$	Short aging

γ_s Refers to supersaturated γ phase

Table 2 Precipitation sequence of different intermetallic phases in Alloy 625 [5]

1.7.4 Stress-Relieving Heat Treatments for Inconel 625

During the LPBF process, the intense interaction between the laser beam and powder layers often leads to defects, primarily due to the generation of high residual stresses. Such defects, including cracks, layer delamination, warping, and porosity, can significantly affect the quality and mechanical performance of components produced by 3D printing.

Residual stress refers to the stress that remains in a material after it has undergone manufacturing processes, such as heating and cooling. In LPBF, the material powder is melted layer by layer using a high-energy laser, which creates steep temperature gradients across the layers. These gradients contribute to the accumulation of residual stresses within the material. The rapid heating and cooling cycles typical in LPBF further increase the risk of developing these stresses.

minimize residual stress in LPBF-fabricated Inconel 625 components, stress-relief heat treatment is commonly applied. This process involves heating the material to moderate temperatures and then cooling it slowly, which helps reduce the internal stresses without significantly altering the microstructure. For Inconel 625, stress relief is typically carried out at temperatures between 870 °C and 900 °C, followed by air or furnace cooling. The effectiveness of the stress-relieving process is influenced by both temperature and duration, with higher temperatures reducing the required treatment time.

Careful control of the heat treatment parameters is essential to prevent excessive grain growth or unwanted microstructural changes in Inconel 625. By optimizing the stress-relieving process, the material retains its mechanical properties, such as high tensile strength and corrosion resistance, which are crucial for high-performance applications.

1.7.5 Water quenching

Water quenching is used to rapidly cool the alloy down to prevent the formation of secondary phases, such as carbides or topologically close-packed (TCP) phases, which can degrade its mechanical properties and corrosion resistance. When the alloy is quenched down to around 500°C, this quick cooling locks in the high-temperature, solid solution microstructure,

effectively “freezing” the alloy’s composition in a state that maximizes its ductility, tensile strength, and resistance to localized corrosion.

However, water quenching also introduces challenges. Rapid cooling can induce significant internal stresses, especially in thick or complex geometries, which may lead to warping, microcracking, or dimensional changes in some components. For larger parts, it may be advisable to combine water quenching with other techniques, such as stress-relieving treatments, to minimize these effects.

Water quenching to 500°C is particularly beneficial because it maintains the alloy's resistance to stress corrosion cracking and enhances its stability in harsh environments without additional phase transformation. In applications where long-term thermal stability is required, such as turbine blades, exhaust systems, and chemical reactors, water quenching provides a practical solution for maximizing Inconel 625’s performance in extreme conditions.

1.8 Corrosion and Passive layer

1.8.1 General Principles

The driving force behind metal corrosion is a natural consequence of their temporal existence in metallic form. Indeed, to achieve the necessary metallic state, the various compounds present in nature absorb and store the energy required to release the metallic elements from their original compounds. The amount of energy stored varies from metal to metal, and this stored energy subsequently returns to the environment through corrosion, which is a spontaneous process. There are two categories of corrosion:

- Wet corrosion: which occurs when the metal is exposed to an environment containing a liquid electrolyte, typically water. This is an electrochemical process that takes place at the metal-electrolyte interface.
- Dry corrosion: also known as oxidation or high-temperature corrosion, occurs when the metal is exposed to a gaseous environment or one with negligible moisture. This is a chemical process involving the formation of a thick oxide layer in air or an oxidizing atmosphere, with the thickness of the oxide layer increasing due to solid-state diffusion through the oxide layer.

The eight main types of corrosion are as follows:

- Uniform corrosion, which affects surfaces evenly;
- Galvanic corrosion, occurring between different metals;
- Crevice corrosion, found in hidden or shielded areas;
- Pitting corrosion, which creates small holes or pits;
- Intergranular corrosion, affecting the grain boundaries of metals;
- Selective leaching, which removes specific elements from an alloy;
- Erosion corrosion, caused by rapid fluid flow;
- Stress corrosion, which happens under the influence of tensile stress.

Typically, corrosion damage manifests in two main patterns related to the surface exposed to the external environment: it can either affect the entire surface, known as generalized corrosion, or impact only a specific, limited area, termed localized corrosion.

1.8.2 Electrochemical Mechanism

Corrosion on an electrochemical mechanism where two reactions combine to constitute the total process. It is constituted of two processes: an anodic reaction or oxidation reaction which release free electrons within the metal and a cathodic reaction typically oxygen or hydrogen that consumes those electrons. The anodic reaction in every corrosion reaction is the oxidation of a metal to its ions, this can be written in the general form as:

$$M \rightarrow M^{+n} + ne$$

There are also two additional phenomena:

- An electron flow within the metal, moving from the anodic region where electrons are released to the cathodic zone where electrons are consumed. It is necessary to underline that the electrons flow direction is opposite to the convention's current direction, giving to the electrons the charge negative. Positive ions move in the same direction as the current, while negative ions move in the opposite direction.
- A current flow within the electrolyte, facilitated by ion transportation, moving from the anode to the cathode zone.

The electrochemical nature of corrosion can be illustrated by the attack on zinc by hydrochloric acid:

$$oxidation\ (anodic\ reaction)\ \ Zn \rightarrow Zn^{2+} + 2e$$

$$reduction\ (cathodic\ reaction)\ \ ZH^{+} + 2e \rightarrow H_2$$

An oxidation or anodic reaction produces an increase in valence or a production of electrons, the equation written upper are partial reactions both must occur simultaneously at the same time and the rate of oxidation equals the rate of reduction, in terms of electron production and consumption. The electrons present within the metal are immediately consumed in the reduction of hydrogen ions. In Figure 8 it is shown a zinc atom undergoes transformation into a zinc ion and releases two electrons. Is defined electrochemical any reaction that can be divided into two or more partial reactions involving oxidation and reduction.

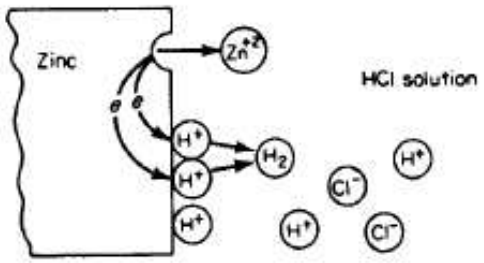

Figure 9: Electrochemical reactions occurring during corrosion of zinc in air-free hydrochloric acid. [6]

The anodic reaction in any corrosion process involves the oxidation of a metal into its ion, with the number of electrons produced equalling the ion's valence. Due to the interdependence of anodic and cathodic reactions during corrosion, it is possible to mitigate corrosion by reducing the rates of either reaction. Coating the metal surface with paint or another nonconductive film significantly reduces the rates of both anodic and cathodic reactions,

thereby slowing down corrosion. It is evident that maintaining good conductivity is crucial for both the metal and the electrolyte during the corrosion reaction. Increasing the electrical resistance of the electrolyte or corrosive can be employed as a strategy to reduce corrosion. The temperature increases the rate of almost all chemical reactions: as the temperature rises, the rate of nearly all chemical reactions accelerates, particularly in Ni-Cr-based superalloys, where the elevated temperature can significantly influence processes such as oxidation, corrosion, and phase transformations. These temperature-driven reactions can alter the microstructure and mechanical properties of the material, making thermal stability a critical factor in the performance and longevity of these high-performance alloys in demanding environments. [6]

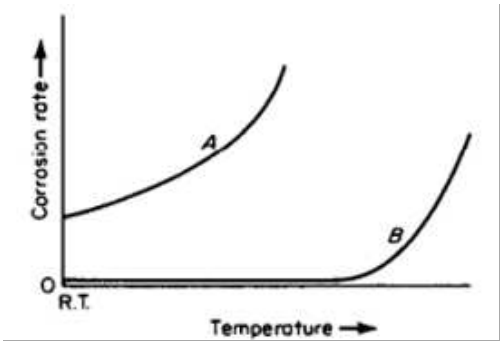

Figure 10: Effect of temperature on corrosion rate [6]

1.8.3 Thermodynamic of corrosion process

During the corrosion the value of free energy ΔG change, this is a direct measure of work capability or maximum electric energy available from the system. If the value is negative indicates a loss in free energy and also the spontaneous reaction direction of the system.

If the change in free energy is positive, this indicates the transition represents an increase in energy and this requires that additional energy be added to the system. ΔG reflects only the direction of reaction by the knowledge of its sign, but it is not possible to accurately predict the velocity of reaction. In reversible thermodynamic conditions, the energy dissipated by an infinitesimal charge transfer is given by

$$\Delta G = nFE$$

where n is the number of electrons involved in the reaction, F is the charge of one mole of electrons, and E is the cell potential. For the generic chemical reaction

$$v_a A + v_b B \leftrightharpoons v_c C + v_d D$$

the change in Gibbs free energy ΔG is:

$$\Delta G = \Delta G^0 + RTln\frac{a_{0x}^{v_{0x}}}{a_{Rid}^{v_{Rid}}}$$

Where a_i is the activity of component i and v_i is the number of moles of products or reactants. By substituting the value of G and after some manipulations, one obtains:

$$E = E^0 + RTln\frac{a_{0x}^{v_{0x}}}{a_{Rid}^{v_{Rid}}}$$

The Nernst equation, where E_0 represents the standard reaction potential, is given by the sum of the standard potentials of the reducing and oxidizing species involved in the reaction.

1.9.4 Kinetics of corrosion process

Let's consider the kinetic aspect of the reaction to gain more information about the rate at which the corrosion process occurs. In the process, there are always frictions that dissipate the available energy, known as 'overpotentials.' The magnitude of these frictions depends on the nature of the materials, the electrochemical reactions, the surface state of the materials, and the presence or absence of surface films.

During the passage of current in an electrochemical system, the electrode potentials shift from their initial equilibrium values to more positive values (for the anode) and more negative values (for the cathode). Even though the net current at equilibrium is zero, the oxidation and reduction currents are not zero. The system is typically described by the Butler-Volmer equation:

$$i = i^0(e^{-a\eta\frac{nF}{RT}} - e^{(1-a)\eta\frac{nF}{RT}})$$

where η is the activation overpotential. An η>0 indicates an anodic overpotential, while an η<indicates a cathodic overpotential. For η>50 we can assume the equation of Tafel

$$\eta = \frac{RT}{nF} = A + BlnI = blog\frac{I}{I_0}$$

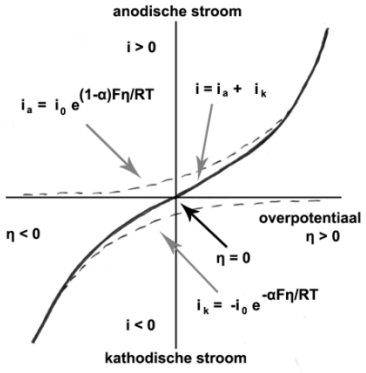

Figure 11: equation of Butler-Volmer. [4]

It is possible to simplify the equation with the Evans diagram, each reaction has its own electrode potential and exchange current density. These two potentials cannot coexist separately on the same electrically conductive surface. Instead, each must polarize or change the potential to a common intermediate value. The combination of the half-cell electrode potentials is referred to as the corrosion potential.

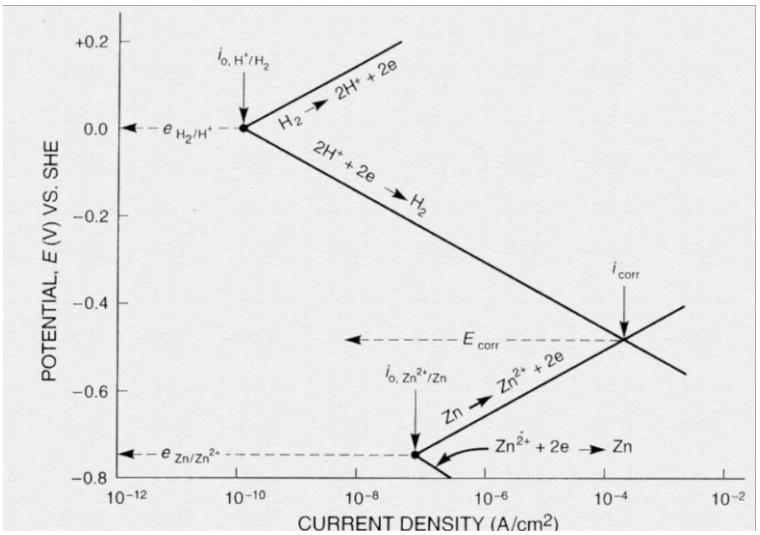

Figure 12: Example of Evans diagram.[6]

1.8.5 Passivity

The corrosion resistance of metallic materials is strongly dependent on the surface condition through the presence of oxides and corrosion products.

The formation of layers on the material surface is called passivation and when the protection property of these layers leads to a practical halt of corrosion this condition is called passivity. It involves the formation of thick layers, in order of tens micrometres, while passivity occurs when the layer is much tinner in order of nanometres. If the passivity occur the layer is called passive films. Passivation can be considered a form of anodic inhibition because the metal dissolution rate is significantly reduced by the passive film. However, passive metals are susceptible to localized breakdown of the oxide layer, which can lead to accelerated localized attack.

Figure 13: Passive layer

The behaviour of a metal alloy can be divided into three regions: active, passive and trans passive.

In the active region, E_{eq} < E < E_{pp}, the behaviour of this material id identical to that of a normal metal, it dissolves. In this range E_{pp} is primary passivation potential, which copes with the maximum anodic current i_{cp} called critical passivation current density. If more oxidizing agent is added, the corrosion rate shows a sudden decrease.

This corresponds to the beginning of the passive region. Further increases in oxidizing agents produce little, if any, change in the corrosion rate of the material. In the passivity region, E_{pp}< E < E_{tr} , metal is passive. E_{tr} is trans passivity potential or oxygen evolution potential or pitting potential, E_{pit}. The dissolution rate corresponds to passivity current density, i_p, which is very low, about 10−6 lower than i_{cp}. Finally, at very high concentrations of oxidizers or in

the presence of very powerful oxidizers, the corrosion rate again increases with increasing oxidizer power. This region is termed the trans passive region (E > E_{tr}).

In the active region the behaviour of this metal is identical to that of a normal metal slight increases the oxidizing power of a solution cause a corresponding rapid increase in the corrosion rate. If more oxidizing agent is added, the corrosion rate shows a sudden decrease.

The corresponds to the beginning of the passive region, further increases in oxidizing agent produce little, if any, change in the corrosion rate of the material. At very high concentrations of oxidizer or in the presence of very powerful oxidizers the corrosion rate again increases with increasing oxidizer power: this region is termed the trans passive region.

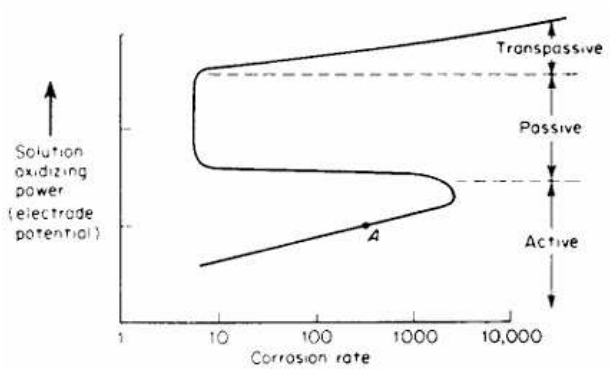

Figure 14: Corrosion characteristic of an active-passive metal as a function of solution oxidizing power (electrode potential)

The precise cause for this unusual active-passive-trans passive transition is not completely understood. It is a special case of activation polarization due to the formation of a surface film or protective barrier that is stable over a considerable range of an oxidizing power and is eventually destroyed in strong oxidizing solutions.

To summarize, metals that possess an active-passive transition become passive or very corrosion resistant in moderately to strongly oxidizing environments. Under extremely strong oxidizing conditions, these materials lose their corrosion-resistance properties. These characteristics have been successfully used to develop new methods of preventing corrosion and to predict corrosion resistance.

1.8.6 Uniform Corrosion

Uniform corrosion is one of the most common forms of corrosion, characterized by a chemical or electrochemical reaction that progresses uniformly over the entire exposed surface or a substantial portion of it, leading to metal dissolution. This type of corrosion involves a consistent rate of metal loss across the surface, causing gradual thinning of the material until failure occurs. Due to the even nature of this corrosion, the rate is often measured as the loss of metal thickness per unit of time, typically expressed as "mils per year" or "millimetres per year."

The corrosion rate can vary significantly depending on environmental factors but is generally predictable and observable when compared to more localized forms of corrosion. In uniform corrosion, both anodic and cathodic reactions occur simultaneously over the surface, leading to an even degradation pattern.[6]

Although uniform corrosion is less dangerous than localized forms, it still poses significant risks in structural applications. For example, Ni-Cr-based superalloys, commonly used in high-temperature environments such as gas turbines and jet engines, are engineered to withstand extreme conditions. However, prolonged exposure to aggressive environments, such as high-temperature oxidation or corrosive gases, can lead to uniform thinning of these materials. The addition of elements like chromium in Ni-Cr superalloys forms a protective oxide layer, slowing down the corrosion process, but the uniform loss of material can still lead to structural failure over time if not monitored properly.[21]

In certain applications, uniform corrosion may even be beneficial. For instance, in surface treatment processes, controlled corrosion is used to create rough textures on metal surfaces, which can improve material bonding or facilitate the examination of microstructures through etching.To mitigate uniform corrosion, several strategies are employed, including selecting materials resistant to corrosion, such as Ni-Cr superalloys, applying protective coatings, using corrosion inhibitors, and implementing cathodic protection measures. These approaches help extend the life of critical components in harsh environments where uniform corrosion could otherwise lead to material degradation.[20]

1.8.7 Crevice Corrosion

Crevice corrosion, also known as interstitial corrosion, is a localized form of corrosion that occurs in the presence of sub-millimeter gaps or interstices on the surface of a metal. The process is driven by the depletion of oxygen within the crevice and the inability to replenish it, leading to an oxygen-starved environment. This type of corrosion typically occurs in confined spaces where an electrolyte seeps in through capillary forces between two metal surfaces or between a metal and an insulating material. In these confined spaces, oxygen diffusion is restricted, establishing a differential aeration cell between the crevice (the microenvironment) and the exposed external surface (the bulk environment). As oxygen is consumed within the crevice, the area with low oxygen concentration acts as the anode, where metal dissolution occurs. This phenomenon is common in environments involving stagnant solutions and can be especially problematic for alloys that rely on passive oxide layers for protection, such as Ni-Cr-based superalloys used in harsh environments.

Ni-Cr superalloys, known for their high resistance to high-temperature oxidation and corrosion, can still experience crevice corrosion under certain conditions. For example, in environments with chloride ions or other aggressive species, the passive oxide layer formed by chromium can break down. This localized breakdown accelerates metal dissolution, leading to crevice formation, localized thinning, or even perforation in the material. Over time, this corrosion can compromise the integrity of components, such as turbine blades and heat exchangers, used in energy generation and aerospace applications. In some cases, the damage can propagate and lead to stress corrosion cracking, further exacerbating the risk of mechanical failure.

To initiate crevice corrosion, the gap must be wide enough for electrolyte penetration but narrow enough to maintain a stagnant zone. As the oxygen is depleted inside the crevice, the corrosion reactions become autocatalytic. Chloride ions migrate into the crevice to balance the excess positive charge, reacting with metal ions to form metal chlorides. These reactions

generate hydrochloric acid and metal hydroxides, significantly lowering the pH within the crevice and accelerating corrosion rates.

The corrosion process intensifies as the anode current density increases within the small, oxygen-starved region, while the surrounding surfaces remain relatively unaffected. This form of corrosion is particularly dangerous because it is often hidden and difficult to detect. Monitoring the extent of damage is challenging since traditional methods, such as mass loss measurements, may not accurately reflect the localized damage within the crevice.

In Ni-Cr-based superalloys, maintaining resistance to crevice corrosion involves optimizing the alloy composition to ensure a robust passive layer. However, aggressive conditions like those found in marine or high-temperature environments can still cause localized failure. Design considerations and material selection are crucial to minimize crevice corrosion risks. For instance, reducing the number of crevices or using alloys with better passive film stability can mitigate the damage.

$$oxidation\ M \rightarrow M^{+} + e$$

$$reduction\ O_2 + 2H_2O + 4e \rightarrow 4OH^{-}$$

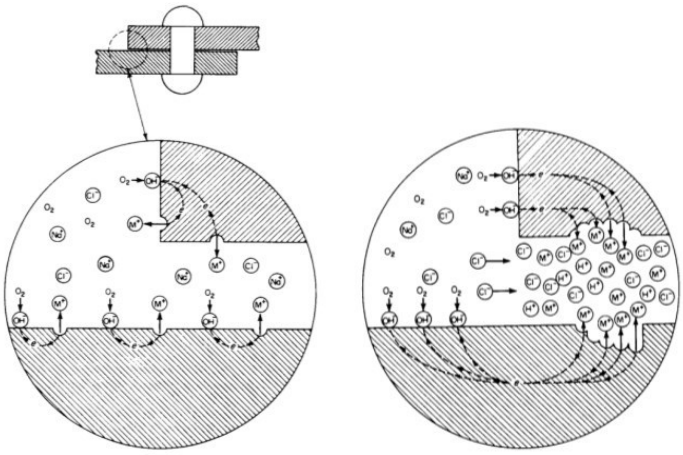

Figure 15: Crevice corrosion initial stage and later stage [6]

The corrosion process intensifies as the anode current density increases within the small, oxygen-starved region, while the surrounding surfaces remain relatively unaffected. This form of corrosion is particularly dangerous because it is often hidden and difficult to detect. Monitoring the extent of damage is challenging since traditional methods, such as mass loss measurements, may not accurately reflect the localized damage within the crevice.

In Ni-Cr-based superalloys, maintaining resistance to crevice corrosion involves optimizing the alloy composition to ensure a robust passive layer. However, aggressive conditions like those found in marine or high-temperature environments can still cause localized failure. Design considerations and material selection are crucial to minimize crevice corrosion risks. For instance, reducing the number of crevices or using alloys with better passive film stability can mitigate the damage.[2]

1.9 Electrochemical characterization technique

1.9.1 Potentiodynamic Polarization (PD)

Potentiodynamic refers to the measurement of changes in electrical potential (voltage) within a system, a key concept in electrochemistry, particularly in polarization techniques for evaluating corrosion. This method systematically varies the electrode potential over a wide range at a controlled rate by applying current through the electrolyte. Potentiodynamic polarization is fundamental in laboratory corrosion testing, offering detailed insights into corrosion mechanisms, rates, and the susceptibility of different materials to corrosion in specific environments.

The data from these tests are typically represented as polarization curves, which illustrate the relationship between current and potential. The corrosion potential, denoted as E_{corr}, reflects the potential of a corroding surface in an electrolyte relative to a reference electrode. It can be determined either from the steady-state potential when the electrode is not polarized or through Tafel extrapolation of the anodic and cathodic branches of the polarization curve. The current density at the corrosion potential, j_{corr}, is calculated from these curves and serves as an indicator of the corrosion rate. Generally, higher E_{corr} and lower j_{corr} values indicate superior corrosion resistance of the material. [25]

In Figure 16 we can see that during electrochemical passivation, if the potential of a metal sample increases in the anodic direction, its dissolution rate initially climbs, reach a peak and then decrease to a minimal level. As the potential increases further, there is minimal change in current within the passive region until the passivity threshold is exceeded, at which point a rapid rise in current occurs with increasing potential. [24]

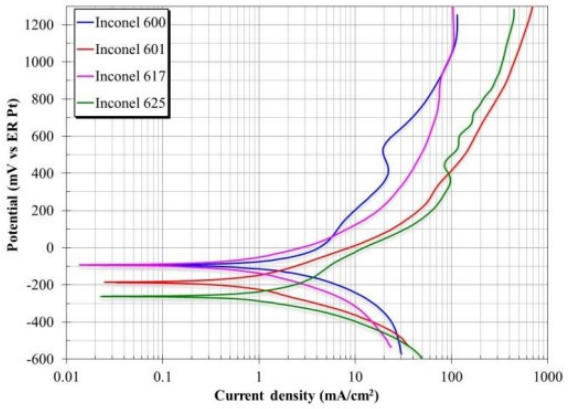

Figure 16: Potentiodynamic polarization curves of Ni-based alloys in $NaVO_3$ at 700° C in static air.[24]

The current density at the corrosion potential, j_{corr}, is derived from potentiodynamic polarization curves and is directly related to the corrosion rate. During electrochemical passivation, as the potential of a metal sample is increased in the anodic direction, the dissolution rate rises to a peak and then declines to a minimal level. Further increases in potential have little impact on the current in the passive region until passivity breaks down, at which point the current increases rapidly with potential.

Cyclic potentiodynamic polarization and Tafel extrapolation measurements follow standards outlined by ASTM, such as ASTM F2129, which is commonly used to test the susceptibility of small implants to localized corrosion.

The ASTM standard defines the zero current potential, E_{zc}, as the potential where current reaches a minimum during the forward scan. The maximum value of anodic dissolution current occurs at the primary passivation potential, E_{pp}, while the corresponding maximum anodic current is termed the critical corrosion current, j_{cc}. In the passive region, which can extend over a wide voltage range, the current density, j_{pas}, remains nearly constant, though metastable pitting may occur, evidenced by transient bursts of anodic current.

The breakdown potential, E_b, represents the lowest potential at which pitting or crevice corrosion initiates and propagates, often accompanied by oxygen evolution and passive film dissolution. A higher E_b value corresponds to greater pitting resistance. The susceptibility to crevice corrosion increases as the gap between E_b and the passivation potential (E_p) widens, causing greater hysteresis in the polarization curve. A higher E_p reflects increased resistance to crevice corrosion. [26]

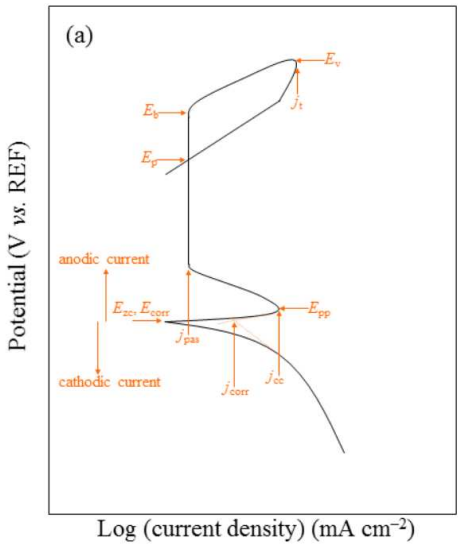

Figure 17: Schematic of cyclic PD polarization curve of a metal that exhibits a protection potential. [26]

Figure 17 shows that at potentials anodic to the primary passivation potential (E_{pp}), the current density decreases with increasing anodic potential until reaching the passive region. This region is unstable, with the current continuing to decrease over time, even at constant potential, due to the ongoing formation and growth of the passive film.

For example Figure 18 depicts potentiodynamic curves comparing the corrosion performance of wrought Inconel 625 and its thermally sprayed High-Velocity Oxy-Fuel (HVOF) coating. The x-axis of the graph represents the potential (in mV) applied during the corrosion test, while the y-axis shows the current density (in mA/cm²), which is indicative of the corrosion rate. The graph highlights the difference in corrosion behaviour between the two materials. The potential where passivation begins (where a stable passive film forms) and the corresponding corrosion current density are key pieces of information. The curve for wrought Inconel 625 shows a much lower corrosion current density in the passive region compared to the HVOF coating. This indicates that the wrought material has better corrosion resistance due to the formation of a more protective oxide layer. The HVOF coating, on the other hand, exhibits a higher current density, signalling poorer passivation and higher susceptibility to corrosion.[27]

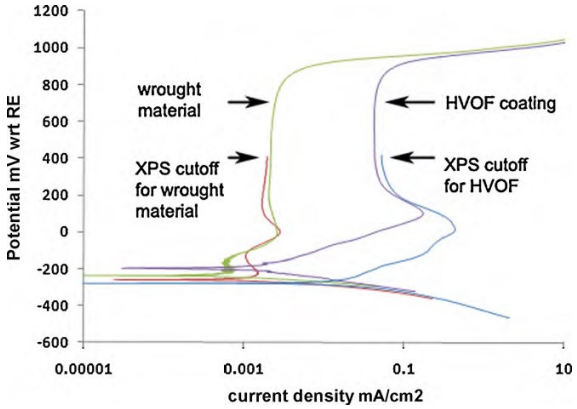

Figure 18: Potentiodynamic curves of samples showing the performance gap between wrought material and HVOF coating as well as the cut-off potentials of samples for XPS analysis. [27]

1.9.2 Mott-Schottky (MS)

The Mott-Schottky (MS) analysis is an electrochemical technique used to investigate the semiconductor properties of passive films or oxide layers on metals. It is particularly useful for determining the type of semiconductor behaviour (n-type or p-type), the donor or acceptor density, and the flat-band potential of these films. The MS analysis is based on the application of a small AC signal to the electrochemical system, while varying the applied DC potential

. The capacitance of the oxide layer (passive film) is measured as a function of the applied potential. This capacitance corresponds to the space-charge region in the semiconductor (the oxide film), which behaves similarly to a parallel-plate capacitor. For an n-type semiconductor, the relationship between the capacitance (C) and the applied potential (V) is given by the Mott-Schottky equation:

$$\frac{1}{C^2} = \frac{2}{\epsilon\epsilon_0 e N_D}(V - V_{fb} - \frac{kT}{e})$$

Where:

- C is the capacitance,
- ϵ is the dielectric constant of the semiconductor,
- ϵ_0 is the vacuum permittivity,
- e is the electron charge,
- N_D is the donor density for n-type (or acceptor density for p-type),
- V_{fb} is the flat-band potential,
- T is the temperature,
- k is Boltzmann's constant.

A plot of $\frac{1}{C^2}$ versus V gives a straight line, from which the slope provides information about the carrier density (donors or acceptors), and the intercept allows determination of the flat-band potential. A positive slope indicates n-type semiconductor behavior, while a negative slope indicates p-type behaviour. This method is widely used in corrosion studies to analyse the electronic properties of passive films on alloys and to understand the role of various alloying elements in passivation.[28]

In the context of Mott-Schottky analysis, an n-type semiconductor is a material where electrical conduction occurs primarily through electrons, which act as the majority charge carriers. This behaviour is achieved by doping the semiconductor with impurities that provide additional electrons. For n-type the analysis typically reveals that as the potential increases (in a positive direction), the capacitance decreases. This is since electrons accumulate near the surface of the semiconductor, forming a depletion region that reduces the ability of the material to store charge. An n-type material in Mott-Schottky analysis is one where electrons dominate the conduction process, and the analysis can provide insights into its doping level, capacitance behaviour, and potential defects. A p-type semiconductor is a material where electrical conduction occurs primarily through holes, which are the majority charge carriers. Holes are essentially the absence of electrons in the atomic structure, and they behave like positive charge carriers. A p-type material is created by doping the semiconductor with atoms that have fewer valence electrons than the host material creating these "holes."

In a typical Mott-Schottky plot, a straight line with a positive slope indicates an n-type semiconductor, while a straight line with a negative slope signifies a p-type semiconductor. Conversely, a U-shaped curve suggests that the behaviour of the system cannot be easily categorized as simply p-type or n-type, as observed in our case. This behaviour could be attributed to several factors:

1. Biphasic behaviour: The semiconductor may exhibit both p-type and n-type characteristics in different regions of the potential. This phenomenon can occur in complex materials or systems with double junctions, where the behaviour transitions from p-type to n-type, or vice versa, at certain points along the curve.
2. Charge accumulation and inversion: The U-shaped curve may indicate a transition between different regions of charge accumulation and inversion. For instance:
    - In the accumulation region, capacitance can increase as charge carriers (either electrons or holes) accumulate near the surface of the semiconductor.
    - In the inversion region, the behaviour of the semiconductor may shift, with a predominance of opposite charge carriers (e.g., electrons in a p-type semiconductor).
3. Presence of defects or heterogeneity: Significant defects within the material or non-uniform doping can lead to deviations from ideal behaviour, resulting in a U-shaped curve. This might suggest the existence of regions with varying concentrations of charge carriers or defects that influence the semiconductor's ability to maintain a linear response.[45]

1.10 Hardness test

The Vickers hardness test is a precise method used to measure the hardness of various materials. It is particularly valuable because it can be applied to nearly any material, from soft metals and polymers to very hard materials like ceramics. The Vickers method uses a diamond indenter in the shape of a square-based pyramid, allowing for a broad range of hardness measurements with a single tool. The test surface must be polished to eliminate any surface irregularities, which is essential for accurate indentation measurement. Materials such as metals, ceramics, and composites need to be polished to ensure that the indentation depth and size can be measured precisely. A diamond pyramid with an angle of 136° between opposite faces is used. Diamond is chosen because of its high hardness, ensuring it does not deform during the test. The indenter is pressed into the material surface with a specific force. The load can vary depending on the material and the application.To avoid rapid deformation, the load is applied gradually, held steady for a specified time , and then removed. This dwell time is crucial as it allows the indenter to stabilize fully in the material, giving a more reliable hardness measurement. After removing the load, the indenter leaves a small, square-shaped impression on the material's surface. The two diagonals of this square are measured using a high-precision microscope, typically at magnifications of around 500x or higher. The average of these diagonal lengths is then used in calculating hardness. The measurement accuracy is essential as the Vickers hardness depends directly on the size of the indentation. The Vickers test is widely applied in fields like materials engineering, metallurgy, and quality control, as it provides key information about a material's resistance to wear, deformation, and its likely performance in demanding applications. [46]

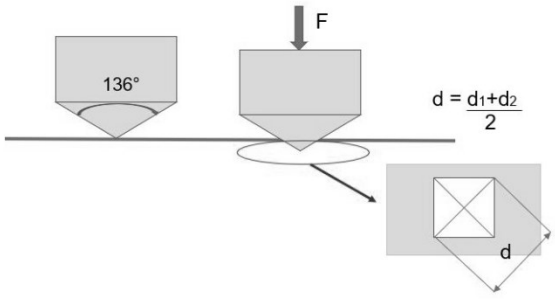

Figure 19: Vickers test

For Inconel 625, increasing the heat treatment temperature from 200°C to 500°C typically reduces the Vickers hardness (HV). This behaviour is due to a reduction in internal stresses and the potential for softening processes, like recovery and partial recrystallization, occurring within this temperature range. Heat treatments at relatively low temperatures, such as 200°C, mainly relieve internal stresses caused by prior cold working without significant changes to the material's microstructure. However, as the temperature rises toward 500°C, softening mechanisms can start to activate, particularly in a material like Inconel 625, which has a stable face-centered cubic (FCC) structure. This softening generally decreases hardness.

Inconel 625 contains alloying elements (e.g., molybdenum and niobium) that provide solid solution strengthening at room temperature. However, heat treatments up to 500°C do not usually cause precipitation hardening in Inconel 625; instead, they can lead to a slight decrease in hardness as atomic mobility increases, reducing dislocation density and altering the distribution of alloying elements.

1.11 Literature review

This section provides a summary of the key papers consulted, specifically those pertaining to the heat treatments and analysis of the passive layer on 625 alloys produced with additive manufacturing. The literature search was conducted using keywords such as "Heat Treatment", "passive layer" "LPBF", "Ni-Cr alloy " and "Inconel 625".

A comprehensive literature review on laser power bed fusion Inconel superalloys [29]

Inconel superalloys are heat-treated to improve mechanical properties at various temperatures through precipitation hardening, involving solution annealing and aging. Solution treatment creates a homogeneous, stress-free microstructure, while aging precipitates hard phases, enhancing performance. For components produced by PBF-LB (Powder Bed Fusion-Laser Beam), unique thermal post-processing is required due to different initial microstructures compared to wrought and cast forms.

Laser power influences energy transfer and scan enhance densification but may also lead to issues like porosity and increased costs. Scan speed affects build rate and energy input, with trade-offs between efficiency and potential defects. Hatch parameters, such as distance and layer strategy, impact build density and microstructure. Linear and volumetric energy densities (LED and VED) are used to evaluate the overall energy input, but their effectiveness as standalone metrics is debated.

$$LED = \frac{laser\ power}{scan\ speed}\ [\frac{J}{mm}]$$

$$VED = \frac{laser\ power}{scan\ speed\ x\ hatch\ distance\ x\ layer\ thickness}\ [\frac{J}{mm^3}]$$

Overall, understanding and optimizing these parameters is crucial for producing high-quality components, especially when working with Inconel superalloys. Solution annealing and aging can alter the grain morphology of IN625 (Inconel 625). Higher solution temperatures reduce anisotropy, strength, stiffness, and residual stresses, often linked to grain growth and the dissolution of hard precipitates.

The Laves phase dissolves above 1040°C, and the δ phase precipitates between 800-900°C, dissolving above 1000°C, which decreases hardness. HIP (Hot Isostatic Pressing) treatment improves fatigue life but reduces mechanical strength due to the dissolution of hard phases and partial recrystallization.

Standard stress-relief treatment (870°C for 1 hour) in PBF-LB IN625 promotes the formation of the δ phase more rapidly than in wrought alloys but this phase can be dissolved by homogenization at 1150°C for 1 hour.

Inconel alloys, known for their high corrosion and oxidation resistance due to passivation layers, show altered corrosion behaviour when processed by PBF-LB (Powder Bed Fusion-Laser Beam). Both as-built and heat-treated PBF-LB samples exhibit lower corrosion rates than wrought ones. However, microstructural anisotropy in as-built specimens can reduce corrosion resistance, particularly in surfaces perpendicular to the build direction, due to increased porosity and the presence of secondary phases like carbides, δ, and Laves phases. The geometry of dendrites and grains, along with surface roughness, also affects corrosion. Cr_2O_3 and Al_2O_3 passivation layers tend to form at grain boundaries, so the refined grain structure in PBF-LB components can influence corrosion resistance. Surface treatments such as peening, alloying with Ruthenium (Re), and adding TiC or Y_2O_3 nanoparticles reduce corrosion kinetics.

Solution heat treatments can decrease oxidation resistance but homogenizing the microstructure and generating γ’ and γ’’ precipitates through controlled aging improve overall corrosion resistance.

Characterization of Inconel 625 fabricated using powder-bed-based additive manufacturing technologies [30]

Experimental Procedure

The study focuses on three AM technologies EPBF, LPBF, and binder jetting each of which has distinct processing characteristics that influence the microstructure and mechanical properties of the final product. The aims are to provide a comprehensive comparison of these technologies by evaluating the mechanical performance of the Inconel 625 parts produced involves fabricating in both the X and Z orientations. After fabrication, the samples undergo hot isostatic pressing (HIP) to reduce porosity and improve mechanical properties. Mechanical testing is conducted to determine ultimate tensile strength (UTS), yield strength (YS), elongation, and modulus of elasticity (E). The microstructure is analysed using optical microscopy (OM) and scanning electron microscopy (SEM), focusing on grain structure and the presence of defects such as porosity and cracks. The results are compared against ASTM standards for Inconel 625 to evaluate the performance of each AM technology.

Results and Discussion

LPBF emerged as the most effective additive manufacturing (AM) technology for producing Inconel 625, primarily due to the fine and homogeneous microstructure it generates. The rapid cooling rates inherent to LPBF contribute to the formation of a finer grain structure compared to EPBF. This refined grain structure is a critical factor in enhancing the mechanical properties of the material, particularly its ultimate tensile strength (UTS) and yield strength (YS). The LPBF samples demonstrated the highest values for both UTS and YS, indicating superior mechanical performance. This is attributed to the process's ability to minimize defect formation, such as porosity, which is typically a challenge in AM-produced components.

The elongation at break, a measure of ductility, was also notably higher in the LPBF samples. This suggests that LPBF not only enhances strength but also preserves the material's ductility, making it suitable for applications where flexibility and toughness are crucial. The fracture analysis further supported these findings, as the LPBF samples exhibited ductile fracture characteristics, evidenced by the presence of dimpled surfaces typical of a material that deforms plastically before breaking. This ductility, combined with high strength, underscores the robustness of LPBF-fabricated Inconel 625 parts.

In conclusion, LPBF as the most promising technology for manufacturing high-quality Inconel 625 components. Its ability to produce fine, homogeneous microstructures with minimal defects directly translates into superior mechanical properties, making LPBF the preferred choice for critical applications requiring high strength and ductility in Inconel 625 parts.

Mechanical Behavior of Laser Powder Bed Fusion Processed Inconel 625 Alloy [31]

Experimental Procedure

The study focuses on understanding the mechanical behavior of Inconel 625 (IN625) alloy processed using Laser Powder Bed Fusion (LPBF), an additive manufacturing technique. The goal is to analyze the microstructural evolution and mechanical properties, such as tensile strength, fatigue, and creep resistance, at both ambient and elevated temperatures. The methods involved using LPBF to fabricate IN625 components followed by various heat treatments like stress relief (SR), solution annealing (ST), and hot isostatic pressing (HIP). Techniques like scanning electron microscopy (SEM), electron backscatter diffraction (EBSD), and X-ray computed tomography (CT) were employed to study the microstructure and mechanical properties. Tensile tests were conducted at room and elevated temperatures (up to 760°C), and fatigue, fracture toughness, and creep behaviors were analyzed

Results and Discussion

The mechanical properties of LPBF-manufactured IN625 are highly dependent on microstructure and defects introduced during processing.

LPBF IN625 exhibits anisotropy in tensile properties due to columnar dendritic growth, with the yield strength (YS) and ultimate tensile strength (UTS) ranging from 618–783 MPa and 891–1041 MPa respectively. Heat treatments improved strength but reduced ductility in some cases. For instance, HIP treatments minimized porosity but led to grain coarsening, reducing strength.

At elevated temperatures, LPBF IN625 displayed high temperature fatigue and creep resistance, with HIP-treated samples showing increased creep strength. However, fracture toughness and fatigue life were affected by the presence of pores and surface roughness, with porosity being a major factor reducing ductility and accelerating crack propagation. Creep ductility was inferior to wrought IN625, due to δ-phase segregation and higher dislocation densities.

In conclusion, while LPBF IN625 is comparable to wrought alloy in terms of strength, its creep and fatigue properties require further improvement, especially for long-term high-temperature applications.

Development and Investigation of Innovative Materials Produced by Means of Additive Manufacturing Technologies [23]

Experimental Procedure

This paper focuses on evaluating the corrosion behavior of nickel alloy 625 produced by different additive manufacturing (AM) techniques. Nickel-based alloys, particularly alloy 625, are essential in industries with harsh environments due to their excellent mechanical properties and corrosion resistance.

The experimental part of the dissertation explores three AM techniques: Laser Powder Bed Fusion (LPBF), Directed Energy Deposition (DED), and Metal Fused Filament Fabrication (MFFF). The study involves comparing the corrosion behavior of alloy 625 produced by these techniques with that of a commercially hot-rolled product. Additionally, the effect of post-process hot isostatic pressing on the corrosion behavior of MFFF and DED specimens is assessed.

Results and Discussion

The dissertation provides a comprehensive evaluation of the corrosion behavior of alloy 625 produced by advanced AM techniques, demonstrating their potential for industrial applications. The LPBF and DED-processed specimens provided very low porosity values, confirming that these technologies are currently well established and the relative process parameters are optimized. Conversely, the specimens produced by MFFF process were characterized a significant number of defects.

In the MFFF-processed material were found small pores, both preexisting in the feedstock material and generated during the deposition phase.

Moreover, periodically distributed elongated macro-defects, result of the scanning strategy adopted, were also detected. The highest hardness was provided by the samples manufactured via LPBF. The DED-processed material had a lower value, due to the coarser dendritic microstructure. Instead, the MFFF-built specimens were characterized by the lowest hardness, due to the complete disappearance of the dendritic structure.

Potentiodynamic tests in sulfuric acid showed that AM specimens are characterized by a behaviour like the traditional material, showing a wide range of passive behaviour of the material, thus confirming the excellent corrosion resistance in this environment.

Finally, cyclic potentiodynamic and potentiostatic polarization tests in chloride solution showed that the specimens obtained by LPBF and DED have a similar, if not higher, resistance to localized corrosion than traditional material.

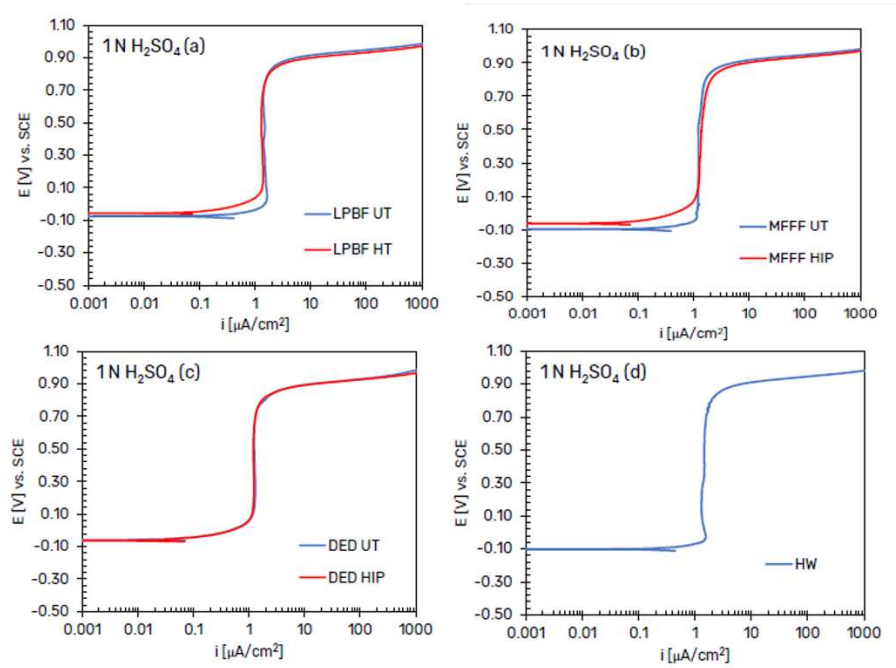

Figure 20: Potentiodynamic polarization curves 1N H_2SO_4 solution a) LPBD b) MFF c) DED-mandufactured samples and d) HW samples [23]

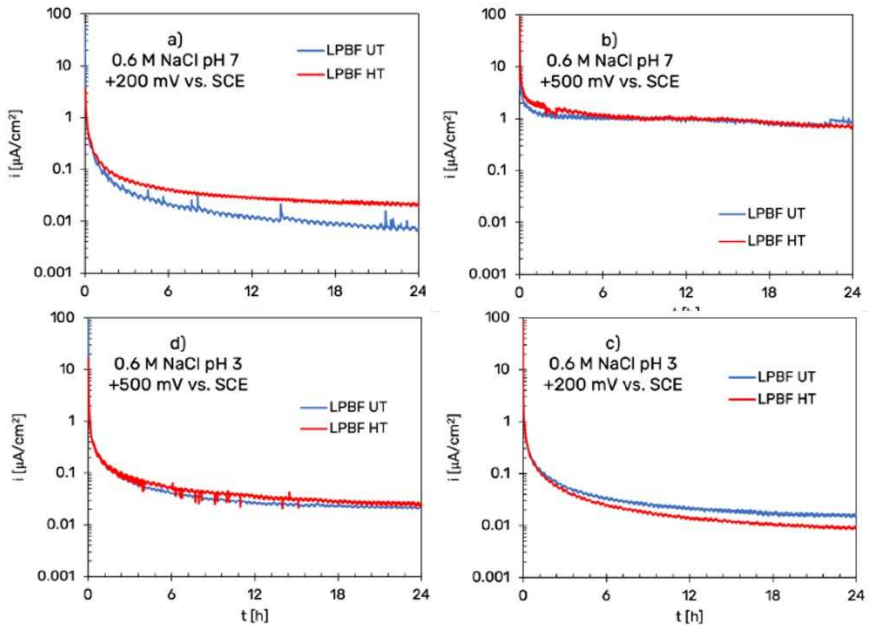

Figure 21: Current density vs. time during potentiostatic tests conducted on LPBF specimens in 0.6M NaCl at pH7 and pH3. a) at +200mV vs. SCE in 0.6M NaCl at pH7 b) at +500mV vs. Saturated Calomel Electrode(SCE) in 0.6M NaCl at pH7 c) at +200mV vs SCE in 0.6M NaCl at pH3 d) at+500 mV vs SCE in 0.6M NaCl at pH3[23]

Evaluation of Corrosion Resistance of Alloy 625 Obtained by Laser Powder Bed Fusion [32]

Experimental Procedure

The study aimed to assess the corrosion resistance of Nickel-based Alloy 625, specifically comparing samples fabricated through Laser Powder Bed Fusion (LPBF) to those produced via conventional casting and hot working methods. The primary goal was to investigate how different manufacturing processes influence the alloy's susceptibility to localized corrosion, such as pitting and crevice corrosion, which are critical factors in its performance in various industrial applications.

In this experiment, the LPBF samples were produced using a Yb-fiber laser with a power setting of 195 W, conducted in an argon atmosphere at a temperature of 80°C. To ensure a comprehensive analysis, the study included both as-built LPBF samples and those that had undergone additional polishing to achieve a 1 μm surface finish. The chemical composition of the samples was carefully controlled to match the standard composition of Alloy 625, ensuring that any differences in corrosion behavior could be attributed to the manufacturing process rather than compositional variations. The samples were then subjected to various electrochemical tests to assess their corrosion resistance. The results were compared to those of conventionally produced Alloy 625 to determine the impact of the LPBF process on corrosion performance.

Results and Discussion

The LPBF-fabricated samples, particularly those in their as-built condition, demonstrated a noticeably higher susceptibility to localized forms of corrosion, such as pitting and crevice corrosion. This increased vulnerability was primarily linked to the unique microstructural characteristics induced by the LPBF process. Key factors contributing to this behavior included the presence of high residual stresses, porosity, and the microsegregation of alloying elements, which are intrinsic to the rapid solidification and layer-by-layer deposition inherent in the LPBF technique.

The study further explored the impact of post-processing on the corrosion resistance of LPBF samples. When the LPBF specimens were polished to a 1 μm surface finish, there was a marked improvement in their corrosion resistance. This improvement was attributed to the reduction of surface roughness and the removal of some of the surface defects that are characteristic of the as-built LPBF samples. However, despite these enhancements, the polished LPBF samples still did not reach the same level of corrosion resistance observed in the conventionally produced Alloy 625. The study suggested that the microstructural anomalies introduced during the LPBF process, such as incomplete densification and retained stress, persist even after polishing and significantly influence the material's overall corrosion behavior.

Electrochemical tests, including potentiodynamic polarization, revealed that the corrosion potential of LPBF samples was lower compared to that of conventionally produced samples, indicating a greater tendency towards corrosion initiation. Moreover, the LPBF samples exhibited a higher pitting current density, reinforcing the observation that these samples are more prone to localized corrosion. These results underscore the complexity of the LPBF process and its effects on the microstructure and, consequently, the corrosion performance of Alloy 625.

The study's findings emphasize the necessity for further optimization of the LPBF process parameters and the development of effective post-processing techniques to mitigate the microstructural defects that compromise the corrosion performance of additively manufactured alloys.

Effect of heat treatment on the anisotropic mechanical properties and corrosion resistance of laser powder bed fusion fabricated Inconel 625 [33]

Experimental Procedure

This study focuses on understanding the effects of heat treatment on the anisotropic mechanical properties and corrosion resistance of Inconel 625, a nickel-based superalloy, fabricated using (LPBF).

The primary aim of this study was to investigate how different heat treatment processes namely aging at 650°C, sensitization at 850°C, and homogenization at 1050°C impact the microstructure, mechanical properties, and corrosion resistance of LPBF-fabricated Inconel 625. The focus was on the evolution of microstructures, particularly at grain boundaries and within cellular structures, and how these changes affect the alloy's overall performance in terms of strength and resistance to corrosive environments.

To carry out the experiment, commercially available gas-atomized Inconel 625 powder, with particle sizes ranging from 15 to 53 μm, was used. The specimens were produced using a HBD-80 LPBF printing machine. The process parameters were meticulously optimized to ensure high-density fabrication: a laser power of 175 W, a scan speed of 800 mm/s, a hatching space of 0.11 mm, and a layer thickness of 0.02 mm. A bidirectional meander scanning strategy with a 67° rotation angle between layers was employed to enhance the mechanical properties and minimize defects.

After fabrication, the samples were subjected to three distinct heat treatments to assess the effects of aging, sensitization, and homogenization on the material's properties. Each heat treatment was conducted in a muffle furnace under air atmosphere, held for 1 hour at the specified temperature. The microstructure of the samples post-heat treatment was thoroughly characterized using various advanced microscopy techniques. These techniques were used to observe changes in grain boundaries, cellular structures, and the presence of phase precipitations, which are critical to understanding the material's behavior.

Additionally, the mechanical properties of the heat-treated specimens were evaluated through tensile tests conducted on dog-bone-shaped samples oriented in different directions to study anisotropy. Corrosion resistance was assessed using boiling ferric sulfate/sulfuric acid tests, following ASTM G28 standards. The comprehensive analysis provided insights into how heat treatments influence the relationship between microstructure evolution, anisotropic mechanical properties, and corrosion resistance of LPBF-fabricated Inconel 625.

Results and Discussion

The aging process at 650°C led to the precipitation of fine γ" (Ni_3Nb) and δ phases within the grain boundaries and cellular structures, which enhanced the alloy's tensile strength but introduced some brittleness due to the hard phases. Sensitization at 850°C caused a more significant precipitation of the δ phase and the formation of continuous carbide ($M_{23}C_6$) networks along grain boundaries. This phase evolution compromised the alloy's ductility and made it more susceptible to intergranular corrosion. In contrast, homogenization at 1050°C effectively dissolved secondary phases and homogenized the microstructure, reducing the anisotropy introduced by the LPBF process. The homogenized microstructure exhibited more equiaxed grains, with a notable reduction in residual stresses and defects. In terms of mechanical properties, the aging treatment enhanced the tensile strength due to the precipitation of the γ" phase but resulted in a decrease in ductility. Sensitization negatively impacted both strength and ductility, primarily due to the brittle carbide networks formed during the treatment. Homogenization improved the ductility and uniformity of mechanical properties across different orientations, effectively reducing the anisotropy observed in the as-built condition.

Regarding corrosion resistance, the as-built samples initially showed good resistance to corrosion. However, this resistance was slightly compromised by the aging and sensitization treatments, which introduced more phases prone to corrosive attack. Sensitized samples displayed the poorest corrosion resistance, particularly due to the formation of chromium-depleted zones along grain boundaries, making them vulnerable to intergranular corrosion. On the other hand, homogenization improved corrosion resistance by eliminating harmful phases and restoring the uniformity of the alloy's chemical composition, thereby reducing susceptibility to localized corrosion.

The study demonstrated that heat treatments significantly influence the microstructure, mechanical properties, and corrosion resistance of LPBF-fabricated Inconel 625. While aging can enhance strength, it may reduce ductility, and sensitization can lead to both mechanical and corrosion vulnerabilities. Homogenization, however, proved to be the most beneficial treatment, as it enhanced both mechanical uniformity and corrosion resistance, making it a valuable process for optimizing the performance of LPBF Inconel 625 in demanding environments.

Effect of heat treatment on microstructure and oxidation properties of Inconel 625 processed by LPBF [34]

Experimental Procedure

The study investigates the microstructure evolution and oxidation behavior of Inconel 625 (IN625), a nickel-based superalloy, produced via Laser Powder Bed Fusion (LPBF). The unique microstructure resulting from the LPBF process, which includes fine dendritic structures and anisotropic grain orientations, requires thorough examination, especially regarding its behavior under oxidative conditions at elevated temperatures. The primary objective of the experiment was to assess the oxidation resistance of LPBF-produced IN625 in both its as-built (AB) and solution-treated (SOL) states when exposed to thermal conditions. This evaluation was carried out by subjecting the samples to oxidation at 900°C for up to 96 hours, followed by comprehensive analysis using advanced characterization techniques.

The IN625 powder utilized in the experiment was procured from EOS GmbH, ensuring compatibility with LPBF processing. The samples were fabricated using an EOSINT M270 machine, operating under precise conditions: a laser power of 195 W, a scan speed of 1200 mm/s, a hatching distance of 0.09 mm, and a layer thickness of 20 μm. A 67° rotation between successive layers was applied in the scanning strategy to enhance the density of the fabricated specimens.

Two distinct sets of samples were prepared for the study. One set was retained in its as-built (AB) condition, while the other set underwent solution annealing at 1150°C for 2 hours, followed by water quenching, aimed at eliminating segregations and secondary phases. These samples were then polished and exposed to oxidation treatments at 900°C for varying durations (8, 24, 48, 72, and 96 hours) to study the effects over time.

For post-oxidation characterization, several techniques were employed. Scanning Electron Microscopy (SEM) and Energy-Dispersive X-ray Spectroscopy (EDS) were used to analyze the cross-sections of the oxidized samples, focusing on the morphology and elemental composition of the oxide layers. X-ray Diffraction (XRD) was conducted to identify the phases present in both AB and SOL samples before and after oxidation, providing insights into phase evolution. Additionally, scratch tests were performed to assess the adhesion and mechanical integrity of the oxide layers formed during the oxidation process.

Results and Discussion

The oxidation behavior of the AB and SOL samples was significantly different. The AB samples demonstrated superior oxidation resistance, as indicated by a lower mass gain and a more uniform oxide layer formation compared to the SOL samples. After 48 hours of oxidation, the SOL samples exhibited a notable increase in oxide layer thickness and the presence of defects, leading to a higher oxidation rate. These observations were supported by SEM and XRD analyses, which revealed differences in the microstructure evolution between the two conditions. The scratch tests further confirmed the superior mechanical stability of the oxide layer in the AB samples.

The study concludes that the as-built LPBF IN625 possesses better oxidation resistance than its solution-treated counterpart, making it more suitable for high-temperature applications without additional heat treatments. The findings highlight the importance of understanding the microstructural effects of LPBF processing on the high-temperature performance of nickel-based superalloys.

Effects of temperature on the protective property, structure and composition of the oxide film on Alloy 625 [35]

Experimental Procedure

The study aims to investigate the effects of temperature on the protective properties, structure, and composition of the oxide film formed on Alloy 625 in a lithium borate buffer solution (pH300°C = 6.93) over a temperature range of 25°C to 300°C. Electrochemical methods, including potentiodynamic polarization and electrochemical impedance spectroscopy (EIS), were used alongside X-ray photoelectron spectroscopy (XPS) for compositional analysis.

A flow-through electrochemical cell with three electrodes was utilized, and the system was heated with band heaters. The alloy's surface was prepared with emery paper, and electrochemical measurements were taken under controlled pressure (14 MPa) and temperatures ranging from 25°C to 300°C. The oxide film was analyzed for its composition after exposing the samples to different temperatures.

Results and Discussion

The results showed that increasing temperature degraded the protective properties of the oxide film. At 25°C and 150°C, the oxide film was composed of Cr_2O_3 and $Cr(OH)_3$, forming a single protective layer. However, at 250°C and 300°C, the film transformed into a double-layer structure with $Ni(OH)_2$ present in the outer layer alongside $Cr(OH)_3$, while Cr_2O_3 remained in the inner layer. Electrochemical impedance spectroscopy confirmed the change in structure from a single to a double layer as temperature increased.

The conclusions highlight that the film's protective properties decrease as temperature rises due to compositional changes in the barrier layer. This degradation is attributed to the increased presence of $Ni(OH)_2$ in the outer layer, which reduces the film's overall corrosion resistance.

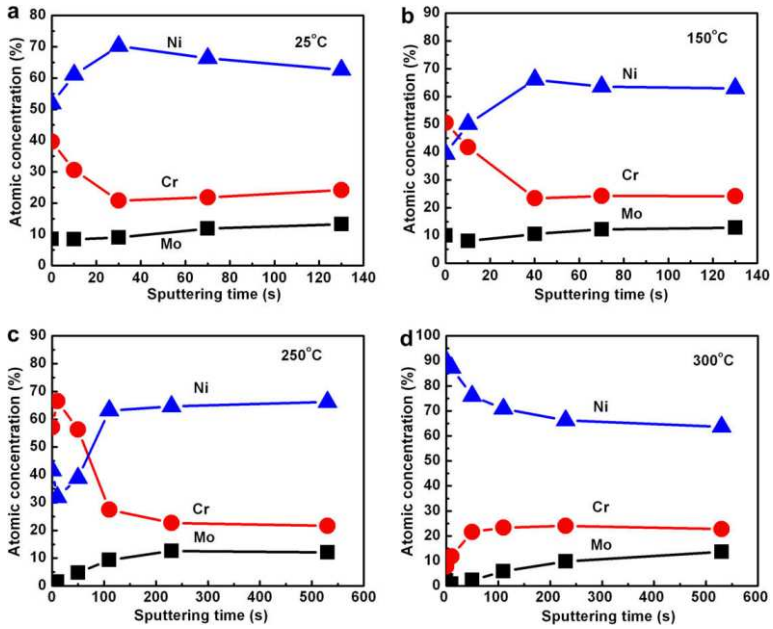

Figure 22:. The depth profiles of the alloy elements in Alloy 625 after oxidation for 30 min at 0 V (vs. Standard Hydrogen Electrode SHE) in pH300C = 6.93 solution in the temperature range of 25–300 C at 14 MPa.

Role of Elemental Segregation on the Oxidation Behavior of Additively Manufactured Alloy 625 [36]

Experimental Procedure

The study focuses on the oxidation behavior of Alloy 625, a nickel-based superalloy, manufactured through both additive manufacturing (AM) techniques—laser powder bed fusion (LPBF) and direct energy deposition (DED)—as well as conventional wrought methods. The objective is to investigate how elemental segregation, particularly of niobium (Nb) and molybdenum (Mo), affects the oxidation process at high temperatures (800°C) in air.

Materials used for the study included gas-atomized Alloy 625 powder, which was used in both AM processes. For the LPBF samples, an EOSINT M 280 system was employed, while for DED samples, a custom-built system featuring a Trumpf TruDisk6002 laser and an ABB robotic arm was utilized. In contrast, the wrought Alloy 625 served as a reference sample. The microstructures of these samples were characterized using field-emission scanning electron microscopy (SEM) and electron probe microanalysis (EPMA) to assess the distribution of refractory metals, particularly Nb and Mo, in the interdendritic regions of AM samples. Oxidation tests were conducted using a thermogravimetric analyzer (TGA) to measure mass gain at 800°C over 24 hours.

Results and Discussion

The study concludes that elemental segregation significantly affects the oxidation behavior of additively manufactured Alloy 625. The AM samples, particularly those produced by DED, exhibited higher segregation of Nb and Mo in comparison to the wrought alloy, leading to differences in microstructure and oxidation resistance. DED samples demonstrated the highest segregation and consequently formed more discontinuous d-phase precipitates beneath the chromia (Cr_2O_3) scale, which affected the overall stability of the oxide layer. The wrought samples displayed better oxidation resistance due to their more homogeneous microstructure, with LPBF samples showing intermediate behavior. Oxidation kinetics revealed that AM samples, especially DED, experienced higher mass gain and thicker oxide scales compared to wrought samples, which adhered more uniformly. The d-phase precipitation, promoted by Nb segregation, did not significantly affect Cr consumption but contributed to scale decohesion in AM samples. Overall, the wrought Alloy 625 displayed superior oxidation performance, while the LPBF samples outperformed DED in terms of oxidation resistance.

X-ray photoelectron spectroscopy study of the passive films formed on thermally sprayed and wrought Inconel 625 [27]

Experimental Procedure

The study focuses on analyzing the corrosion resistance of thermally sprayed coatings of Inconel 625 alloy compared to wrought Inconel 625. Inconel 625 is a nickel-based alloy known for its corrosion resistance, used in environments such as nuclear and thermal energy applications. The research aims to investigate the performance gap in corrosion resistance between thermally sprayed coatings and bulk materials. This difference is primarily due to the unique microstructure of the coatings, which are formed from partially or fully melted particles that result in interconnected porosity and regions depleted in oxide-forming elements.

The experimental process involves the preparation of samples of both thermally sprayed and wrought Inconel 625, with the thermally sprayed coatings deposited using a high-velocity oxy-fuel (HVOF) process. Potentiodynamic polarization tests in 0.5M sulfuric acid were performed to examine corrosion behaviour. X-ray photoelectron spectroscopy (XPS) was used to analyze the passive films formed on the samples, comparing air-formed films and those formed after polarization.

Results and Discussion

The results revealed that both the thermally sprayed coatings and wrought Inconel 625 form passive films containing oxides of nickel, chromium, molybdenum, and niobium. However, the thermally sprayed coatings showed significantly poorer corrosion resistance, attributed to the formation of non-protective $Ni(OH)_2$ in the local regions. In contrast, the passive films on wrought Inconel 625 contained more stable oxides, such as Cr_2O_3, MoO_3, and Nb_2O_5, which provide better corrosion resistance.

In conclusion, the performance gap between the thermally sprayed and wrought materials is due to the presence of local Ni-rich, Cr-depleted regions in the coatings, which lead to the formation of loose $Ni(OH)_2$ that compromises the passive film's protective properties. The study suggests that improving the composition uniformity of thermally sprayed coatings could enhance their corrosion resistance, aligning them closer to that of the wrought material

Studies on the Oxidation Behavior of Inconel 625 Between 873 and 1523 K [37]

Experimental Procedure

The study focuses on understanding the oxidation behavior of Inconel 625, a nickel-based superalloy, in the temperature range of 873 to 1523 K. The goal is to examine how the alloy's oxidation mechanism changes with temperature. The material used is a 1mm thick sheet of Inconel 625, cut into samples of 10mm x 10mm dimensions, which were electropolished for the experiment.

The main experimental technique employed was thermogravimetric analysis (TGA) to measure the oxidation at two oxygen pressures (0.12 kPa and 101.3 kPa) across various temperatures. Additional surface analysis methods like X-ray photoelectron spectroscopy (XPS), Auger electron spectroscopy (AES), and energy dispersive X-ray spectroscopy (EDS) were used to examine the surface composition of the formed oxide layers. These techniques aimed to study how the oxidation kinetics and surface oxide films evolve, particularly the role of chromium, titanium, and niobium oxides at higher temperatures.

Results and Discussion

The study found that the oxidation behavior of Inconel 625 follows a parabolic trend at temperatures between 1323 K and 1523 K, indicating a diffusion-controlled process. Significant findings included the observation that the oxidation mechanism is temperature-dependent. At temperatures above 873 K, the oxide layer becomes enriched with chromium oxide (Cr_2O_3), peaking at around 1200 K. At higher temperatures (>1300 K), the oxides of niobium and titanium are also formed in significant amounts.

The study concluded that the oxidation kinetics are nearly independent of oxygen pressure. The presence of niobium in the oxide layer at high temperatures significantly reduces the oxidation rate, contributing to the long-term stability of Inconel 625. The Cr_2O_3 layer plays a major role in controlling the oxidation process, with the diffusion of cations through this layer being the rate-determining step.

A Comparative Analysis Between Material Extrusion and Other Additive Manufacturing Techniques: Defects, Microstructure and Corrosion Behavior in Nickel Alloy 625 [40]

Experimental Procedure

The study examined the defects, microstructure, hardness, and corrosion behavior of Nickel Alloy 625 specimens produced using different additive manufacturing techniques: Powder Bed Fusion-Laser Beam (PBF-LB), Directed Energy Deposition-Laser Beam (DED-LB), and Material Extrusion (MEX).

Results and Discussion

In terms of defects, PBF-LB and DED-LB specimens showed very low porosity.
Regarding microstructure, PBF-LB and DED-LB specimens displayed microstructures consistent with existing literature. MEX specimens, however, showed equiaxed grains with Mo-, Nb-, and Si-rich second phases, which had a blocky morphology in the core and an elongated shape in the contour.
In terms of hardness, PBF-LB specimens exhibited the highest hardness due to small dendritic regions. DED-LB specimens had slightly lower hardness due to coarser dendritic structures. MEX specimens showed the lowest hardness, attributable to the absence of dendritic structures, resulting in a Vickers microhardness of 189 ± 11 HV.
For corrosion behavior, PBF-LB and DED-LB specimens provided excellent corrosion resistance, with DED-LB showing a corrosion rate of less than 100 mdd (100 μm). In contrast, MEX specimens exhibited the highest corrosion rate among the additive manufacturing technologies considered, although still significantly lower than the hot-worked (HW) benchmark material. The increased corrosion rate in MEX specimens was primarily due to localized attacks in the core region influenced by microstructural features.
The experimental methods involved fabricating the specimens using the three different techniques and employing metallographic investigations such as microCT analysis and X-ray diffraction (XRD) to study the defects and microstructures. Corrosion testing was conducted using intergranular corrosion tests to evaluate the corrosion rates of the different AM-processed specimens, comparing these with a hot-worked (HW) benchmark material.
In conclusion, the study highlights significant differences in defectology, microstructure, hardness, and corrosion behavior among Nickel Alloy 625 specimens produced using different additive manufacturing techniques. The MEX process was noted for higher defect rates and lower material hardness, as well as poorer corrosion resistance compared to PBF-LB and DED-LB methods. These findings underscore the importance of selecting appropriate additive manufacturing techniques based on the specific application requirements of Nickel Alloy 625.

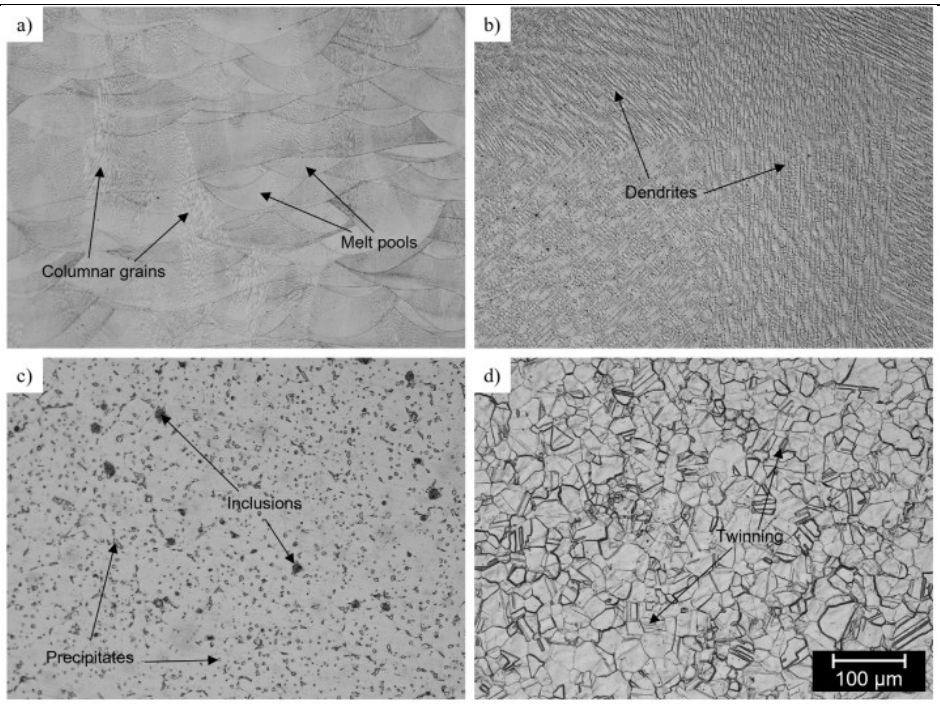

Figure 23: Optical micrographs of the PBF-LB (a), DED-LB (b), MEX-processed (c) and HW (d) specimens.

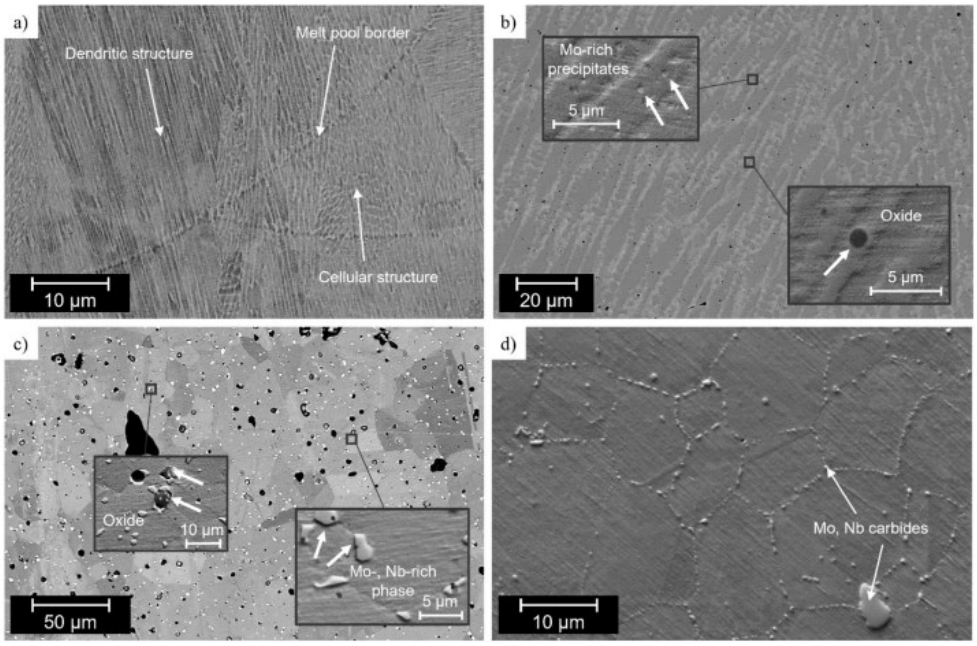

Figure 24: SEM micrographs of the PBF-LB (a), DED-LB (b), MEX-processed (c) and HW (D) specimens.

2. Experimental procedure

The aim of this thesis is to investigate the effect of heat treatments on microstructural and oxide layers of additive manufactured Inconel 625.

2.1 Material production

The samples involved is Inconel 625 alloy produced used Laser Powder Bed Fusion (LPBF) additive manufacturing technique and samples produced by conventional method. Five main samples were utilized, as previously mentioned in Chapter 1.6 they are:

- Conventional
- Nopat40
- Nopat180
- Chess
- Stripes

The LPBF samples have a layer thickness of 40 μm which has allowed us to obtain an excellent production quality of the samples at the expense of longer production times.

	Ni	Cr	Fe	C(1)	Mn	Si	Co	Al	Ti	P	S	Mo	Nb+Ta
min	58	21										8	3.2
max	71	23	5	0.03	0.5	0.4	1	0.4	0.4	0.01	0.01	10	3.8

(1) The chemical analysis may differ slightly in some elements in other specifications and contain additional elements: according to DIN EN 10095

Table 3: Chemical composition (wt.%)

Additional information about the laser power and production specifics was withheld due to company confidentiality.

2.2 Sample preparation

The samples were subjected to grinding on an ATA SAPHIR 320 grinding machine, utilizing abrasive discs with grit sizes of 500, 800, 1000 and 1200. Continuous water flow was applied to the discs to reduce friction and avoid overheating, which could otherwise affect the material's surface properties.

The polishing process was carried out on a STRUERS LaboPol-21 machine, removing all surface scratches to make the material's defects observable under a microscope. During polishing, diamond particles suspended in alcoholic solutions were applied to rotating cloths. Three different particle sizes 6 μm, 3 μm, and 1 μm were used on the first, second, and third cloths, respectively.

To avoid cross-contamination between different cloths, samples were thoroughly rinsed with water and ethanol before moving to the next polishing stage. Additionally, water was intermittently sprayed during polishing to further reduce friction.

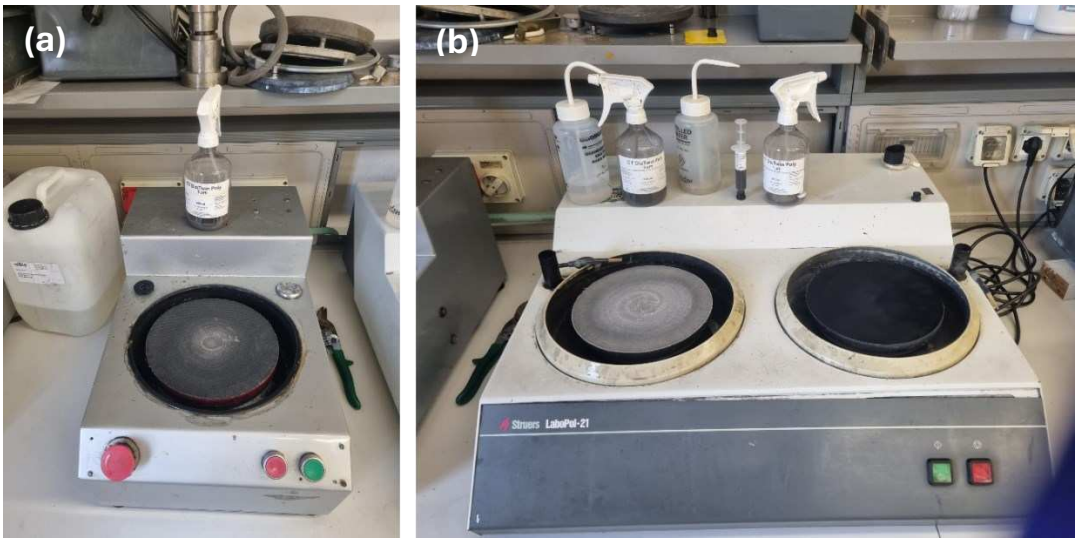

Figure 25: polishing machines (a) for 6 µm and (b) for 3 µm and 1 µm.

Four sample sets consisting of 1 conventional sample and 4 LPBF, with different scanning strategies (Nopat40, Nopat180, Chess and Stripes) of Inconel 625 were placed in a furnace for 1 hour, with four samples exposed to each of four distinct temperatures: 200°C, 300°C, 400°C, and 500°C. After heating, the samples were air-cooled to room temperature.

Immediately after the heat treatment, several tests were performed to analyze the passive layer, followed by grinding and polishing of the samples, using the same procedure described in section 2.2. Below a summary Table 4 to better explain the set of samples available:

	Conventional	Nopat40 LPBF	Nopat180 LPBF	Stripes LPBF	Chess LPBF
As Received (AR) (No heat treatment)	1 sample	1 sample	1 sample	1 sample	1 sample
200°C (HT200)	1 sample	1 sample	1 sample	1 sample	1 sample
300°C (HT300)	1 sample	1 sample	1 sample	1 sample	1 sample
400°C (HT400)	1 sample	1 sample	1 sample	1 sample	1 sample
500°C (HT500)	1 sample	1 sample	1 sample	1 sample	1 sample

Table 4: Summary of all the samples.

2.3 Analysis of microstructure

2.3.1 Preparation

All the samples with a mirror finish (1 µm) including both as-received and solution-annealed samples) were cleaned for 1 minute in an ultrasonic bath filled with a solution of 70% ethanol and 30% distilled water. The ultrasonic cleaning effectively removed any residual polishing particles or contaminants it generates high-frequency vibrations that create cavitation bubbles in the solution, which agitate the surface of the samples and dislodge contaminants. This method is widely used in various fields for its thorough and uniform cleaning capabilities.[38] After cleaning, the samples were dried using compressed air.

2.3.2 Etching

Adhesive tape was applied to each sample to cover part of its surface. An acid solution known as Kalling N.2, which is suitable for Inconel 625 alloy, was then applied to the exposed section of each sample and left to act for approximately 1 minutes.

Kalling's Reagent is used for metallographic etching to reveal the microstructure of Inconel 625, a nickel-chromium alloy. The solution typically comprises a mixture of hydrochloric acid, nitric acid, and water. This etching solution selectively attacks the grain boundaries and phase boundaries within the alloy, making them visible under an optical microscope. By using Kalling's reagent, researchers can effectively highlight and analyze the microstructural features of Inconel 625, such as grain size and phase distribution. [39] The composition is 5g of CuCl, 100 mL of Hydrochloric acid and 100mL of Ethanol.

Finally, the sample was rinsed with ethanol and dried with compressed air. The etching process exposes the microstructure of the surface by selectively corroding the grain boundaries, making the metal grains visible under the microscope.

2.3.3 Optical microscope and Scanning Electron Microscope

The etched surfaces of the samples were inspected with a LEICA DM RE optical microscope, utilizing magnifications of 5x, 10x, and 20x, and observed in black and white mode. For each magnification level, five images were captured, except at 20x magnification, where ten images were taken. Subsequently, the samples were analysed using a Scanning Electron Microscope (SEM) with the following settings: ETH 15, WD 8mm, and I PROBE 16.

The tungsten-based Scanning Electron Microscope (SEM) operates by using a tungsten filament as the electron source. When heated, this filament emits a stream of electrons that are accelerated and focused into a fine beam. This electron beam is directed onto the surface of a sample, where it scans in a raster pattern, line by line, across the area of interest. As the electrons interact with the sample's atoms, they generate various types of signals, including secondary electrons, backscattered electrons, and X-rays. These signals provide information about the sample's topography, composition, and other characteristics. Secondary electrons, for example, are particularly useful for producing high-resolution images of the surface structure, while backscattered electrons help reveal differences in atomic number, allowing for material contrast.

2.4 Oxide layer study

In order to study the oxide layer, electrochemical tests were performed using a GAMRY potentiostat/galvanostat (see Figure 28

All electrochemical tests (PD, MS) were managed through the GAMRY Framework software, which controlled the potentiostat via a computer. The GAMRY ECHEM Analysis program was used to display the resulting curves on-screen, facilitating an initial qualitative assessment of the data.

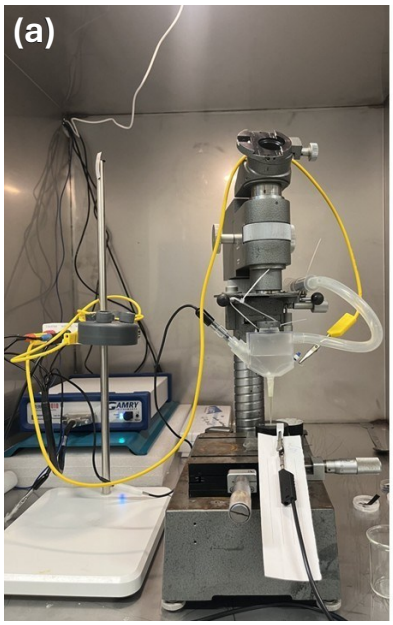

Figure 26: GAMRY Potentiostat/Galvanostat. (a) Microcapillary.

2.4.1 Borate Buffer solution

The experiments were carried out at room temperature (22 ± 2°C) under controlled conditions, with a pH of 9.2, using a Borate Buffer solution composed of 0.0075M sodium tetraborate decahydrate ($Na_2B_4O_7$ - $10H_2O$) and 0.05M boric acid (H_3BO_3). This specific buffer solution was chosen due to its stability in maintaining an alkaline pH, which is crucial for replicating the typical environments where corrosion resistance of nickel-based alloys, such as Inconel 625, is tested. The buffer serves to minimize fluctuations in pH that could otherwise affect the accuracy of electrochemical measurements. For each new sample tested, the buffer solution was replaced to ensure the consistency and reliability of the results, particularly in the case of immersion cell experiments. Replacing the solution prevented contamination or dilution that might arise from repeated use, which could alter the electrochemical behaviour of the sample. This protocol was especially important for evaluating the passive oxide layer formation and stability, as any residual products from previous tests could influence subsequent measurements. By maintaining the same controlled environmental conditions and regularly renewing the solution, the study ensured reproducibility and provided a more accurate assessment of the material's electrochemical properties in alkaline conditions.

Potentiodynamic polarization (PD) was performed over 20 minutes, during which the electrode potential was varied automatically from -1000 mV to +1500 mV with respect to the reference electrode, at a scan rate of 5 mV/s. The conditioning time for these tests was set at 600 seconds, both at 0 mV, 300 mV, and 600 mV as well as with the conditioning feature turned off.

Mott-Schottky (MS) analysis was carried out for 15 minutes, during which the electrode potential was varied from -1000 mV to +1000 mV, using an AC voltage of 10 mV and a frequency of 1000 Hz. The experiment included a conditioning time of 600 seconds at both 0 mV, 300 mV, and 600 mV. A Reverse Mott-Schottky (MS-Rev) analysis was also conducted

under the same conditions, with the key difference being that the electrode potential was varied in the opposite direction, from +1000 mV to -1000 mV.

After these experiments, the samples were polished up to 1 µm using the same procedure described previously in Chapter 2.2, to study the passive layer of these samples, each sample was left for at least 24 hours to allow the passive layer to reform.

Potentiodynamic polarization (PD) was repeated on the samples, during which the electrode potential was automatically varied from -1000 mV to +1500 mV with respect to the reference electrode, at a scan rate of 5 mV/s. The conditioning time for these tests was set at 600 seconds at 0 mV and 300 mV as well as with the conditioning feature turned off. Mott-Schottky (MS) analysis was carried out for 15 minutes, during which the electrode potential was varied from -750 mV to +900 mV, using an AC voltage of 10 mV and a frequency of 1000 Hz. The experiment included a conditioning time of 600 seconds at 0 mV and 300 mV. A Reverse Mott-Schottky (MS-Rev) analysis was also conducted under the same conditions, with the key difference being that the electrode potential was varied in the opposite direction, from +900 mV to -750 mV.

2.4.2 Data processing

In summary, the samples were first polished to a surface finish of 1 µm and then subjected to heat treatment. Immediately afterward, the passive layer was analysed using PD, MS. The samples were then polished again to a 1 µm finish, and the passive layer study was repeated.

The corrosion test results were recorded using the GAMRY framework software and saved as text files (.DTA), each file named according to the corresponding experiment. An initial review of the data was performed using the GAMRY ECHEM Analysis software. The text files were then imported into Microsoft Excel through a step-by-step process that converted them into editable tables.

After normalization, the data tables were imported into Origin Lab software, where they were organized into different books based on the test type. Each sheet within the books was dedicated to the results of a specific experiment. Using this structured data, graphs were created to visually represent and compare the experimental outcomes, enabling a clearer understanding of the corrosion behaviour across different tests.

2.4.3 Data processing for hardness test

For the hardness test Inconel 625 samples were polished to remove surface irregularities and ensure accurate indentation measurements. Polishing is particularly crucial for Vickers tests on superalloys since surface roughness can affect indentation size and the precision of hardness values.

A diamond indenter in the shape of a square-based pyramid with a 136° angle between opposite faces is used. In the Vickers test, load application can vary but commonly ranges between 1 N and 30 N for metals like Inconel 625, though microhardness testing might use lower loads to evaluate hardness on specific microstructures. In this case we use a force of 2.01 N.

The load is applied gradually over a time frame (often around 10-15 seconds for Inconel 625) to avoid rapid deformation that could skew results. After reaching the desired load, it's maintained for a few seconds to allow the indenter to fully penetrate and stabilize in the material. After load removal, the indenter leaves a square-shaped impression on the alloy's surface. The lengths of the diagonals of this impression are measured under a microscope, typically at magnifications around 500x or higher for precision. Measurements must be highly accurate to ensure a valid hardness calculation. Vickers hardness is calculated by dividing the applied force by the surface area of the indentation. The formula used is:

$$HV = 0.1891 \frac{F}{d^2}$$

where:

- HV is the Vickers hardness value.
- F is the applied force in N.
- d is the mean diagonal length of the indentation in millimetres.

Subsequently, all the measurements were reported in an Excel file to be able to compare them.

3. Result and Discussion

3.1 Microstructure analysis

3.1.1 Optical Microscope

Optical microscope analysis showed clearly the build direction in LPBF for the different types of samples: elongated structures follow a preferred orientation, likely corresponding to the solidification direction during the LPBF process, typical of laser melting where solidification occurs parallel to heat flow.

The morphological features of the elongated structures may represent the cellular formations that develop along the temperature gradient during rapid solidification, varying with cooling rate. It is possible to observe also some oval or elliptical shapes which may indicate porosity or material discontinuities, common defects in additive manufacturing that can affect mechanical properties.

Summarizing, these microstructures reflect typical directional solidification patterns and potential LPBF process defects. Further analysis, such as SEM, may be required for understanding better the structure.

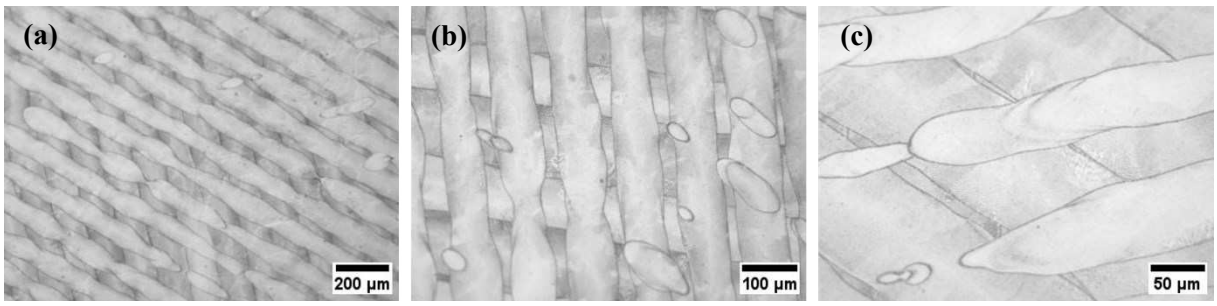

Figure 27: Optical microscope photo of Nopat40 at different magnitudes: (a) 5x, (b) 10x, (c) 20x.

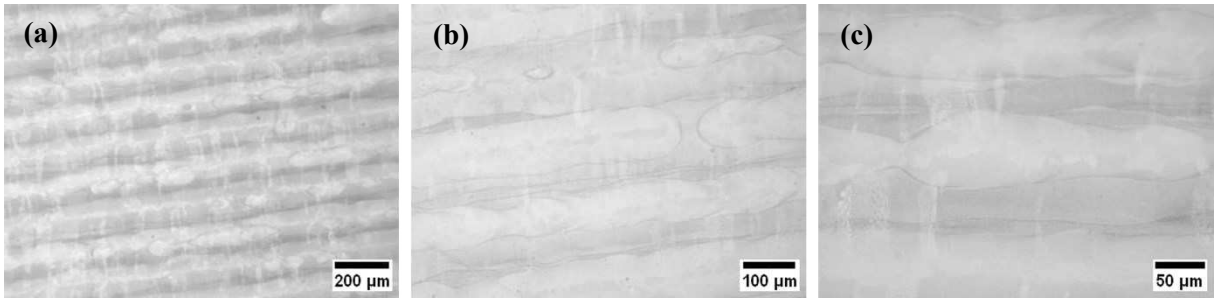

Figure 28: Optical microscope photo of Nopat180 at different magnitudes: (a) 5x, (b) 10x, (c) 20x.

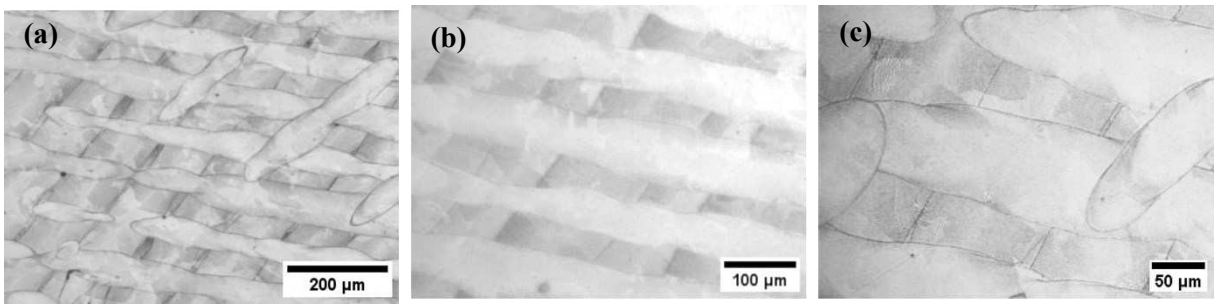

Figure 29: Optical microscope photo of Stripes at different magnitudes: (a) 5x, (b) 10x, (c) 20x.

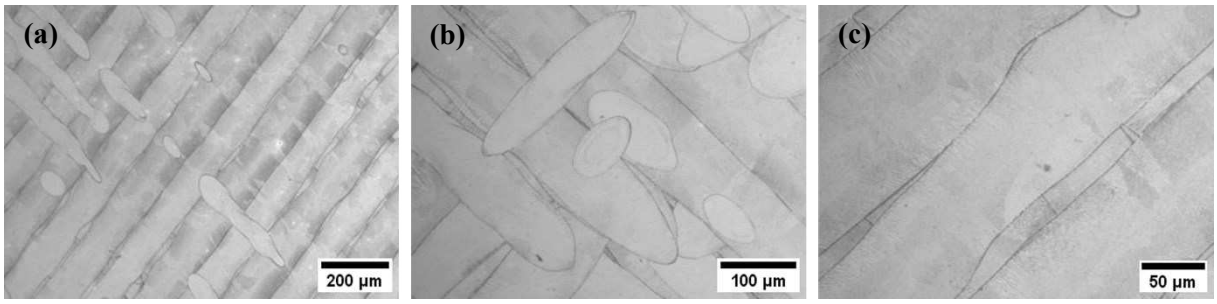

Figure 30: Optical microscope photo of Chess at different magnitudes: (a) 5x, (b) 10x, (c) 20x.

3.1.2 Scanning Electron Microscope (SEM)

From the analysis of images obtained through SEM microscopy following acid etching, clear distinctions are observed between samples produced conventionally and those manufactured using LPBF. The purpose of this analysis is also to compare the microstructure of LPBF samples treated at different temperatures and polished, with the goal of determining whether heat treatment has altered the microstructure and in what way. This was made possible using the SEM microscope, which offers magnifications of up to 10000x.

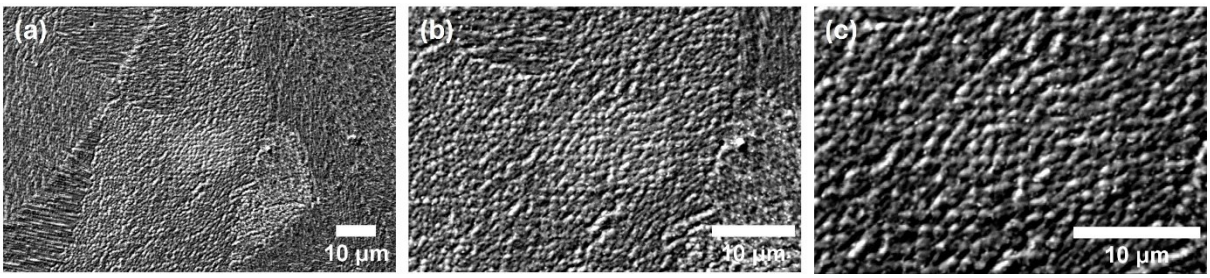

Figure 31: SEM image of Nopat40 HT200 at different magnitude (a)3K, (b) 6k, (c) 10k.

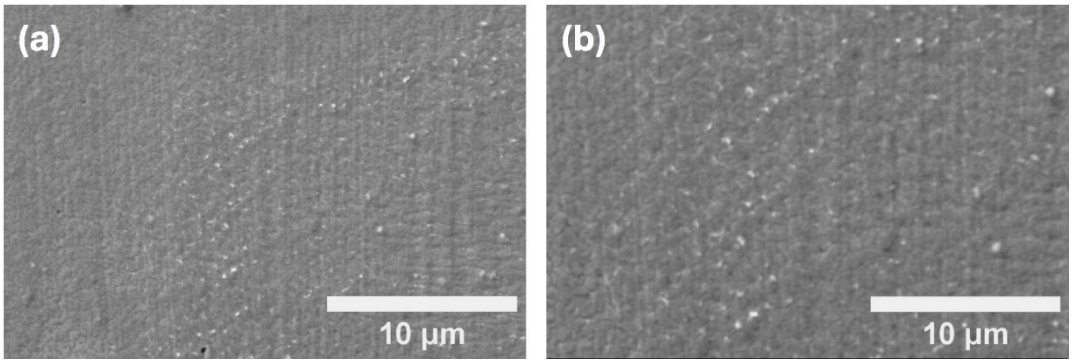

Figure 32: SEM image of Nopat40 HT300 at different magnitude (a) 6K, (b) 10k..

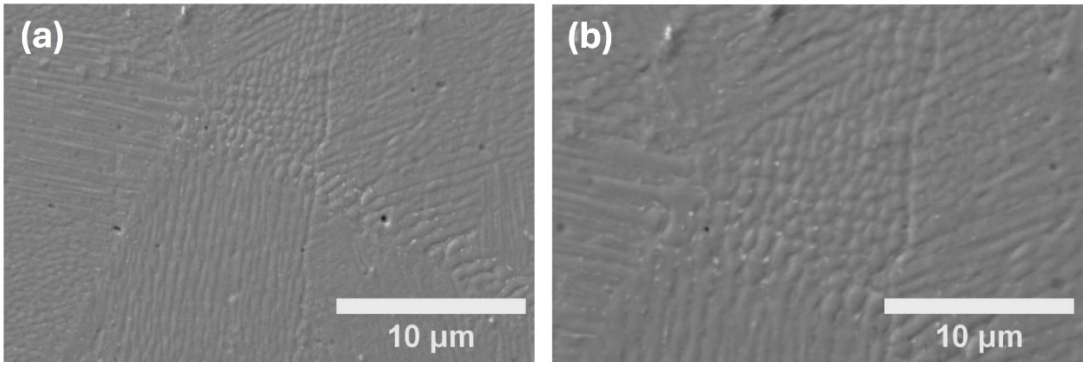

Figure 33: SEM image of Nopat40 HT400 at different magnitude (a) 6K, (b) 10k.

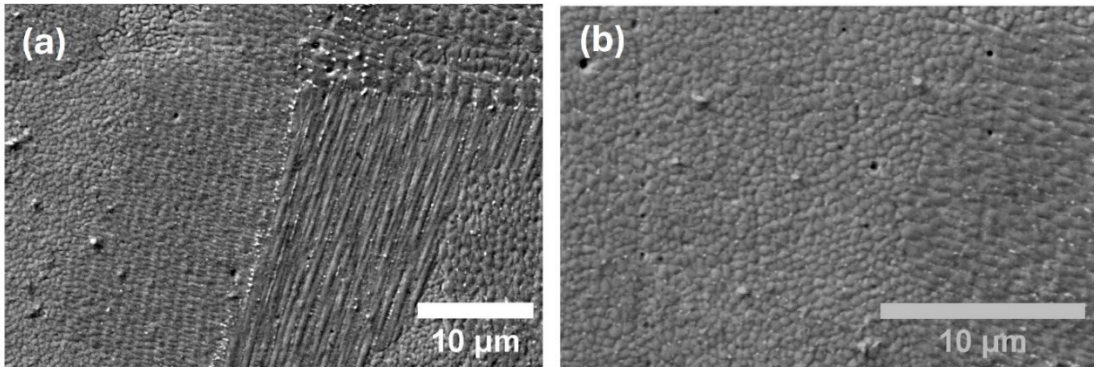

Figure 34: SEM image of Nopat40 HT500 at different magnitude (a) 6K, (b) 10k.

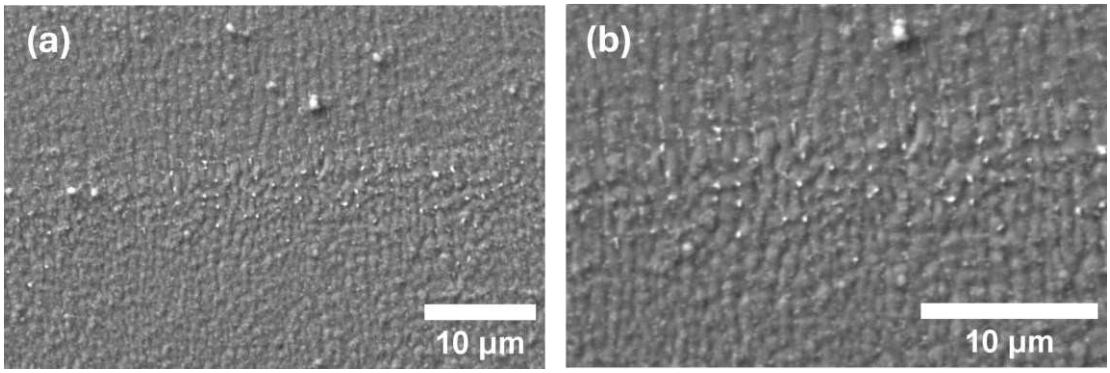

Figure 35: SEM image of Nopat180 HT200 at different magnitude (a) 6K, (b) 10k.

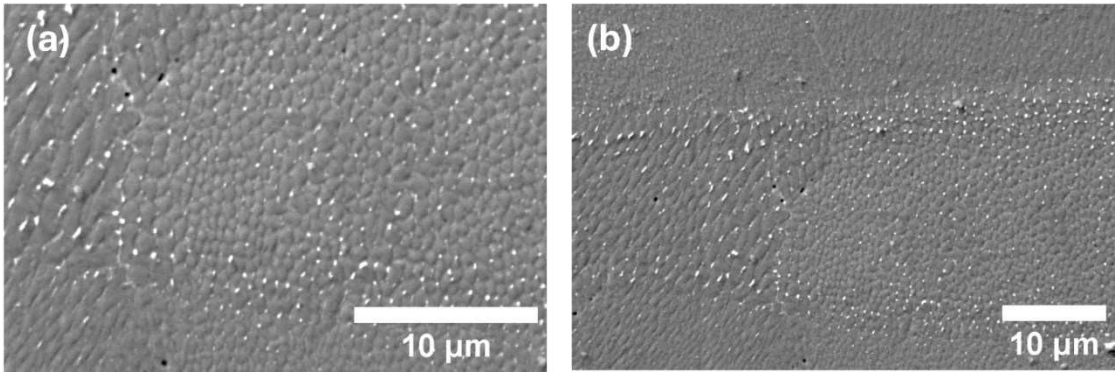

Figure 36: SEM image of Nopat180 HT300 at different magnitude (a) 6K, (b) 10k.

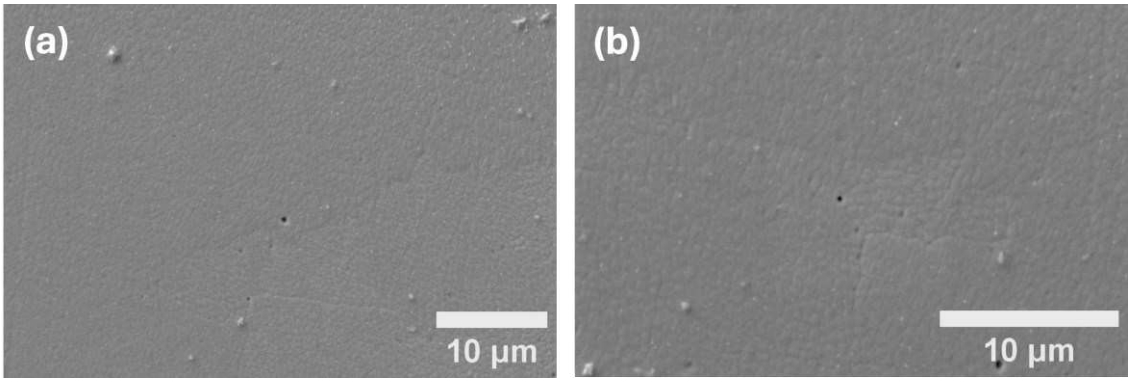

Figure 37: SEM image of Nopat180 HT400 at different magnitude (a) 6K, (b) 10k.

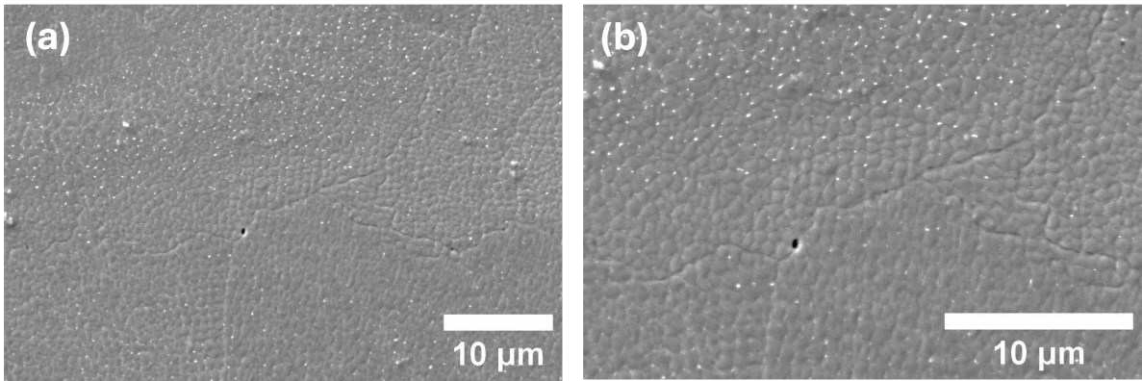

Figure 38: SEM image of Nopat180 HT500 at different magnitude (a) 6K, (b) 10k.

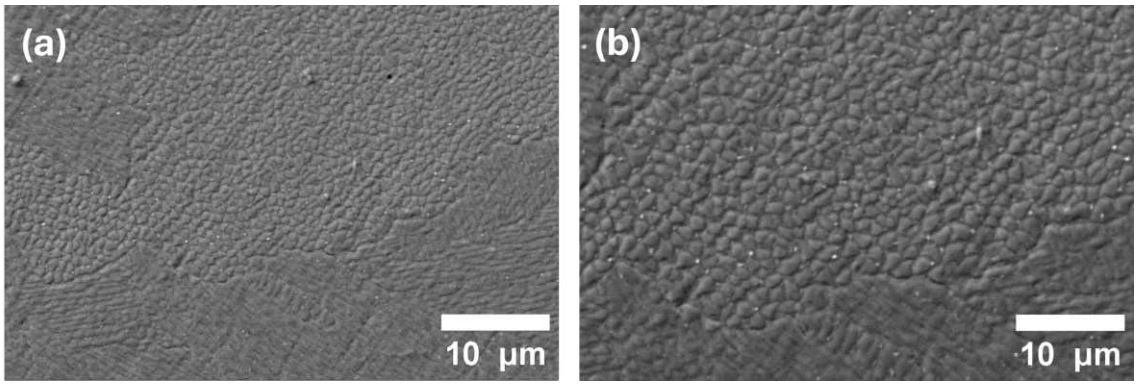

Figure 39: SEM image of Stripes HT200 at different magnitude (a) 6K, (b) 10k.

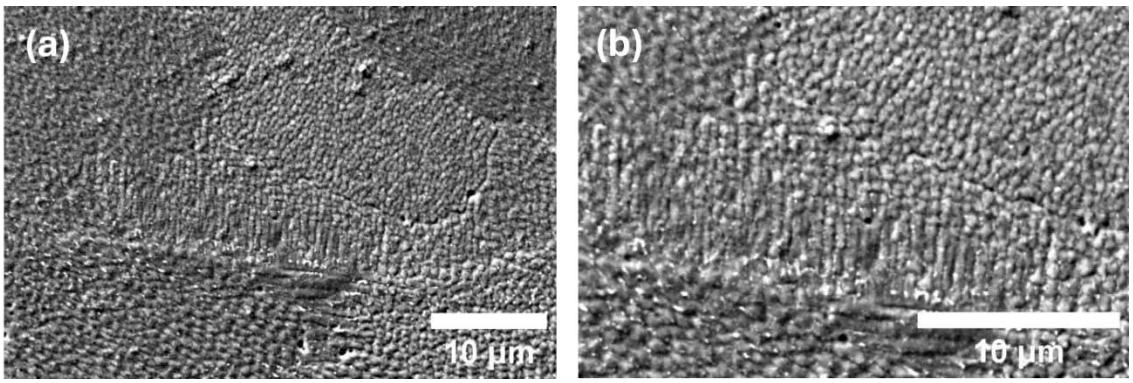

Figure 40: SEM image of Stripes HT300 at different magnitude (a) 6K, (b) 10k.

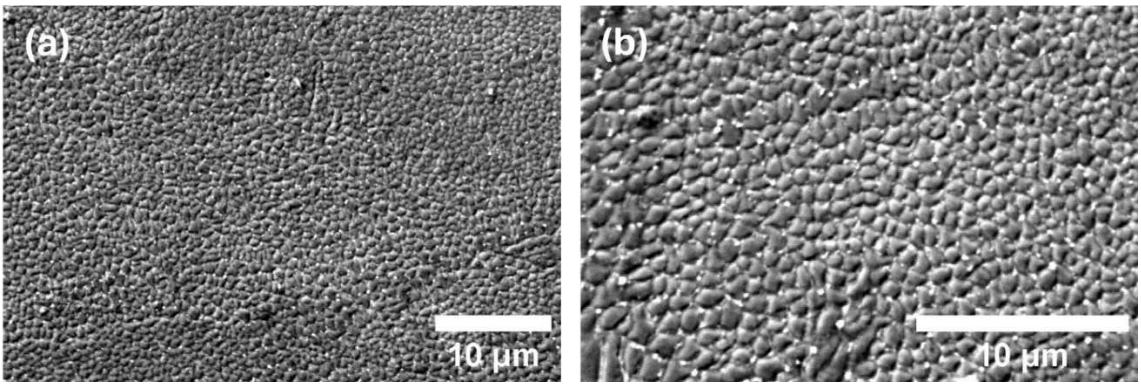

Figure 41: SEM image of Stripes HT400 at different magnitude (a) 6K, (b) 10k.

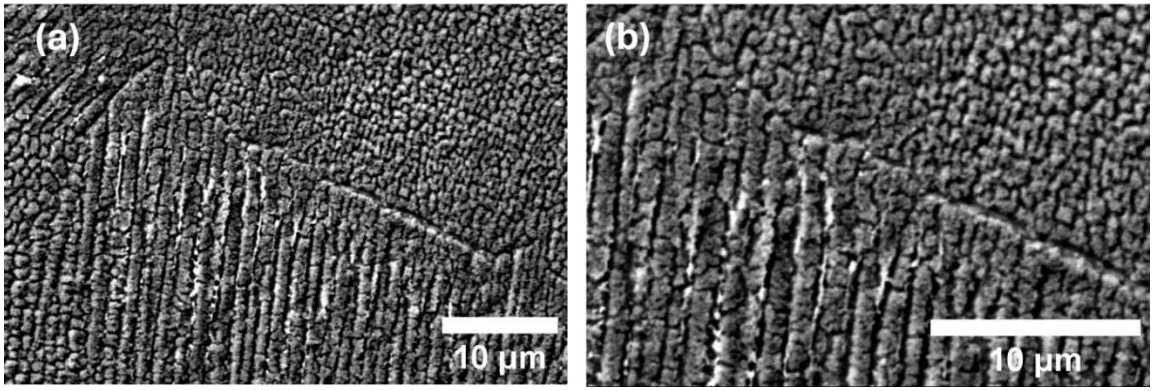

Figure 42: SEM image of Stripes HT500 at different magnitude (a) 6K, (b) 10k.

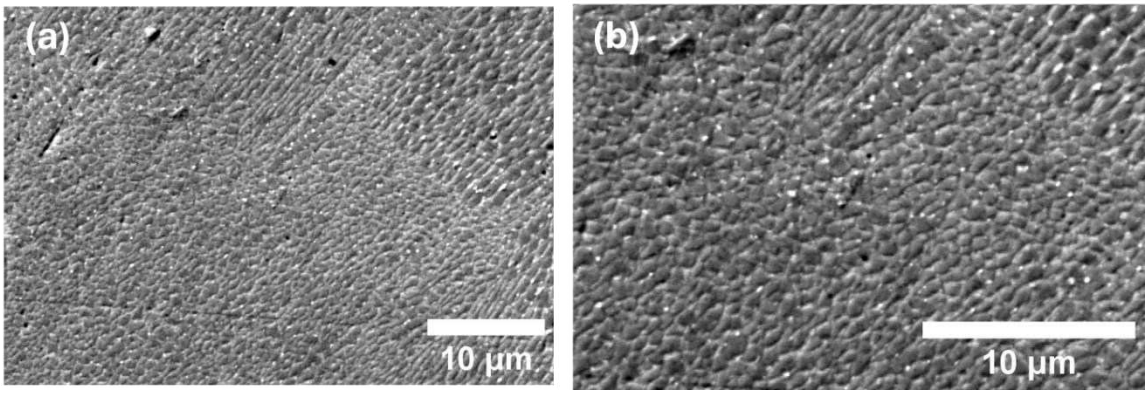

Figure 43: SEM image of Chess HT300 at different magnitude (a) 6K, (b) 10k.

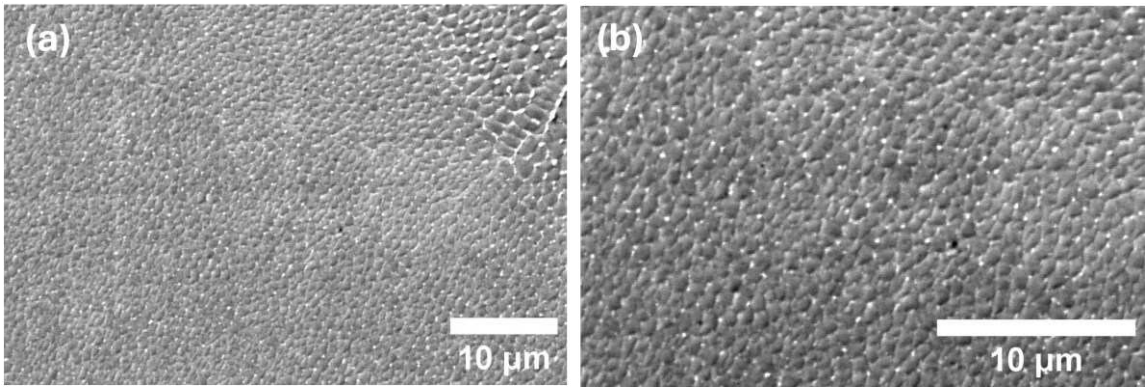

Figure 44: SEM image of Chess HT400 at different magnitude (a) 6K, (b) 10k.

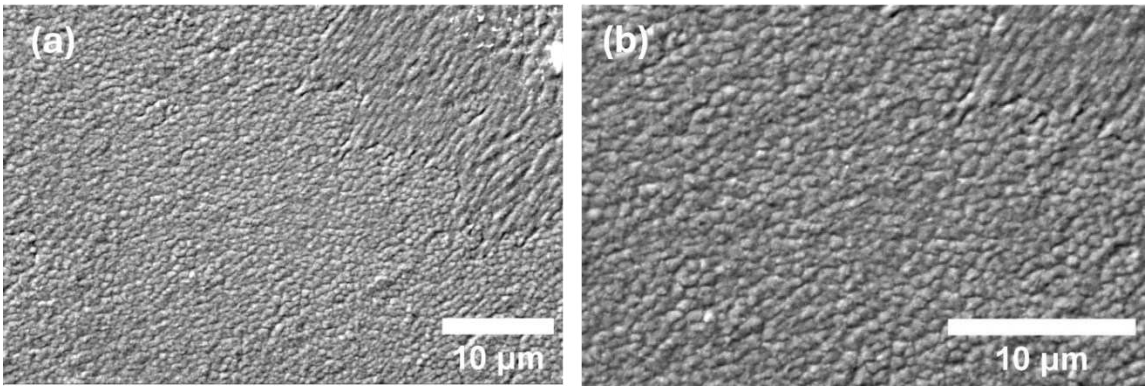

Figure 45: SEM image of Chess HT500 at different magnitude (a) 6K, (b) 10k.

During heat treatments, the grain size in Inconel 625 tends to increase with higher temperatures: this grain growth is thermodynamically driven, as grain boundaries decrease to minimize the system's overall energy. The growth of grains has a direct impact on its properties. This makes the control of grain size a critical factor in processing and heat treatment of Inconel 625, as it affects the balance between strength and durability in high-temperature applications.

3.2 Passive Layer Study

3.2.1 Potentiodynamic Polarization (PD)

The construction of the potentiodynamic polarization curves proceeds in a steady and consistent manner, spanning the potential range from -1.0V to 1.5V across all the samples tested. The measurements were carried out without any significant disruptions, ensuring reliable and reproducible data for each sample throughout the entire voltage sweep. This stable progression reflects the effectiveness of the experimental setup and the suitability of the test conditions for investigating the electrochemical behaviour of the materials under study. The potentiodynamic experiment was conducted twice on all samples, following the procedure described earlier: once in the thermal oxide condition and once after polishing the samples.

Thermal oxide condition

From the Figure 45 and 46 we can deduce that:

- At high temperatures, the passive layer of the samples analysed gradually loses its protective characteristics. This results in the disappearance of a distinct passive region, as the current continues to increase rather than stabilize. This behaviour suggests that the chromium oxide layer, which typically provides material protection, loses its effectiveness as a barrier against ion transfer, thereby exposing the material to a higher risk of degradation.
- Among the temperatures tested, 300 ºC proves to be optimal for passive layer stability. At this temperature, the oxide barrier exhibits the best protective properties, providing superior corrosion resistance compared to the other thermal conditions tested.
- In almost all of the samples examined, except for the Nopat180 sample, increasing the temperature leads to a thicker oxide layer, indicating potential improvement in surface protection. However, in the specific case of Nopat180, the increase in thickness is observed only beyond 300 ºC, revealing behavior that is distinct from the other materials.
- As the temperature rises, ion activity becomes increasingly pronounced, facilitating ionic penetration into the surface layer. This process causes a gradual deformation of the passive layer, reducing its protective capacity across all the samples analyzed. Ultimately, the increase in temperature accelerates the deterioration processes of the passive layer.

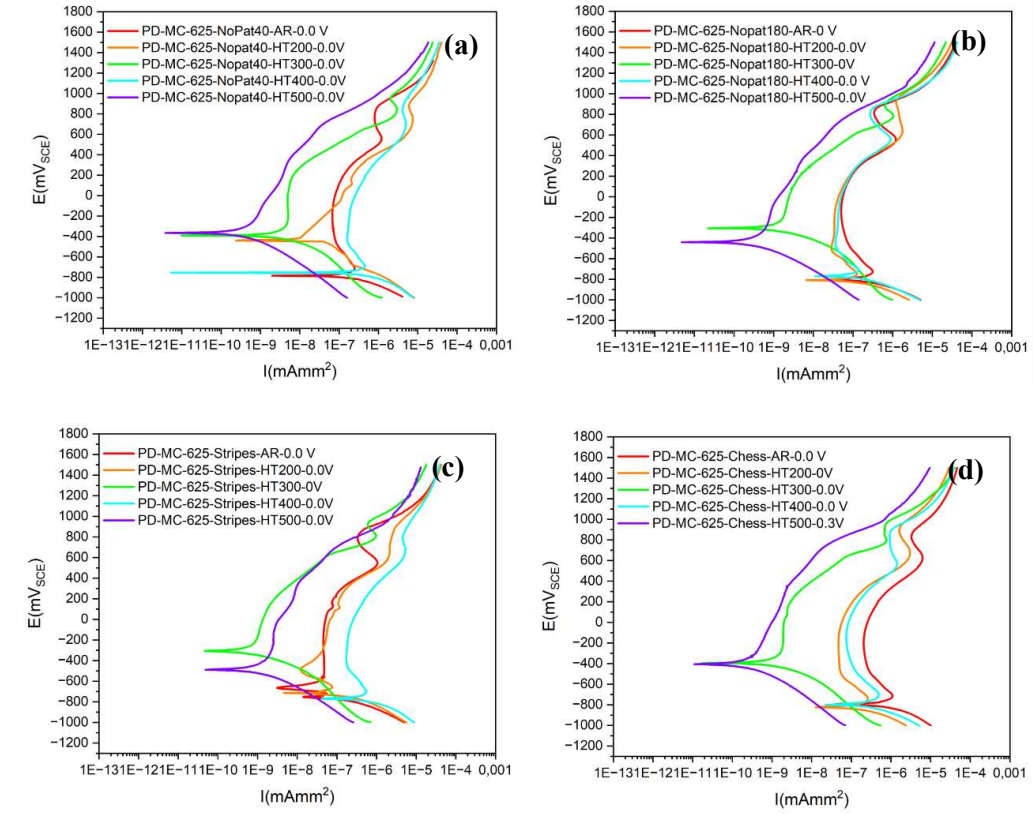

Figure 45: PD curves in thermal oxide condition (imposed E as a function of current) of LPBF samples with Borate Buffer solution at same state: conditioning 0.0 V (a) HT200, (b) HT300, (c) HT400, (d) HT500

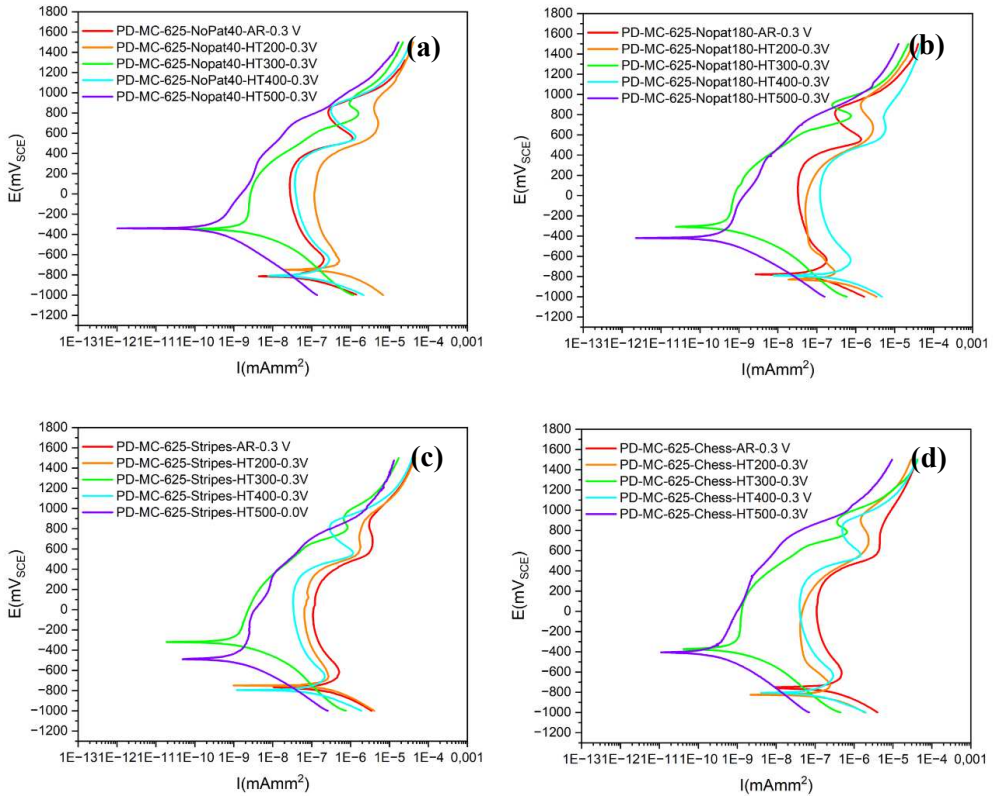

Figure 46: PD curves in thermal oxide condition (imposed E as a function of current) of LPBF samples with Borate Buffer solution at same state: conditioning 0.3 V (a) HT200, (b) HT300, (c) HT400, (d) HT500

Polished samples

It is clear that, in the as-recived (AR) condition, the Nopat40 and Nopat180 samples show the best performance, demonstrating greater stability than the others. In the same AR condition, however, Chess exhibits the poorest performance, likely due to the stronger laser interaction between the different layers, which generates high levels of residual stress. However, as the temperature increases, Chess shows a progressive improvement in performance due to the reduction and release of residual stresses. This effect significantly enhances its resistance, making it perform better than the Nopat samples.

Raising the heat treatment to 200 ºC, a gradual improvement in the performance of Chess and Stripes compared to the Nopat samples is observed, as the partial release of residual stresses begins to strengthen the stability of the oxide layer. At this temperature, residual stresses are still present but at relatively low levels, allowing for some protection without compromising the integrity of the surface layer.

At higher temperatures, the continuous release of residual stresses allows for further uniformity in material behaviour, progressively reducing differences between the samples. This effect becomes evident when the heat treatment exceeds 300 ºC, as the surface structure tends to stabilize and respond similarly across the various types of samples, until no significant differences are observed in the passive layer protection.

Between 300 and 500 ºC, Chess exhibits the best performance among all samples. In this temperature range, the release of residual stresses allows the oxide layer to maintain greater stability and better corrosion resistance compared to the Nopat and Stripes samples. However, above 500 ºC, the protective properties of the oxide layer tend to decrease due to microstructural changes that reduce the effectiveness of the protective barrier. At these elevated temperatures, the differences in performance between the various samples become less significant, with similar results in terms of corrosion resistance.

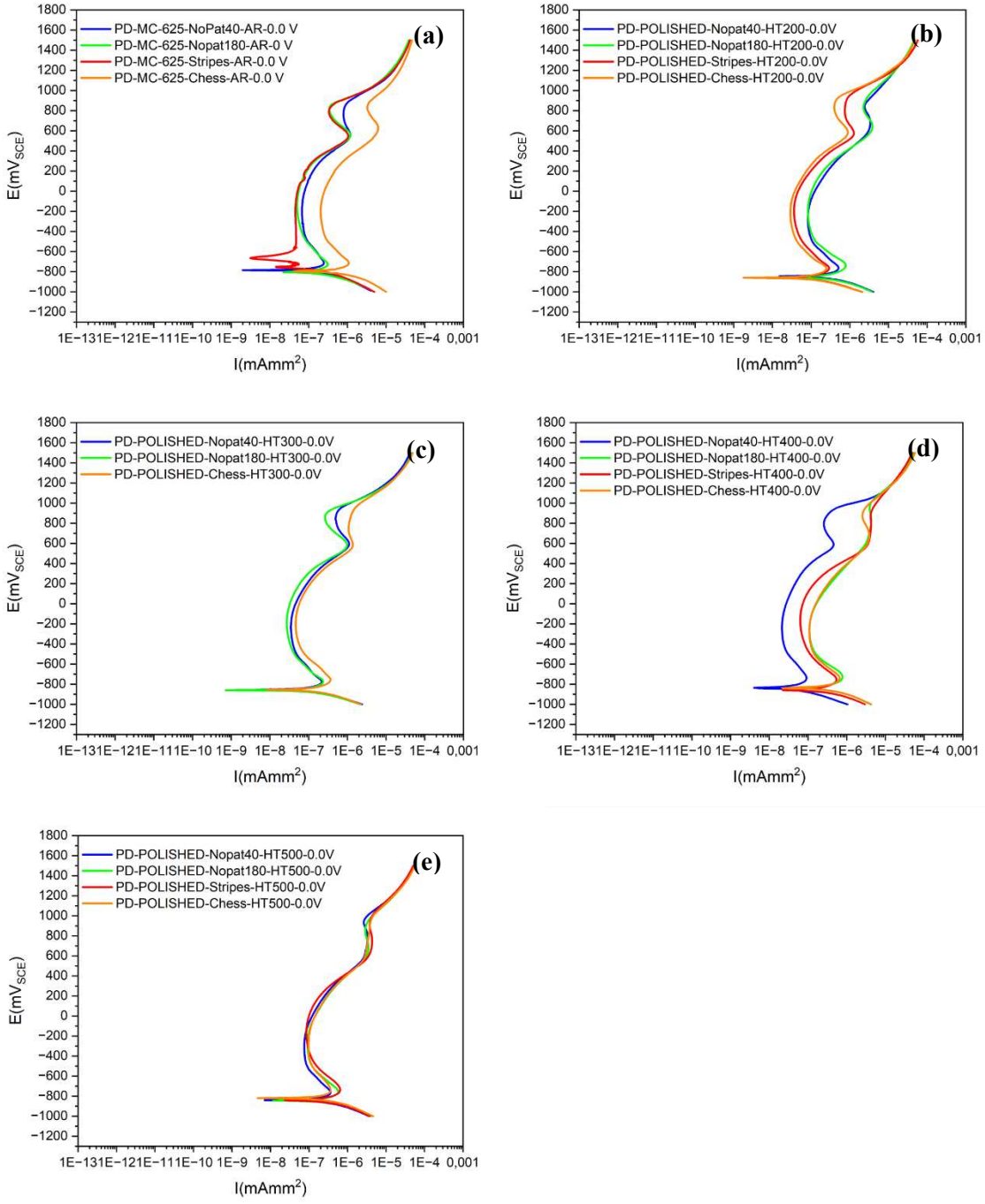

Figure 47: PD curves polished samples (imposed E as a function of current) of LPBF samples with Borate Buffer solution at same state: conditioning 0.0 V (a) AR, (b) HT200, (c) HT300, (d) HT400, (e) HT500

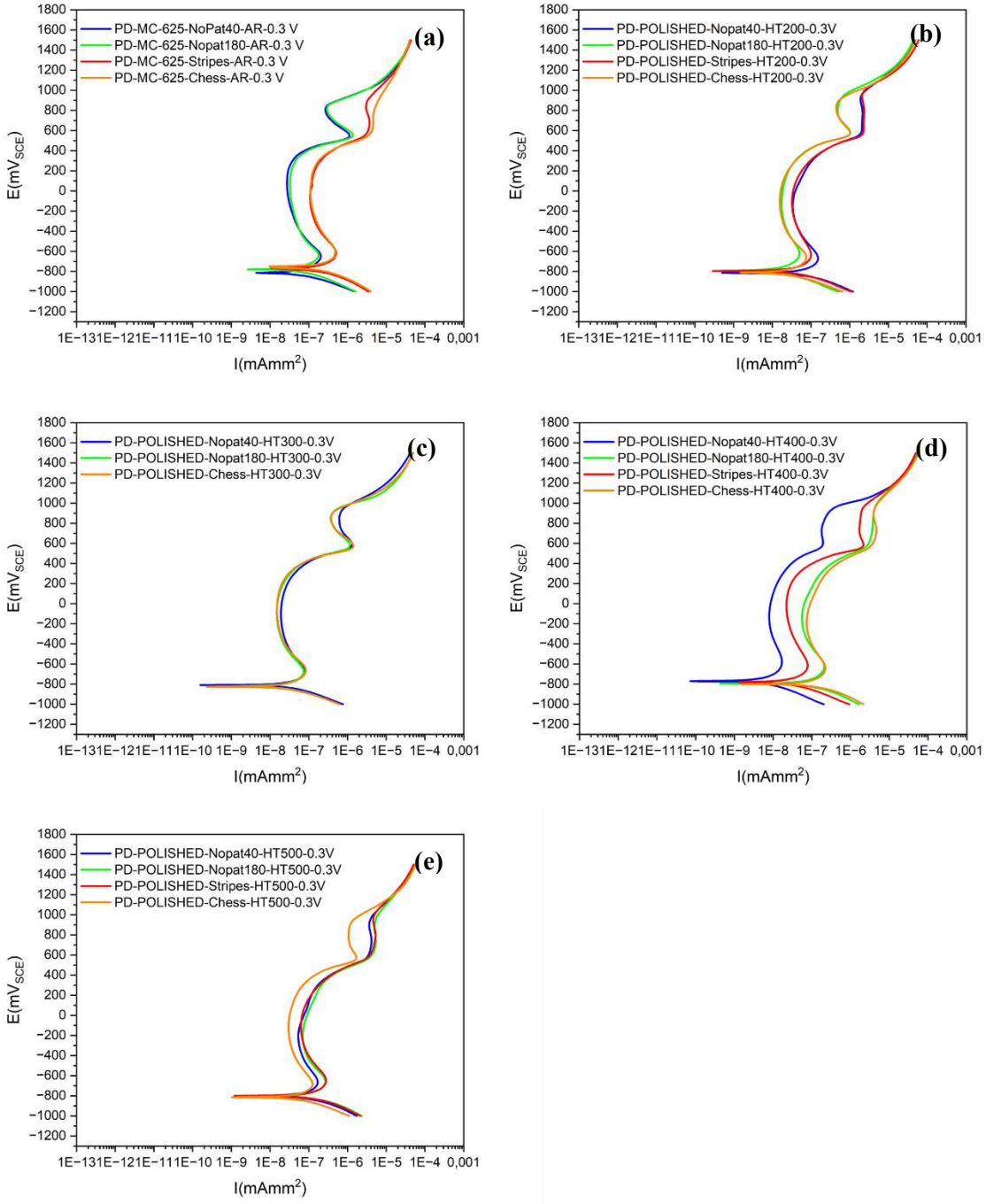

Figure 48: PD curves polished samples (imposed E as a function of current) of LPBF samples with Borate Buffer solution at same state: conditioning 0.3 V (a) AR, (b) HT200, (c) HT300, (d) HT400, (e) HT500

Comparison between thermal oxide condition and polished samples

In general, the thermal oxide condition exhibits better properties for the passive layer compared to the polished samples. However, this difference is less pronounced in the Stripes samples. At a temperature of 200°C, it is not sufficient to significantly alter the state of the passive layer between the thermal oxide condition and the polished samples. On the other hand, at 300°C, a difference can be observed for the Nopat and Chess samples. However, this difference is not noticeable in the Stripes samples, as the performance of the oxide layer is not significantly different between the two conditions. This suggests that for the Stripes samples, the passive layer formed immediately after thermal treatment is filled with defects.

At 300°C, the passive layer in the Stripes samples is less affected by ion transport compared to the other samples.

After reaching a temperature of 400°C, the oxide layer formed on the surface is so defective that instead of improving the performance of the barrier layer, it becomes worse. However, at 500°C, the thickness of the oxide layer increases. Although the layer is still defective, as evidenced by the absence of a clear passive region, the increased thickness still results in a lower ion flux through the layer.

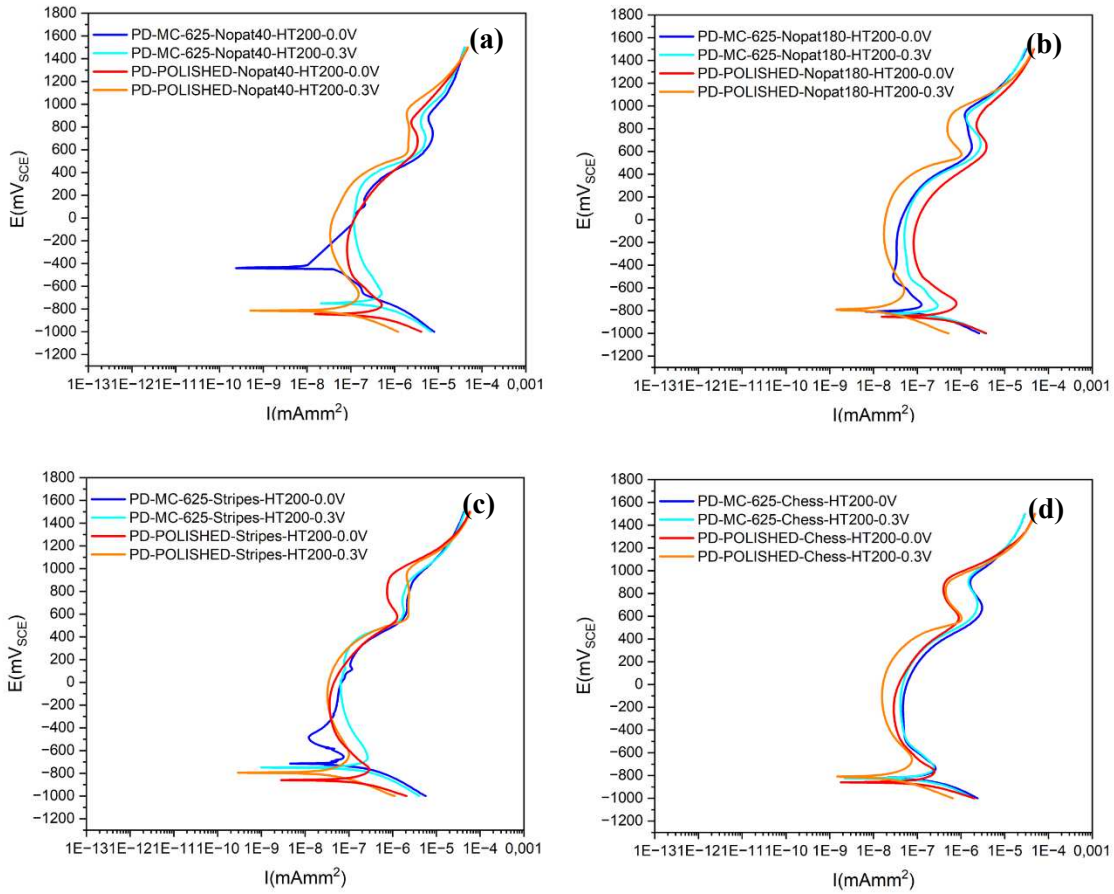

Figure 49: PD curves of HT200 LPBF samples (imposed E as a function of current) Borate Buffer solution with different conditioning and state (a) Nopat40, (b) Nopat180, (c) Stripes, (d) Chess.

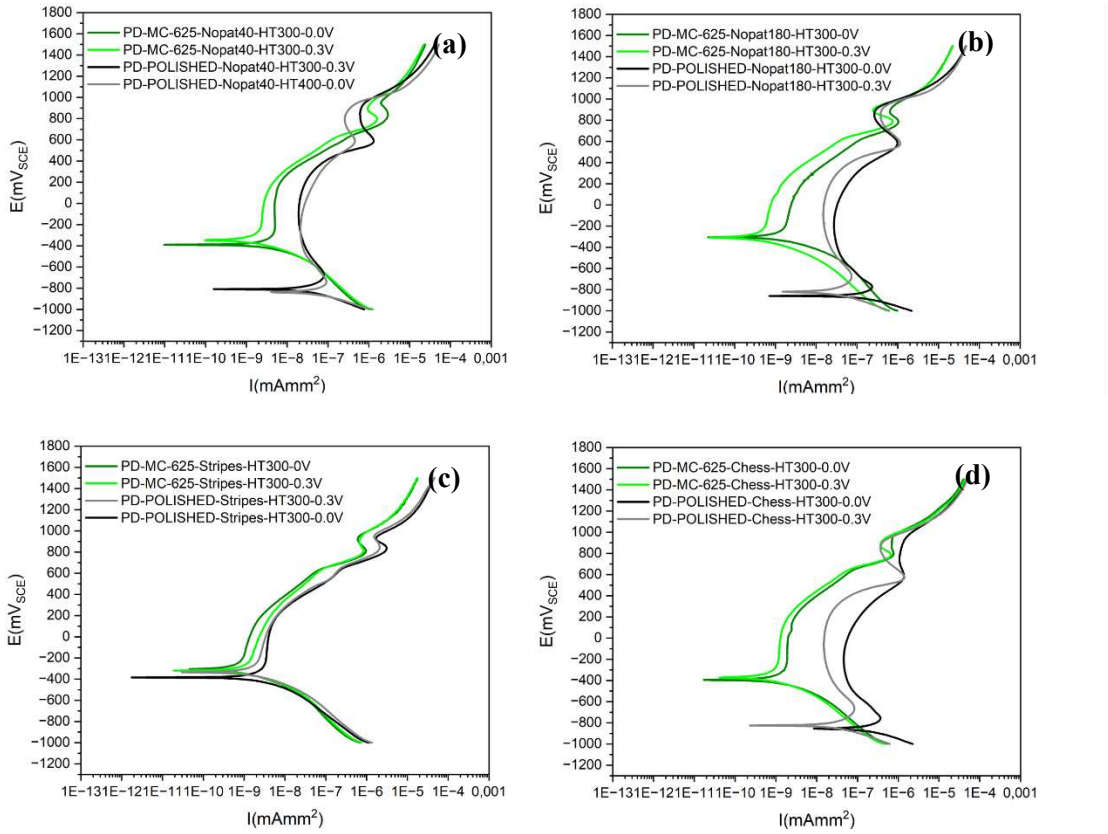

Figure 50: PD curves of HT300 LPBF samples (imposed E as a function of current) Borate Buffer solution with different conditioning and state (a) Nopat40, (b) Nopat180, (c) Stripes, (d) Chess.

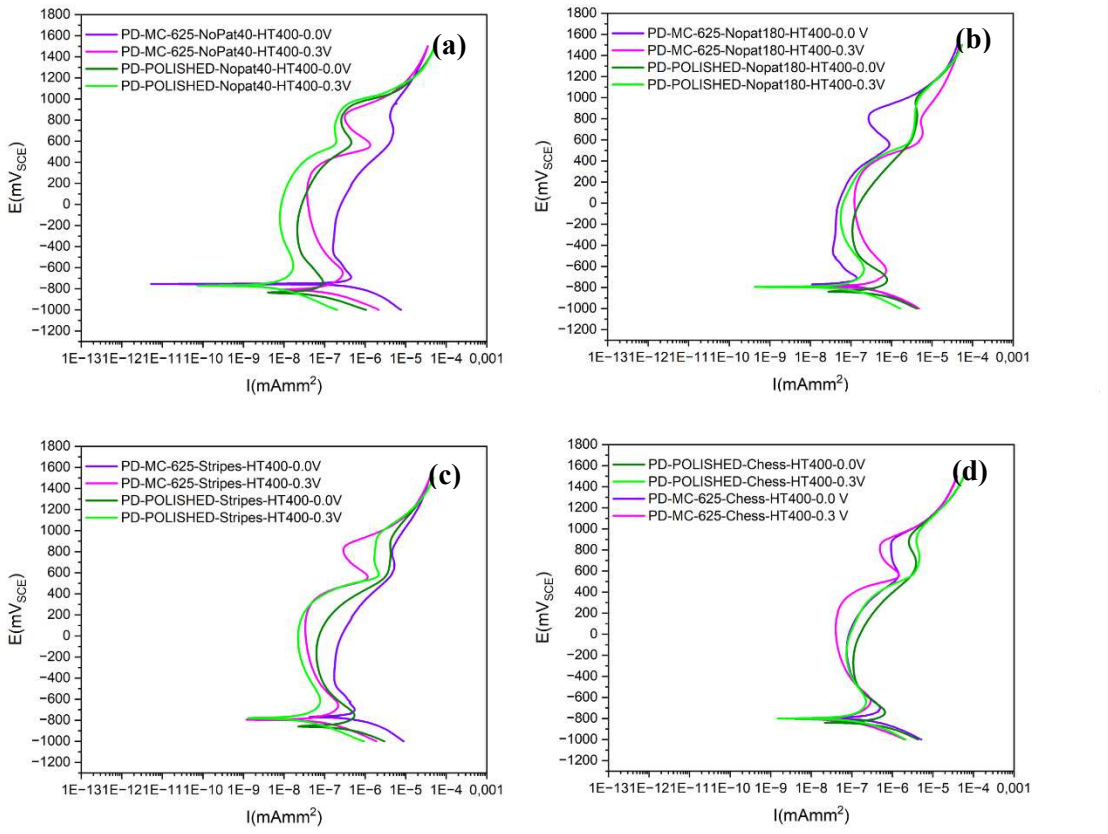

Figure 51: PD curves of HT400 LPBF samples (imposed E as a function of current) Borate Buffer solution with different conditioning and state (a) Nopat40, (b) Nopat180, (c) Stripes, (d) Chess.

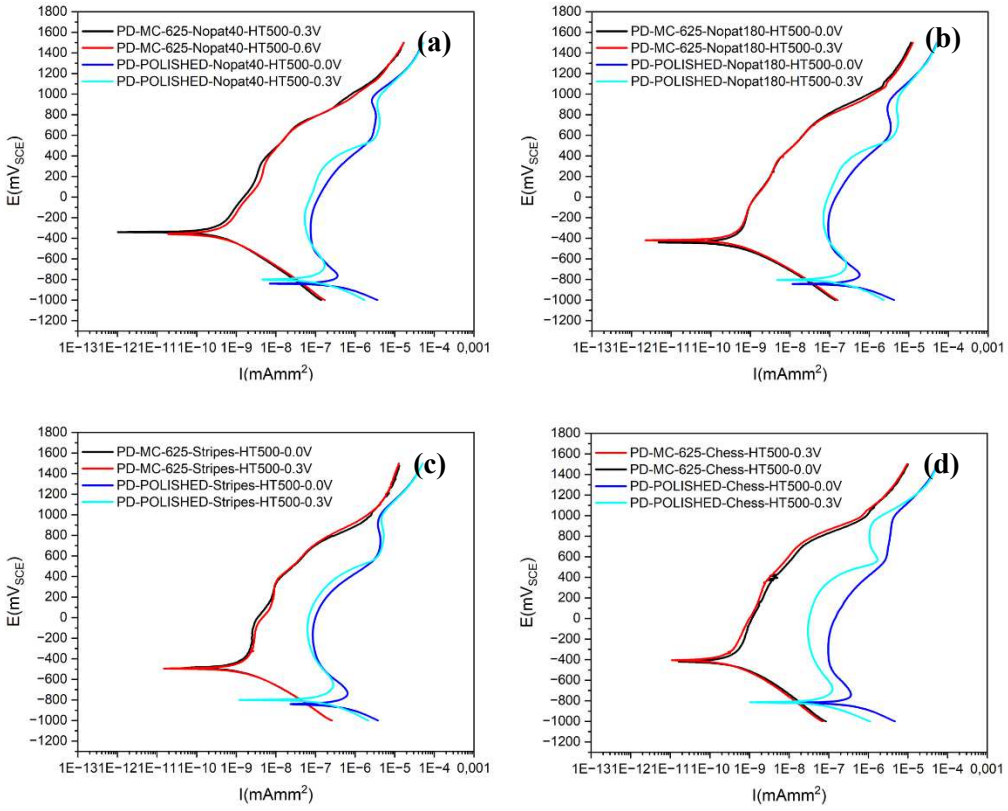

Figure 52: PD curves of HT500 LPBF samples (imposed E as a function of current) Borate Buffer solution with different conditioning and state (a) Nopat40, (b) Nopat180, (c) Stripes, (d) Chess

3.2.2 Mott-Schottky (MS)

The primary goal of Mott-Schottky analysis is to understand the semiconductive behaviour of the passive layer, specifically evaluating the quality of the oxide layer that forms and how defective or porous it might be. In this context, a higher capacitance is generally considered undesirable, as it suggests potential charge accumulation, which points to defects in the material hindering the flow of charge. As the oxide layer grows thicker, an increase in capacitance is observed, indicating a rising level of defects within the layer.

If we consider the AR samples without any conditioning and without heat treatment, the conventional sample demonstrates the best performance.

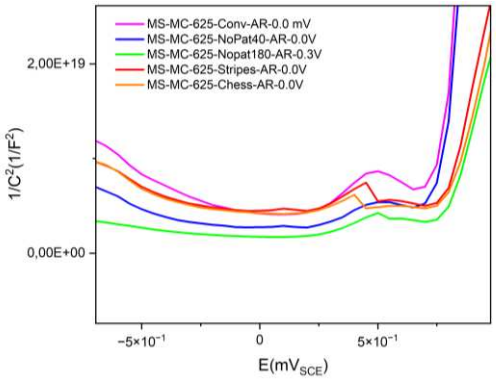

Figure 53: MS curves in thermal oxide condition of LPBF samples with Borate Buffer solution of LPBF samples at same state: conditioning 0.0 V

Thermal oxide condition

The electrochemical impedance spectroscopy (MS) graph clearly confirms the previous observations of PD (Figure 45 and 46).

In particular, the semiconductive properties of the oxide layer suggest a highly defective oxide structure when the temperature reaches or exceeds 400-500 ºC in all cases analysed. This indicates that, at these elevated temperatures, the oxide layer undergoes significant microstructural alterations, reducing its capacity to act as a protective barrier and making it more susceptible to ionic penetration and, consequently, degradation.

For most samples, except for Stripes, the maximum effectiveness of the protective oxide layer is reached around 200 ºC. In this temperature range, the oxidized layer appears more stable and less defective, maintaining better protective characteristics. However, the Stripes sample behaves differently, suggesting that its microstructure or composition may influence the oxide layer's response at moderate temperatures.

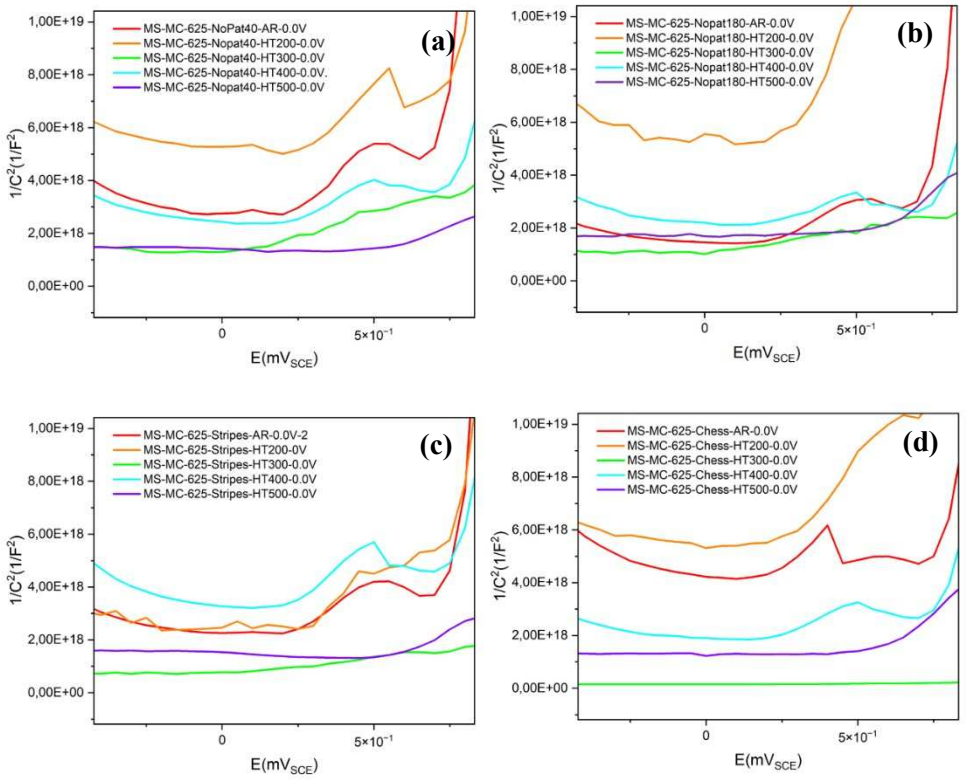

Figure 54:MS curves of HT200 LPBF samples Borate Buffer solution with same conditioning and state 0.0 V (a) Nopat40, (b) Nopat180, (c) Stripes, (d) Chess

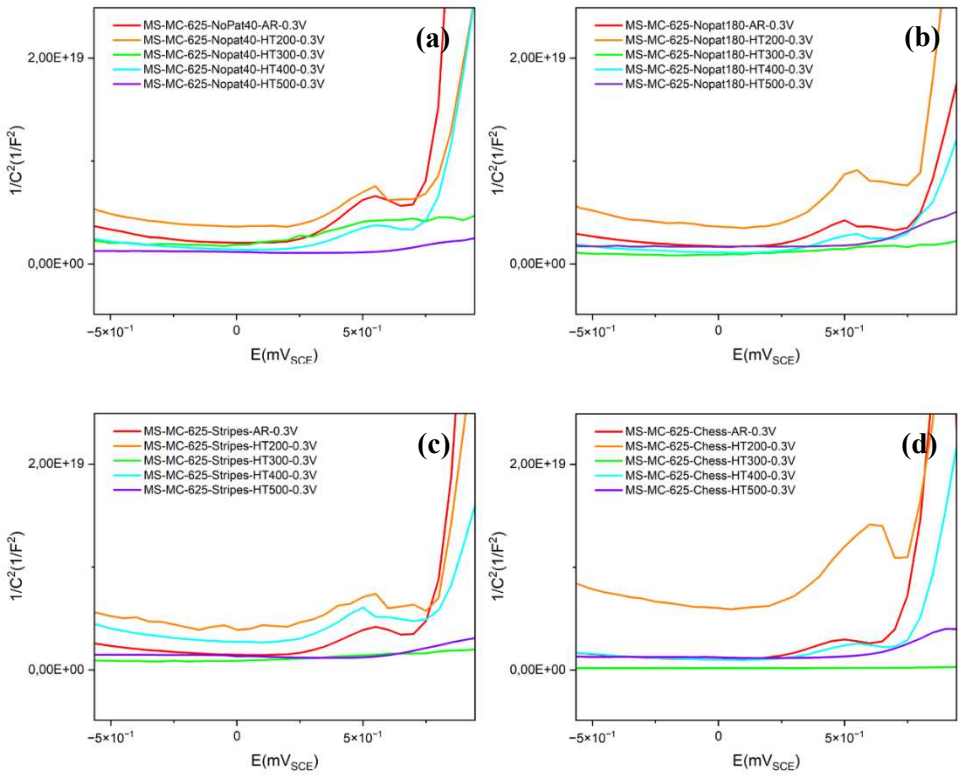

Figure 55:MS curves of HT200 LPBF samples Borate Buffer solution with same conditioning and state 0.3V (a) Nopat40, (b) Nopat180, (c) Stripes, (d) Chess

Polished samples

MS graphs confirm PD (Figure 47 and 48). It is clear that for all temperatures, except at 400°C. For all other temperature ranges, the passive layer reaches its maximum in the Nopat40 samples.

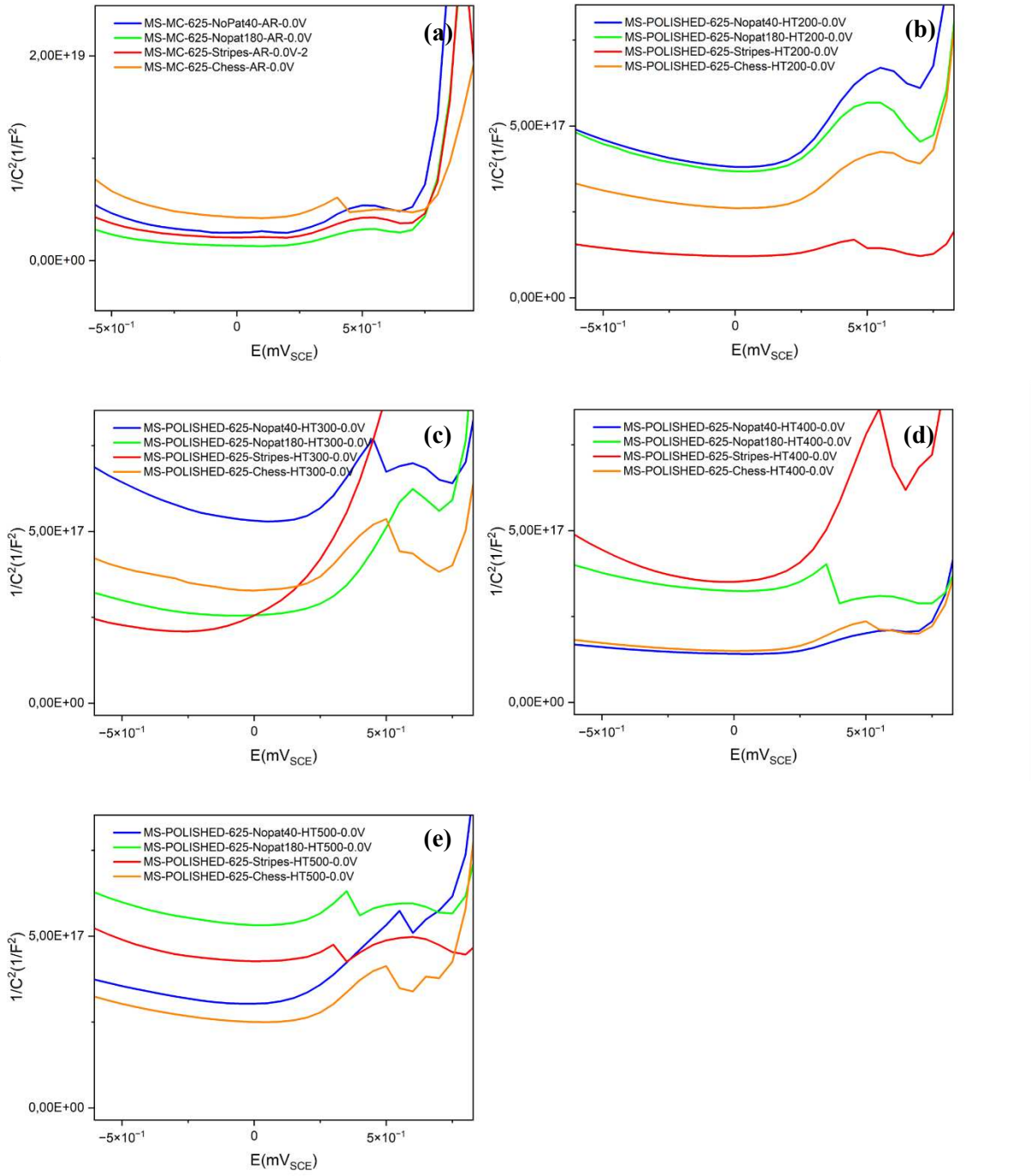

Figure 56:MS curves of LPBF samples Borate Buffer solution with same conditioning and state 0.0V (a) AR, (b) HT200, (c) HT300, (d) HT400, (e) HT500.

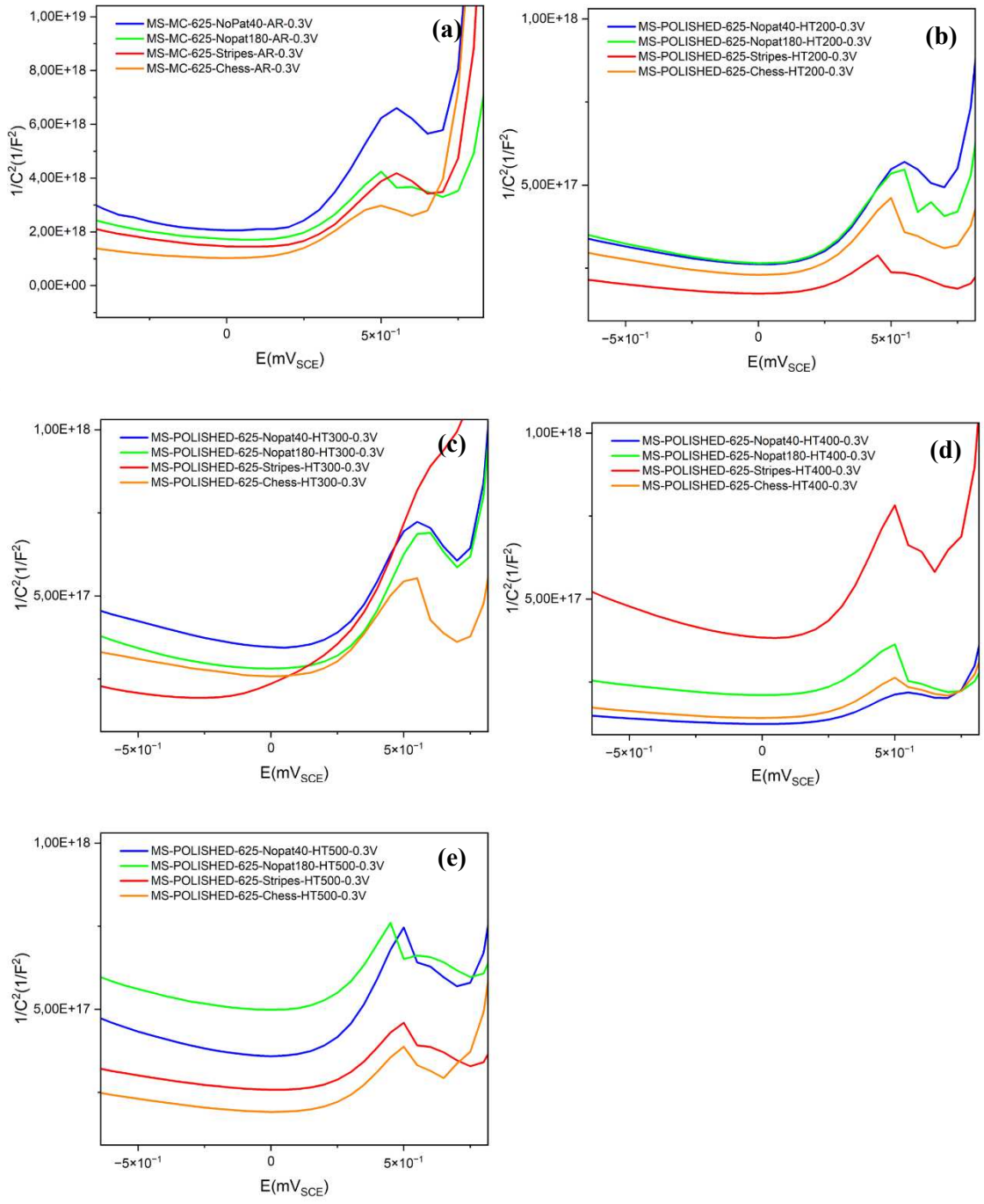

Figure 57:MS curves of LPBF samples Borate Buffer solution with same conditioning and state 0.3V (a) AR, (b) HT200, (c) HT300, (d) HT400, (e) HT500

3.3 Hardness test

For Inconel 625, a nickel-chromium-molybdenum alloy, hardness generally decreases with increasing temperature during heat treatment, particularly in the 200-500 °C range. At this temperature range, Inconel 625 tends to soften slightly, primarily because the temperature is not high enough to induce significant phase transformations or precipitation that would increase hardness. This response is because Inconel 625 retains its austenitic structure up to very high temperatures, and its mechanical properties remain stable up to around 600 °C. Above these temperatures, microstructural changes might start to occur, but at 200-500 °C, lower load resistance (and therefore lower Vickers hardness) is expected compared to lower temperatures, albeit with limited variations. [47]. Here an example in Figure 58 of a Vickers's test.

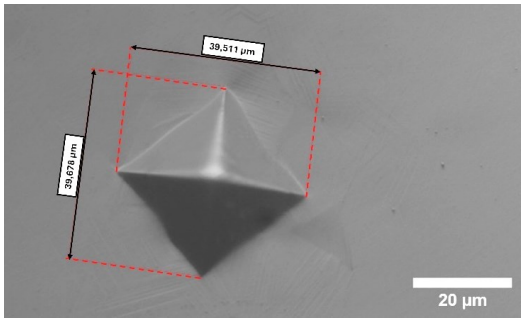

Figure 58: Example of hardness test on Conventional samples HT300.

Comparing the hardness results across various samples, we observe an overall trend of decreasing hardness, consistent with previously cited literature. Notably, at a temperature of 400 degrees, this trend reverses, highlighting once again the critical significance of this temperature.

	HT200	HT300	HT400	HT500
Nopat 40	299.32 HV	297.23 HV	306.70 HV	279.77 HV
Nopat180	301.73 HV	306.51 HV	344.92 HV	306.03 HV
Stripes	309.90 HV	297.33 HV	308.22 HV	183.66 HV
Chess	282.61 HV	299.5 HV	306.54 HV	208.22 HV

Table 5: Comparison of the hardness of all the samples.

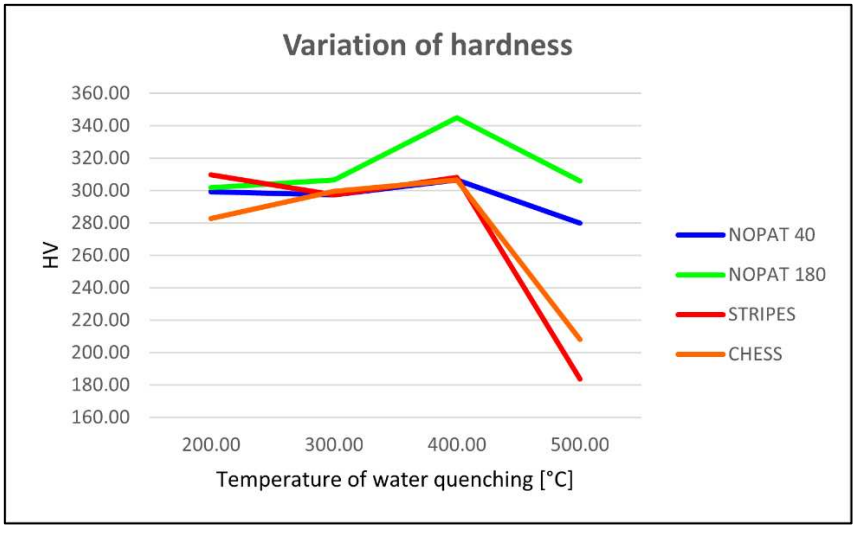

Figure 59: Variation of the hardness of all the samples.

4. Conclusion

Thermal treatments were performed to determine whether residual stresses could be reduced or eliminated to improve the properties of the passive layer while maintaining the cellular structure of the samples. According to the literature, it is recommended that AR (as-received) samples perform better in preserving the cellular structure, while Nopat samples generally optimize heat distribution and reduce residual stresses. In contrast, the Stripes and Chess patterns offer solutions to ensure uniform fusion and better structural integrity. However, this study revealed that the deposition pattern technique significantly influences the properties of the passive layer.

In the next phase, the aim was to identify the optimal temperature for each of the four sample types in order to reduce residual stresses and achieve comparable results across the different samples. In summary, it was observed that, to optimize the passive layer, the most favourable thermal treatment for the samples is as follows:

	Optimal temperature
Nopat 40	200°C
Nopat180	300°C
Stripes	300°C
Chess	200°C

4.1 Future developments

The findings of this study on Inconel 625 produced via Laser Powder Bed Fusion (LPBF) with four different deposition patterns (Nopat40, Nopat180, Stripes, and Chess), followed by thermal treatments up to 500°C, provide a strong foundation for future research aimed at further improving the performance of this material in aerospace and other high-performance applications.

A key area for future development lies in optimizing the thermal treatment processes, not only to reduce residual stresses but also to further enhance the properties of the passive layer. Future studies could explore a broader range of temperatures and heat treatment durations, as well as the potential use of multi-step heat treatments, to better understand how the interplay between temperature, microstructure, and the passive layer influences corrosion resistance and mechanical performance.

Additionally, while this study has explored the effect of deposition patterns on the properties of the passive layer, future work could investigate other deposition strategies, such as varying laser power, scan speed, and layer thickness, to further optimize the material's overall performance. The incorporation of advanced in-situ monitoring techniques, such as high-resolution thermal imaging and X-ray tomography, could offer deeper insights into the material behavior during the LPBF process and the subsequent heat treatments.

Moreover, extending the study to examine the long-term durability of Inconel 625 under cyclic loading conditions and exposure to extreme environmental factors, such as elevated pressures and corrosive atmospheres, would provide valuable data on its suitability for critical

aerospace components. The effect of environmental conditions on the oxide layer, as well as potential improvements in the material's fatigue resistance and crack propagation resistance, would be critical for evaluating its performance over time.

Finally, the application of machine learning algorithms to predict the optimal processing parameters based on the desired material properties could significantly streamline the design and production process for Inconel 625 in additive manufacturing. This approach would enable a more efficient and precise tailoring of the material properties for specific aerospace and industrial applications.

In conclusion, this study paves the way for further advancements in the use of Inconel 625 produced by additive manufacturing, and future research will continue to focus on refining processing techniques, improving material properties, and expanding the range of potential applications in demanding industries.

5. Reference

[1] B. Geddes, H. Leon, and X. Huang, Superalloys: Alloying and Performance. ASM International, 2010

[2] C.T. Sims, Superalloys: Genesis and Character, Superalloys II, C.T. Sims, N.S. Stoloff, and W.C. Hagel, Ed., John Wiley & Sons, 1987

[3] Unit Cell https://byjus.com/chemistry/bcc-fcc-primitive-cubic-unit-cell/

[4] Electrochemical Methods: Fundamentals and Applications di Allen J. Bard e Larry R. Faulkner

[5] Jung Bahadur Singh Alloy 625 Microstructure, Properties and Performance

[6] Mars G. Fontana, Corrosion Engineering. McGraw-Hill Book Company

[7] ASM Handbook, Volume 2: Properties and Selection: Nonferrous Alloys and Special-Purpose Materials" by ASM International

[8] Introduction to Solid State Physics by Charles Kitt

[9] Solid State Physics: An Introduction by Philip Hofmann

[10] The γ' Phase in Nickel-Based Superalloys: A Review in Journal of Materials Science

[11] Precipitation Hardening of Nickel-Based Superalloys: Mechanisms and Modeling published in Metallurgical and Materials Transactions

[12] The γ'' Phase in Nickel-Based Superalloys: Formation, Structure, and Properties published in Metallurgical and Materials Transactions A

[13] Carbide Precipitation in Nickel-Based Superalloys: Microstructural Analysis and Effects on Mechanical Properties" published in Materials Science and Engineering A.

[14] Potential for carbide dispersive precipitation strengthening Ni-based alloy for high temperature He Jiang, Fa Wang, Jianxin Dong

[15] Oxidation of Nickel-Chromium Alloys in Journal of Materials Science

[16] Powder bed fusion additive manufacturing of Ni-based superalloys: a review of the main microstructural constituents and characterization techniques Michael P. Haines, Vitor V. Rielli, Sophie Primig and Nima Haghdadi

[17] Haines, M. P., Rielli, V. V., Primig, S., & Haghdadi, N. (2022). Powder bed fusion additive manufacturing of Ni-based superalloys: A review of the main microstructural constituents and characterization techniques. Journal of Materials Science

[18] Laser Additive Manufacturing: Materials, Design, Technologies, and Applications" di G. Leal, A. S. Guedes, e A. A. M. G. Reis

[19] Effects of Power and Laser Speed on the Mechanical Properties of AlSi7Mg0.6 Manufactured by Laser Powder Bed Fusion, Sébastien Vaudreuil, Salah-Eddine Bencaid, Hamid Reza Vanaei and Anouar El Magri

[20] P. Pedeferri e L. Lazzari, Corrosion Science and Engineering Springer

[21] H. Herrera Hernández et al., 'Electrochemical Impedance Spectroscopy (EIS): A Review Study of Basic Aspects of the Corrosion Mechanism Applied to Steels', in Electrochemical Impedance Spectroscopy, M. El-Azazy, M. Min, and P. Annus, Eds., IntechOpen, 2020

[22] Reflections on the history of electrochemical impedance spectroscopy, Digby D. Macdonald

[23] Development and Investigation of Innovative Materials Produced by Means of Additive Manufacturing Technologies Francesco Carugo

[24] Corrosion Performance of Ni-Based Alloys in Sodium Metavanadate O. Sotelo Mazon,Jesus Porcayo-Calderon,C. Cuevas-Arteaga,Lorenzo Martinez Gomez

[25] K. D. Ramkumar, W. S. Abraham, V. Viyash, N. Arivazhagan, and A. M. Rabel, 'Investigations on the microstructure, tensile strength and high temperature corrosion behaviour of Inconel 625 and Inconel 718 dissimilar joints', Journal of Manufacturing Processes
[26] N. Eliaz, «Corrosion of Metallic Biomaterials: A Review», Materials, vol. 12, fasc. 3
[27] X-ray photoelectron spectroscopy study of the passive films formed on thermally sprayed and wrought Inconel 625, M.S. Bakare, K.T. Voisey, M.J. Roe, D.G. McCartney
[28] A. J. Bard and L. R. Faulkner, "Electrochemical Methods: Fundamentals and Applications," 2nd Edition, Wiley, 2001
[29] A comprehensive literature review on laser power bed fusion Inconel superalloys, Guilherme Maziero Volpato, Ultrich Ttexlaff and Marcio Celso Fredel
[30] Characterization of Inconel 625 fabricated using powder-bed-based additive manufacturing technologies J.A. Gonzaleza, J. Mirelesa, S.W. Staffordb, M.A. Pereza, C.A. Terrazasa, R.B. Wickera
[31] Mechanical Behavior of Laser Powder Bed Fusion Processed Inconel 625 Alloy Hua Sun, K. S. N. Satish Idury,V. Chakkravarthy,R. L. Narayan
[32] Evaluation of Corrosion Resistance of Alloy 625 Obtained by Laser Powder Bed Fusion M. Cabrini, S. Lorenzi, C. Testa, T. Pastore, F. Brevi, S. Biamino, P. Fino, D. Manfredi, G. Marchese, F. Calignano and F. Scenini
[33] Effect of heat treatment on the anisotropic mechanical properties and corrosion resistance of laser powder bed fusion fabricated Inconel 625 Jie Zhu, Kai Feng, Hiroyuki Kokawa, Zhuguo Li
[34] Effect of heat treatment on microstructure and oxidation properties of Inconel 625 processed by LPBF Simone Parizia, Giulio Marchese, Masoud Rashidi Massimo Lorusso,Eduard Hryha, Diego Manfredi, Sara Biamino
[35] Effects of temperature on the protective property, structure and composition of the oxide film on Alloy 625 Hua Sun, Xinqiang Wu, En-Hou Han
[36] Role of Elemental Segregation on the Oxidation Behavior of Additively Manufactured Alloy 625 G. del Leon Nope, G. Wang, M. Alvardo-Orozco and B. Gleeson
[37] Studies on the Oxidation Behavior of Inconel 625 Between 873 and 1523 K, Lalit Kumar, R. Venkataramani, M. Sundararaman, P. Mukhopadhyay and S. P. Garg
[38] Ultrasonic cleaning and washing of surfaces F.J. Fuchs, in Power Ultrasonics, 2015
[39] Extending powder lifetime in additive manufacturing: Chemical etching of stainless-steel spatter W. Murray, Alistair Speidel, Adriaan Spierings, Ian J. Marsh, Adam T. Clare
[40] A Comparative Analysis Between Material Extrusion and Other Additive Manufacturing Techniques: Defects, Microstructure and Corrosion Behavior in Nickel Alloy 625 A. Carrozza, S. Lorenzi, F. Carugo, S. Fest-Santini, M. Santini, G. Marchese,G. Barbieri,F. Cognini, M. Cabrini, T. Pastore
[41] Inconel Alloy 625 in Aerospace Engineering https://bswmetals.ro/en/inconel-alloy-625-in-aerospace-engineering
[42] Inconel Alloy 625 in Aerospace Engineering https://www.jaimannickelalloys.com/blog/inconel-alloy-625-in-aerospace-engineering
[43] Nickel 625 a Superalloy for Extreme Environments https://continentalsteel.com/blog/nickel-625-for-extreme-environments
[44] A Review on Laser Powder Bed Fusion of Inconel 625 Nickel-Based Alloy Zhihua Tian, Chaoqun Zhang , Dayong Wang , Wen Liu, Xiaoying Fang, DanielWellmann, Yongtao Zhao and Yingtao Tian

[45] Mott, N. F., & Schottky, W. (1938). The electronic conduction of semiconductors. Proceedings of the Royal Society A: Mathematical, Physical and Engineering Sciences
[46] The Vickers Hardness Testing Machine. UKcalibrations.co.uk. Retrieved on 2016/06/03
[47] ASM Specialty Handbook: Nickel, Cobalt, and Their Alloys
[48] Exploring the mechanism of stress-induced passive layer degradation in additively manufactured Ni-Fe-Cr-based alloy 718 Arshad Yazdanpanah , Reynier I. Revilla, Mattia Franceschi, Gioele Pagot, Mona Khodabakhshi, Iris De Graeve, Vito Di Noto, Manuele Dabala, Sergio Lozano-Perez